SOLUTION OF ELECTROMAGNETIC SCATTERING PROBLEMS WITH THE LOCALLY CORRECTED NYSTRÖM METHOD

A THESIS

SUBMITTED TO THE DEPARTMENT OF ELECTRICAL AND

ELECTRONICS ENGINEERING

AND THE INSTITUTE OF ENGINEERING AND SCIENCE

OF BILKENT UNIVERSITY

IN PARTIAL FULFILLMENT OF THE REQUIREMENTS

FOR THE DEGREE OF

MASTER OF SCIENCE

By

Seçil Kılınç

September 2010

I certify that I have read this thesis and that in my opinion it is fully adequate, in scope and in quality, as a thesis for the degree of Master of Science.

Prof. Dr. Levent Gürel (Supervisor)

I certify that I have read this thesis and that in my opinion it is fully adequate, in scope and in quality, as a thesis for the degree of Master of Science.

Prof. Dr. Ayhan Altıntaş

I certify that I have read this thesis and that in my opinion it is fully adequate, in scope and in quality, as a thesis for the degree of Master of Science.

Assoc. Prof. Özlem Aydın Çivi

Approved for the Institute of Engineering and Sciences:

Prof. Dr. Levent Onural
Director of Institute of Engineering and Science

ABSTRACT

SOLUTION OF ELECTROMAGNETIC SCATTERING PROBLEMS WITH THE LOCALLY CORRECTED NYSTRÖM METHOD

Seçil Kılınç
M.S. in Electrical and Electronics Engineering
Supervisor: Prof. Dr. Levent Gürel
September 2010

The locally corrected Nyström (LCN) method is used to solve integral equations with high accuracy and efficiency. Unlike commonly used methods, the LCN method employs high-order basis functions on high-order surfaces. Hence, the number of unknowns in the electromagnetic problem decreases substantially, this also reduces the total solution time of the problem. In this thesis, electromagnetic scattering problems for arbitrary, three-dimensional, and conducting geometries are solved with the LCN method. Both the electric-field integral equation (EFIE) and the magnetic-field integral equation (MFIE) are implemented. The solution time for Duffy integrals is reduced significantly by modifying the Duffy transform. Then, mixed-order basis functions are implemented to accurately represent the charge density for EFIE. Finally, both the accuracy and the efficiency (in terms of solutions times and the number of unknowns) of the LCN method are compared with the method of moments and the multilevel fast multipole algorithm.

Keywords: The locally corrected Nyström (LCN) method, electromagnetic scattering, surface integral equations, high-order geometry modeling, high-order basis functions, the Duffy transform, radar cross section.

ÖZET

ELEKTROMANYETİK SAÇILIM PROBLEMLERİNİN LOKAL OLARAK DÜZELTİLMİŞ NYSTRÖM YÖNTEMİYLE ÇÖZÜMÜ

Seçil Kılınç
Elektrik ve Elektronik Mühendisliği Bölümü Yüksek Lisans
Tez Yöneticisi: Prof. Dr. Levent Gürel
Eylül 2010

Lokal olarak düzeltilmiş Nyström (LDN) yöntemi, integral denklemlerinin yüksek doğrulukta ve verimlilikte çözümleri için kullanılan bir metottur. Bu yöntemde düzlemsel üçgenler yerine, yüksek dereceli yüzeyler üzerinde, yüksek dereceli temel fonksiyonları kullanılır. Bu sayede, elektromanyetik problemdeki bilinmeyen sayısı azalmakta ve böylece problemin çözüm süresi önemli ölçüde kısalmaktadır. Bu tezde, üç boyutlu, karmaşık, mükemmel iletken cisimler içeren saçılım problemlerinin LDN yöntemi ile yüksek doğrulukta çözümleri gerçekleştirilmiş ve çözüm süreleri ile bilinmeyen sayıları momentler metodu ve çok seviyeli hızlı çokkutup yönteminden elde edilen sonuçlar ile karşılaştırılmıştır. LDN yöntemi hem elektrik-alan integral denklemi (EAİD), hem de manyetik-alan integral denklemine (MAİD) uygulanmıştır. Duffy dönüşümünde bazı değişiklikler yapılarak toplam çözüm zamanında büyük ölçüde azalma sağlanmıştır. Ayrıca, tam dereceli temel fonksiyonları yerine karışık dereceli temel fonksiyonları kullanılarak EAİD'de yükün doğru modellenmesi sağlanmıştır.

Anahtar kelimeler: Lokal olarak düzeltilmiş Nyström (LDN) yöntemi, elektromanyetik saçılım, yüzey integral denklemleri, yüksek dereceli geometri modelleme, yüksek dereceli temel fonksiyonları, Duffy dönüşümü, radar kesit alanı.

ACKNOWLEDGMENTS

I would like to express my deepest gratitude to my supervisor Prof. Levent Gürel, for his supervision, suggestions, and encouragement throughout the development of this thesis.

I would to like to thank to Prof. Ayhan Altıntaş and Assoc. Prof. Özlem Aydın Çivi for participating in my thesis committee and for accepting to read and review this thesis.

I am also thankful to the former and current researchers of the Bilkent University Computational Electromagnetics Research Center (BiLCEM), especially to Özgür Salih Ergül, for their cooperation and accompaniment in my studies. I would not be able to conduct high-quality research without their contributions.

My special thanks go to each member of my family for their endless love and patience.

Last but not least, thanks to Burak Tiryaki for being in my life, for witnessing every moment of this process, and for motivating me all the time.

This work was supported by the Scientific and Technical Research Council of Turkey (TUBITAK) through a M.S. scholarship.

Contents

List of Figures

List of Tables

To My Family...
Aileme...

Chapter 1

Introduction

The aim of computational electromagnetics is to solve electromagnetic problems in the computer simulation environment by using integral equations that are derived from Maxwell's equations that can be written in phasor form with the $e^{-i\omega t}$ time convention as follows

$$\nabla \times \boldsymbol{H}(\boldsymbol{r}) = -i\omega \boldsymbol{D}(\boldsymbol{r}) + \boldsymbol{J}(\boldsymbol{r}), \tag{1.1}$$

$$\nabla \times \boldsymbol{E}(\boldsymbol{r}) = i\omega \boldsymbol{B}(\boldsymbol{r}), \tag{1.2}$$

$$\nabla \cdot \boldsymbol{D}(\boldsymbol{r}) = \rho(\boldsymbol{r}), \tag{1.3}$$

$$\nabla \cdot \boldsymbol{B}(\boldsymbol{r}) = 0. \tag{1.4}$$

In an electromagnetic scattering problem, an arbitrary, three-dimensional (3-D) object is illuminated with an external electromagnetic source. Then, scattered electromagnetic fields from the object are simulated using numerical methods. Advances in computer technology have led to the development of these numerical methods to be applied to very large electromagnetic problems.

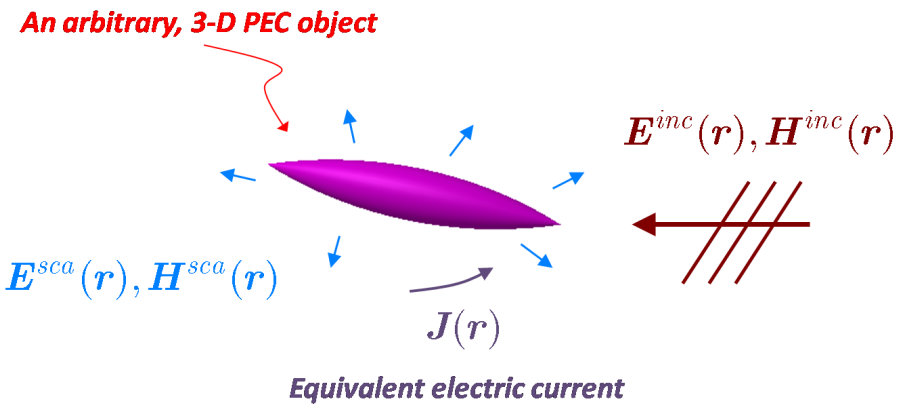

Figure 1.1: Solution of an electromagnetic scattering problem.

1.1 Historical Background

In order to solve electromagnetic scattering and radiation problems, the method of moments (MoM) [1] is a widely used method. The memory requirement of this method is $\mathcal{O}(N^2)$, where N is the number of unknowns. In addition, the required time for the direct solution is $\mathcal{O}(N^3)$. So, as the number of unknowns increases, this method becomes inefficient.

The fast multipole method (FMM), which is much more efficient than MoM, was developed for the solution of electromagnetic scattering and radiation problems [2],[3]. FMM is based on the iterative solution of the linear system that is obtained from the discretization of integral equations. Complexity of matrix-vector computations and memory requirement drops to $\mathcal{O}(N^{1.5})$ with this method. A few years later after the development of the method, FMM is extended to its multilevel version. The new method is called the multilevel fast multipole algorithm (MLFMA) [4],[5], which further reduces the computational complexity and memory requirement to the orders of $\mathcal{O}(N \log N)$.

In MLFMA, the object is placed into a cubic box, and the computational domain is divided into subdomains (clusters) recursively. Then, interactions between testing and basis elements are calculated in a group-by-group manner. This calculation is completed in three steps: aggregation, translation, and disaggregation. In the aggregation step, radiated fields are calculated from the lowest to the highest level. These radiated fields are translated into incoming fields in the translation step. Finally, in the disaggregation step, total incoming fields at the cluster centers are calculated from the highest to the lowest level.

Aforementioned methods typically employ low-order basis and testing functions, such as Rao-Wilton-Glisson (RWG) functions [6]. As mentioned above, if increased accuracy is required from these methods, computational resources increase significantly. When the number of unknowns is increased by a factor, the error also reduces with the same factor. That is, these methods are linearly convergent. In contrast, a high-order method like the locally corrected Nyström (LCN) method [7],[8],[9] can provide exponential convergence. Moreover, instead of remeshing for higher accuracies, the error convergence can be increased exponentially simply by increasing the order of the underlying quadrature rule. The computation of local correction matrix elements has a complexity of $\mathcal{O}(N)$ and these computations require the calculation of single integrations unlike the double integrations of MoM and related methods. Furthermore, the step involving the filling of impedance matrix consists of nothing more than a point-to-point kernel evaluation, which is easy to calculate. As a result, the use of a high-order method with a point-based discretization substantially reduces the required amount of computational resources.

1.2 The Objective and Overview of the Thesis

In this thesis, a high-order method, called the LCN method is investigated. In Chapter 2, a brief introduction to general properties of the method will be introduced. In order to model geometries, some commercial programs are used. The exported data of these programs are manipulated in a Fortran program to make this data compatible with curvilinear modeling. Details of high-order geometry modeling will be discussed in Chapter 2.

In Chapters 3 and 4, the LCN method is applied to the electric-field integral equation (EFIE) and magnetic-field integral equation (MFIE), respectively. The process of local correction both on self patches and near patches are presented in these chapters. For the singularity of local correction integrands, the Duffy transform is implemented on the self patch. For near patches, there is no singularity, but interactions between testing and basis points are quite high. To overcome this problem, adaptive quadrature rules are developed. Chapter 5 contains details for the Duffy transform and adaptive integration.

To correctly represent the charge continuity relation, mixed-order basis functions are used. Effects of using polynomial complete basis functions or mixed-order basis functions on the current density and charge density will be presented in Chapter 6 on a patch example. Finally, in Chapter 7, radar-cross-sections (RCS) of several real-life geometries will be shown. The accuracy and efficiency of the LCN method will be illustrated by comparing results with Bilkent University Computational Electromagnetics Research Center (BiLCEM) MLFMA solver, whose accuracy is shown in several resources [10],[11],[12].

Chapter 2

The Locally Corrected Nyström Method

The MoM discretization procedure is widely used for the solution of electromagnetic scattering problems, and in most of the MoM-based codes, low-order basis and testing functions such as RWG functions are employed. Unfortunately, these techniques have some disadvantages. Codes employing RWG functions realize linear convergence. Hence, when increased accuracy is required from the simulation, computational resources increase significantly. In this research, as an alternative to MoM, the LCN method will be investigated.

One advantage of the LCN method over MoM is that in contrast to linear convergence, the LCN method is exponentially convergent. This method employs a quadrature rule to discretize the integral equation directly. Moreover, instead of remeshing, only the quadrature rule order is increased for higher accuracies. The computation of point-to-point interactions are easy and requires low-rank algebra, while for the computation of MoM matrix elements double integrations are calculated on triangles. As a result of this, the point-based Nyström discretization reduces the precomputation time substantially. For the same level

of solution accuracy with a low-order technique, the LCN method requires less computational resources, such as time and memory.

In this chapter, first, the conventional Nyström method will be introduced. The problem with the conventional Nyström method is that it can only be applied to regular kernels. However, the Helmholtz kernel becomes singular when the source and observation point coincides with each other. Then, to handle this singularity, a local correction scheme will be presented, which was first introduced by J. Strain [13]. The local correction scheme basically requires the calculation of new specialized quadrature rule weights for the singular kernel to make the quadrature rule high-order accurate. This enhanced Nyström method will be investigated in this chapter. Finally, high-order surface modeling will be described with several examples.

2.1 The Classical Nyström Method

The classical Nyström method provides efficient and accurate solutions for the electromagnetic problems with regular kernels. Consider the following integral equation:

$$\phi(\boldsymbol{r}) = \int_S d\boldsymbol{r}' K(\boldsymbol{r}, \boldsymbol{r}') J(\boldsymbol{r}'), \tag{2.1}$$

where $\phi(\boldsymbol{r})$ is a known forcing function evaluated at $\boldsymbol{r}$, $K(\boldsymbol{r}, \boldsymbol{r}')$ is a linear kernel, and $J(\boldsymbol{r}')$ is an unknown current density. The Nyström method approximates the integral with an N-point quadrature rule as

$$\phi(\boldsymbol{r}) = \sum_{n=1}^{N} \omega_n K(\boldsymbol{r}, \boldsymbol{r}_n) J(\boldsymbol{r}_n) \tag{2.2}$$

where $\boldsymbol{r}_n$ are quadrature points, and ω_n represents weights of the quadrature rule. By sampling (2.2) at N quadrature points leads to a square linear system

of equations with m-th row expressed as

$$\phi(\boldsymbol{r}_m) = \sum_{n=1}^{N} \omega_n K(\boldsymbol{r}_m, \boldsymbol{r}_n) J(\boldsymbol{r}_n). \tag{2.3}$$

This linear system provides a solution for the unknown current density at N discrete points. If the kernel is regular and the geometry is smooth, the accuracy of the method can be adjusted with the quadrature rule order.

2.2 The Locally Corrected Nyström Method

If the kernel is infinite when $\boldsymbol{r}_m = \boldsymbol{r}_n$, the classical Nyström method becomes inconvenient. This problem is handled with local corrections. The idea of local corrections is to adjust the quadrature weights that are required to make the quadrature rule high-order accurate. Fortunately, these corrections are only calculated in the vicinity of the singularity. The new coefficients are combined with the discretized kernel elements to obtain the final form of the corrected kernel, $\bar{G}_{mn_{ij}}$, as

$$\bar{G}_{mn_{ij}} = \begin{cases} G_{mn_{ij}}, & m \neq n \\ L_{mn_{ij}}, & m = n. \end{cases} \tag{2.4}$$

Assume that the current density is expanded into a set of known basis functions $f_j^k(\boldsymbol{r}_n)$ that are distributed over the surface. In this thesis, orthogonal subdomain functions representing the underlying quadrature rules are assumed. If the integrand is a regular function, the basis functions should be regular functions of increasing order. In locations where the singular behavior of integrand is expected, such as edges and corners, it is desired to apply a different quadrature rule and use appropriate basis functions. To this end, for smooth geometries, an N-point Gauss-Legendre quadrature rule is defined. Similarly, an N-point Gauss-Jacobi quadrature rule is defined over the surface for geometries that lead to currents with known edge singularities. The choice of testing functions goes

together with the choice of quadrature rule. Consequently, an N-point Gauss-Legendre or N-point Gauss-Jacobi quadrature rule is defined over the surface of the geometry. Then, the entries L_{mn} can be expressed in terms of the equations

$$\sum_{n=1}^{N} \omega_n L_{mn} f_k(\boldsymbol{r}_n) = \int_S d\boldsymbol{r}' K(\boldsymbol{r}, \boldsymbol{r}') f_k(\boldsymbol{r}') - \sum_{n=1, n\neq m}^{N} \omega_n K_{mn} f_k(\boldsymbol{r}_n). \tag{2.5}$$

Then, the linear system of equations can be solved for the m-th row of L_{mn} using a direct LU factorization or singular value decomposition.

2.3 High-Order Geometry Modelling

Nyström discretization is of little benefit without a high-order surface modeling. Representing a curved surface with flat facets limits the rate of convergence to low order even if the rest of the discretization method is high order. In the ideal case, the internal representation of the surface exactly defines the physical surface.

In this research, an approximate representation of the surface is employed using biquadratic surfaces. A CAD program is used for modeling the geometry and meshing it with quadratic elements as shown in the examples in Figure 2.1. Next, the output of the CAD program is processed in a Fortran program to merge quadratic meshes to form larger curved patches. Since on the larger patches higher order quadrature rule and basis functions can be defined, the large smooth curvilinear patches are preferred in the LCN method. This is because of the fact that the high-order basis converge more rapidly than low-order basis. Consequently, after obtaining the curvilinear patches, quadrature rule points are placed on the surface by using the biquadratic surface formulation as shown in Figure 2.2. As mentioned before, the difference between the high-order surface description and a faceted description is that the subdivision of the surface into

curvilinear patches is done once and to improve the accuracy it is only required to increase the order of the quadrature rule.

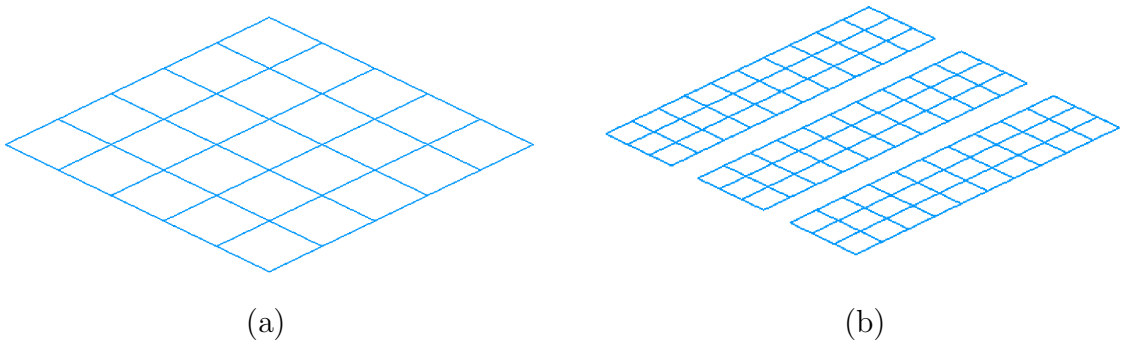

(a) (b)

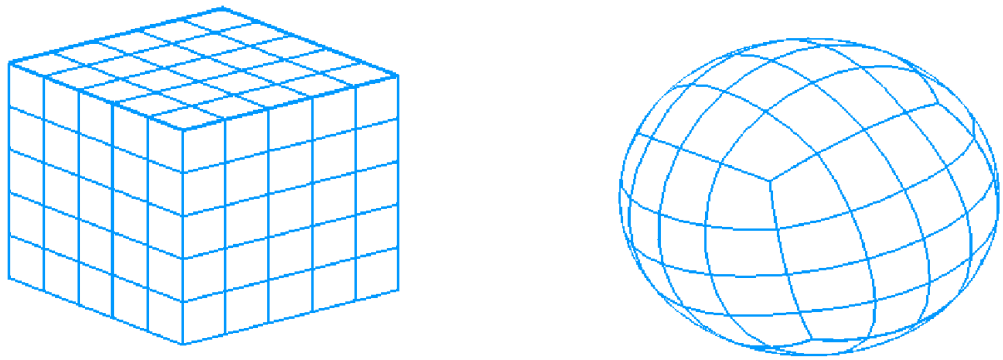

(c) (d)

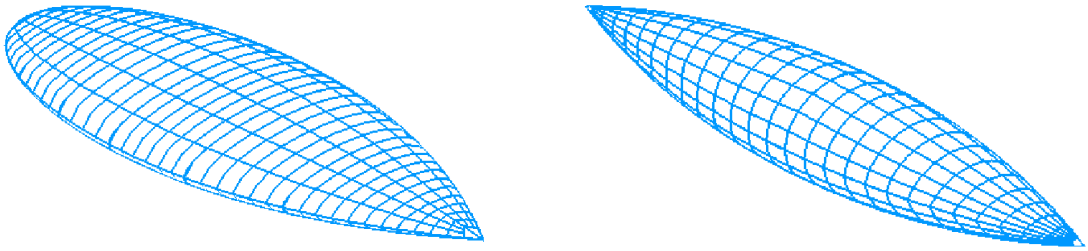

(e) (f)

Figure 2.1: Discretization of various geometries with quadratic meshes: (a) square patch, (b) finite array of strips, (c) cube, (d) sphere, (e) NASA almond, and (f) ogive.

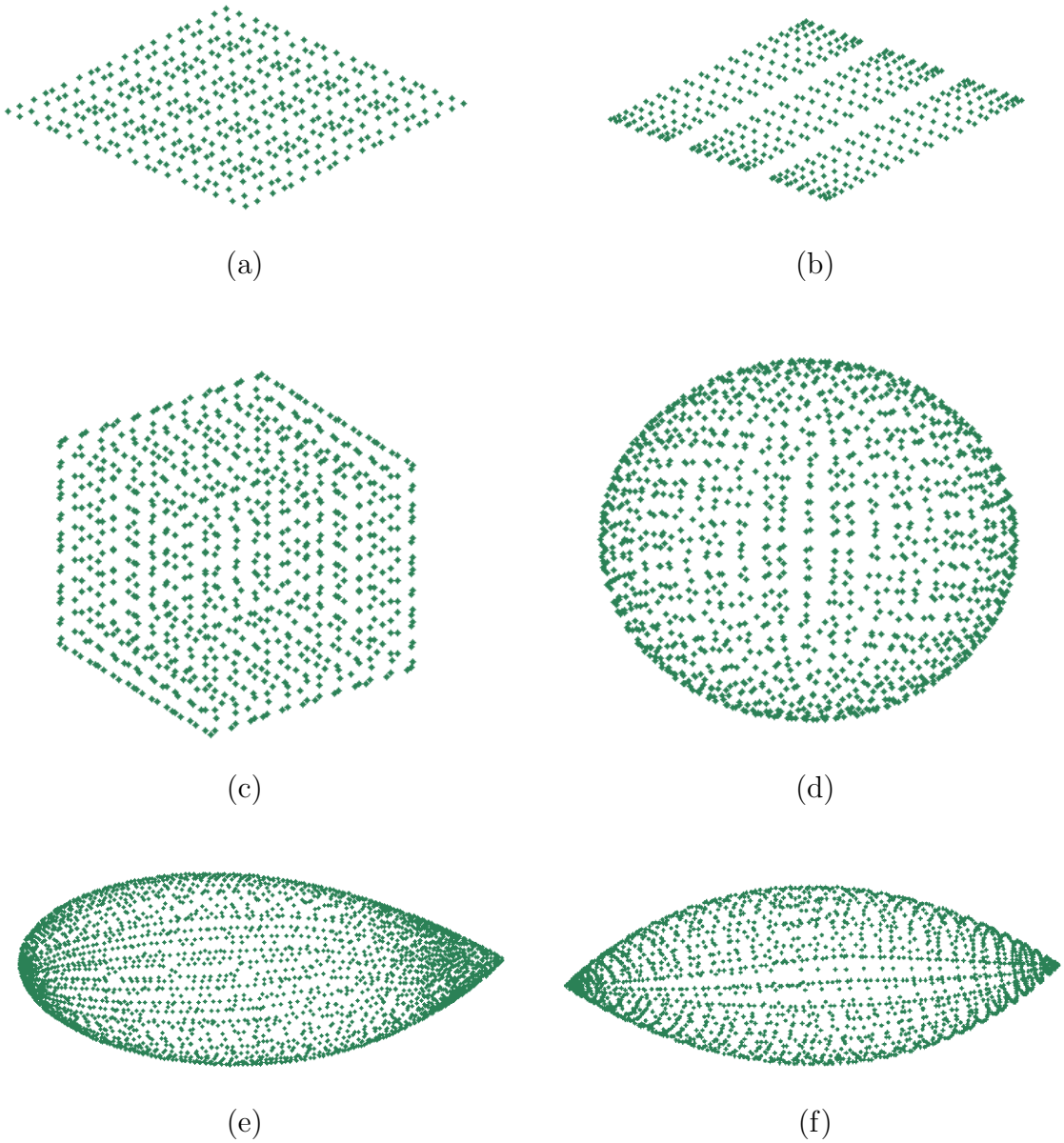

Figure 2.2: Nyström discretization of various geometries: (a) square patch, (b) finite array of strips, (c) cube, (d) sphere, (e) NASA almond, and (f) ogive.

Chapter 3

Application of the Locally Corrected Nyström Method to the Electric-Field Integral Equation

In this chapter, the application of the LCN method to the electric-field integral equation (EFIE) is introduced. The EFIE is discretized on quadrature points, and it is tested with unitary vectors, which are defined on each point. Then, for the singularity, local corrections will be introduced. Local corrections are implemented on both the self patches and the near patches.

3.1 Formulation

The boundary condition about the tangential component of the electric field for a perfectly conducting surface in free-space is,

$$\hat{\boldsymbol{t}} \cdot \boldsymbol{E}^{inc}(\boldsymbol{r}) + \hat{\boldsymbol{t}} \cdot \boldsymbol{E}^{sca}(\boldsymbol{r}) = 0, \tag{3.1}$$

where $\boldsymbol{r}$ is the observation point on the surface of the geometry, $\boldsymbol{E}^{inc}$ is the incident and $\boldsymbol{E}^{sca}$ is the scattered electric field due to external electromagnetic sources. The scattered field can be expressed as

$$\boldsymbol{E}^{sca}(\boldsymbol{r}) = ik\eta \int_S d\boldsymbol{r}' \bar{\boldsymbol{G}}(\boldsymbol{r}, \boldsymbol{r}') \cdot \boldsymbol{J}(\boldsymbol{r}'), \tag{3.2}$$

where $k = \omega\sqrt{\mu\epsilon} = 2\pi/\lambda$ is the wavenumber, $\eta = \sqrt{\mu/\epsilon}$ is the intrinsic impedance and $\bar{\boldsymbol{G}}(\boldsymbol{r}, \boldsymbol{r}')$ is the dyadic Green's function which can be defined as

$$\bar{\boldsymbol{G}}(\boldsymbol{r}, \boldsymbol{r}') = \left[\bar{\boldsymbol{I}} + \frac{\nabla\nabla}{k^2}\right] g(\boldsymbol{r}, \boldsymbol{r}') \tag{3.3}$$

and

$$g(\boldsymbol{r}, \boldsymbol{r}') = \frac{\exp(ikR)}{4\pi R} \tag{3.4}$$

is the free-space Green's function. Substituting (3.3) into (3.2), the scattered electric field can be rewritten as

$$\boldsymbol{E}^{sca}(\boldsymbol{r}) = ik\eta \int_S d\boldsymbol{r}' \boldsymbol{J}(\boldsymbol{r}') g(\boldsymbol{r}, \boldsymbol{r}') + i\frac{\eta}{k} \nabla \int_S d\boldsymbol{r}' \nabla g(\boldsymbol{r}, \boldsymbol{r}') \cdot \boldsymbol{J}(\boldsymbol{r}'). \tag{3.5}$$

Then, the EFIE is formed by substituting the scattered field expression into the boundary condition as

$$\hat{\boldsymbol{t}} \cdot \boldsymbol{E}^{inc}(\boldsymbol{r}) = ik\eta \hat{\boldsymbol{t}} \cdot \int_S d\boldsymbol{r}' \boldsymbol{J}(\boldsymbol{r}') g(\boldsymbol{r}, \boldsymbol{r}') + i\frac{\eta}{k} \hat{\boldsymbol{t}} \cdot \nabla \int_S d\boldsymbol{r}' \nabla g(\boldsymbol{r}, \boldsymbol{r}') \cdot \boldsymbol{J}(\boldsymbol{r}'). \tag{3.6}$$

In the LCN method, it is assumed that the surface is discretized with the curvilinear patches. These curvilinear patches have the property that, they can be uniquely described by a two-dimensional space with the parameters

$(u_1, u_2) \in (0, 1)$. There are two independent unitary vectors defined for this space. These vectors are tangential to the surface [14] and they are defined as

$$\boldsymbol{a}_i = \frac{\partial \boldsymbol{r}(u_1, u_2)}{\partial u_i}, \qquad i = 1, 2 \tag{3.7}$$

where $\boldsymbol{r}(u_1, u_2)$ defines the biquadratic surfaces in this thesis. A biquadratic surface is expressed with the following formulation, which will also be mentioned in Appendix B.

$$\boldsymbol{r}(u_1, u_2) = \sum_{i=0}^{2} \sum_{j=0}^{2} \boldsymbol{a}_{ij} (u_1)^i (u_2)^j. \tag{3.8}$$

Then, by testing (3.6) with this unitary vectors, we obtain

$$-\boldsymbol{a}_i \cdot \boldsymbol{E}^{inc}(\boldsymbol{r}) = ik\eta \boldsymbol{a}_i \cdot \int_S d\boldsymbol{r}' \boldsymbol{J}(\boldsymbol{r}') g(\boldsymbol{r}, \boldsymbol{r}') + i\frac{\eta}{k} \boldsymbol{a}_i \cdot \nabla \int_S d\boldsymbol{r}' \nabla g(\boldsymbol{r}, \boldsymbol{r}') \cdot \boldsymbol{J}(\boldsymbol{r}'). \tag{3.9}$$

There is a double gradient operation on the second term of. By operating it on the Green's function, the integral can be divided into smaller parts. Furthermore, the integral is separated in its real and imaginary components by first expressing the Green's function in terms of its real and imaginary parts. For this purpose, the Green's function is rewritten as

$$g(\boldsymbol{r}, \boldsymbol{r}') = g^R(\boldsymbol{r}, \boldsymbol{r}') + ig^I(\boldsymbol{r}, \boldsymbol{r}') = \frac{1}{4\pi} \left[\frac{\cos(kR)}{R} + i\frac{\sin(kR)}{R} \right], \tag{3.10}$$

where $R = |\boldsymbol{R}| = |\boldsymbol{r} - \boldsymbol{r}'|$.

By applying the first gradient operation on the real part of the Green's function, we obtain

$$\nabla g^R(\boldsymbol{r}, \boldsymbol{r}') = -\frac{1}{4\pi} \left(\frac{kR\sin(kR) + \cos(kR)}{R^3} \right) \boldsymbol{R}. \tag{3.11}$$

Similarly, by applying the first gradient operation on the imaginary part of the Green's function, we obtain

$$\nabla g^I(\boldsymbol{r}, \boldsymbol{r}') = \frac{1}{4\pi} \left(\frac{kR\cos(kR) - \sin(kR)}{R^3} \right) \boldsymbol{R}. \tag{3.12}$$

Then, the real part of the second term of (3.9) can be written as

$$\boldsymbol{a}_i \cdot \nabla \int_S d\boldsymbol{r}' \nabla g^R(\boldsymbol{r}, \boldsymbol{r}') \cdot \boldsymbol{J}(\boldsymbol{r}') = -\boldsymbol{a}_i \cdot \nabla \int_S d\boldsymbol{r}' \left(\frac{kR\sin(kR) + \cos(kR)}{4\pi R^3} \right) \boldsymbol{R} \cdot \boldsymbol{J}(\boldsymbol{r}'), \tag{3.13}$$

where

$$\begin{aligned} \boldsymbol{a}_i \cdot \nabla \left[\left(\frac{kR\sin(kR) + \cos(kR)}{R^2} \right) \left(\frac{\boldsymbol{R} \cdot \boldsymbol{J}(\boldsymbol{r}')}{R} \right) \right] = \\ \boldsymbol{a}_i \cdot \left[\nabla \left(\frac{kR\sin(kR) + \cos(kR)}{R^2} \right) \left(\frac{\boldsymbol{R} \cdot \boldsymbol{J}(\boldsymbol{r}')}{R} \right) \right. \\ \left. + \nabla \left(\frac{\boldsymbol{R} \cdot \boldsymbol{J}(\boldsymbol{r}')}{R} \right) \left(\frac{kR\sin(kR) + \cos(kR)}{R^2} \right) \right]. \end{aligned} \tag{3.14}$$

Evaluating the gradient operator on the first term of the right-hand-side we obtain

$$\nabla \left(\frac{kR\sin(kR) + \cos(kR)}{R^2} \right) = \left(\frac{k^2\cos(kR)}{R} - \frac{3k\sin(kR)}{R^2} - \frac{2\cos(kR)}{R^2} \right) \frac{\boldsymbol{R}}{R}, \tag{3.15}$$

and applying the following vector identity on the second term

$$\boldsymbol{a}_i \cdot \nabla \left(\frac{\boldsymbol{R} \cdot \boldsymbol{J}(\boldsymbol{r}')}{R} \right) = \frac{\boldsymbol{a}_i \cdot \boldsymbol{J}(\boldsymbol{r}')}{R} - \frac{(\boldsymbol{a}_i \cdot \boldsymbol{R})(\boldsymbol{J}(\boldsymbol{r}') \cdot \boldsymbol{R})}{R^3}, \tag{3.16}$$

the final expression for the real part as is obtained as

$$\begin{aligned} \boldsymbol{a}_i \cdot \nabla \left[\left(\frac{kR\sin(kR) + \cos(kR)}{R^2} \right) \left(\frac{\boldsymbol{R} \cdot \boldsymbol{J}(\boldsymbol{r}')}{R} \right) \right] = -\boldsymbol{a}_i \cdot \boldsymbol{J}(\boldsymbol{r}') k^3 \left[\frac{\sin(kR)}{(kR)^2} + \frac{\cos(kR)}{(kR)^3} \right] \\ + (\boldsymbol{a}_i \cdot \boldsymbol{R})(\boldsymbol{J}(\boldsymbol{r}') \cdot \boldsymbol{R}) k^5 \left[\frac{3\cos(kR)}{(kR)^5} + \frac{3\sin(kR)}{(kR)^4} - \frac{\cos(kR)}{(kR)^3} \right]. \end{aligned} \tag{3.17}$$

Similar calculations can be done for the imaginary part to obtain

$$\begin{aligned} \boldsymbol{a}_i \cdot \nabla \left[\left(\frac{kR\cos(kR) - \sin(kR)}{R^2} \right) \left(\frac{\boldsymbol{R} \cdot \boldsymbol{J}(\boldsymbol{r}')}{R} \right) \right] = \boldsymbol{a}_i \cdot \boldsymbol{J}(\boldsymbol{r}') k^3 \left[\frac{\cos(kR)}{(kR)^2} - \frac{\sin(kR)}{(kR)^3} \right] \\ + (\boldsymbol{a}_i \cdot \boldsymbol{R})(\boldsymbol{J}(\boldsymbol{r}') \cdot \boldsymbol{R}) k^5 \left[\frac{3\sin(kR)}{(kR)^5} - \frac{3\cos(kR)}{(kR)^4} - \frac{\sin(kR)}{(kR)^3} \right]. \end{aligned} \tag{3.18}$$

3.1.1 Discretization

In the LCN method, the surface current density, $\boldsymbol{J}(\boldsymbol{r}')$, is expressed in terms of two components that correspond to the projection onto the two unitary vectors that are independent from each other. Hence, to discretize the integral equations, the current can be approximated as

$$\boldsymbol{J}(\boldsymbol{r}_n) = \frac{\boldsymbol{a}_{1n} J_{1n} + \boldsymbol{a}_{2n} J_{2n}}{\sqrt{g_n}}, \tag{3.19}$$

where J_{1n} and J_{2n} are unknown constant coefficients to be calculated at numerical quadrature points, $\boldsymbol{a}_{1n}$ and $\boldsymbol{a}_{2n}$ are unitary vectors as defined in (3.7), and $\sqrt{g_n}$ is the Jacobian evaluated at $\boldsymbol{r}_n$. The Jacobian for a surface integration can be calculated from the coefficients of the metric tensor as

$$\sqrt{g_n} = |\boldsymbol{a}_{1n} \times \boldsymbol{a}_{2n}| = \sqrt{g_{11} g_{22} - g_{12}^2}, \tag{3.20}$$

where

$$g_{ij} = \boldsymbol{a}_i \cdot \boldsymbol{a}_j. \tag{3.21}$$

For the numerical solution of the EFIE, the integrals are discretized by applying numerical quadrature to (3.9), and by using (3.19) as

$$\begin{aligned} -\boldsymbol{a}_{im} \cdot \boldsymbol{E}^{inc}(\boldsymbol{r}_m) = ik\eta \sum_{p=1}^{P} \sum_{n=1}^{N} \boldsymbol{a}_{im} \cdot \left(\frac{\boldsymbol{a}_{1n} J_{1n} + \boldsymbol{a}_{2n} J_{2n}}{\sqrt{g_n}} \right) g(\boldsymbol{r}_m, \boldsymbol{r}_n) \sqrt{g_n} \omega_n \\ + i \frac{\eta}{k} \sum_{p=1}^{P} \sum_{n=1}^{N} \boldsymbol{a}_{im} \cdot \nabla \left(\nabla g(\boldsymbol{r}_m, \boldsymbol{r}_n) \cdot \frac{\boldsymbol{a}_{1n} J_{1n} + \boldsymbol{a}_{2n} J_{2n}}{\sqrt{g_n}} \right) \sqrt{g_n} \omega_n. \end{aligned} \tag{3.22}$$

In this equation, it is assumed that there are a total of P curvilinear patches on the surface S, and N quadrature points on each of the patches. We can also express (3.22) as a linear system of equations

$$\begin{bmatrix} -\boldsymbol{a}_{1m} \cdot \boldsymbol{E}^{inc}(\boldsymbol{r}_m) \\ -\boldsymbol{a}_{2m} \cdot \boldsymbol{E}^{inc}(\boldsymbol{r}_m) \end{bmatrix} = \begin{bmatrix} G_{mn_{11}} & G_{mn_{12}} \\ G_{mn_{21}} & G_{mn_{22}} \end{bmatrix} \cdot \begin{bmatrix} J_{1n} \\ J_{2n} \end{bmatrix}. \tag{3.23}$$

Further, the kernel $G_{mn_{ij}}$ can be written in terms of its real and imaginary components as

$$G_{mn_{ij}} = G^R_{mn_{ij}} + G^I_{mn_{ij}}. \tag{3.24}$$

Then, by substituting (3.17) and (3.18) into (3.22), we can write the real part of the EFIE kernel as

$$\begin{aligned} G^R_{mn_{ij}} = i\frac{\eta}{4\pi}\omega_n\Big[k^2(\boldsymbol{a}_{im}\cdot\boldsymbol{a}_{jn})\Big[\frac{\cos(kR_{mn})}{(kR_{mn})} - \frac{\sin(kR_{mn})}{(kR_{mn})^2} - \frac{\cos(kR_{mn})}{(kR_{mn})^3}\Big] \\ + k^4(\boldsymbol{a}_{im}\cdot\boldsymbol{R}_{mn})(\boldsymbol{a}_{jn}\cdot\boldsymbol{R}_{mn})\Big[3\frac{\cos(kR_{mn})}{(kR_{mn})^5} + 3\frac{\sin(kR_{mn})}{(kR_{mn})^4} - \frac{\cos(kR_{mn})}{(kR_{mn})^3}\Big]\Big], \end{aligned} \tag{3.25}$$

and the imaginary part can be written as

$$\begin{aligned} G^I_{mn_{ij}} = \frac{\eta}{4\pi}\omega_n\Big[k^2(\boldsymbol{a}_{im}\cdot\boldsymbol{a}_{jn})\Big[-\frac{\sin(kR_{mn})}{(kR_{mn})} + \frac{\sin(kR_{mn})}{(kR_{mn})^3} - \frac{\cos(kR_{mn})}{(kR_{mn})^2}\Big] \\ + k^4(\boldsymbol{a}_{im}\cdot\boldsymbol{R}_{mn})(\boldsymbol{a}_{jn}\cdot\boldsymbol{R}_{mn})\Big[\frac{\sin(kR_{mn})}{(kR_{mn})^3} - 3\frac{\sin(kR_{mn})}{(kR_{mn})^5} + 3\frac{\cos(kR_{mn})}{(kR_{mn})^4}\Big]\Big]. \end{aligned} \tag{3.26}$$

3.2 Local Corrections

From (3.10), it can be seen that the real part of the Green's function is singular, while the imaginary part is regular in the limit that the source point approaches to the observation point. This means that the derivatives of the imaginary part are also bounded. The limit value of $G^I_{mn_{ij}}$ can be calculated as

$$\lim_{m\to n} G^I_{mn_{ij}} = \frac{\eta}{4\pi}J_{jn}\omega_n\Big[-\frac{2}{3}k^2(\boldsymbol{a}_{im}\cdot\boldsymbol{a}_{jn})\Big]. \tag{3.27}$$

Hence, this term can be integrated by using the underlying quadrature rule, and do not require local corrections. On the other hand, since the real part is not regular, the quadrature rule is not sufficient to integrate $G^R_{mn_{ij}}$ accurately. The LCN method requires the local correction of this term.

$$\lim_{m\to n} G^R_{mn_{ij}} = \infty. \tag{3.28}$$

In the local correction process, the unknown current is expressed in terms of known basis functions as

$$\boldsymbol{J}(\boldsymbol{r}_n) = \frac{\boldsymbol{a}_{1n} f_1^k(\boldsymbol{r}_n) + \boldsymbol{a}_{2n} f_2^k(\boldsymbol{r}_n)}{\sqrt{g_n}}, \tag{3.29}$$

where $f_j^k(\boldsymbol{r}_n)$ are chosen as the product of two Legendre polynomials that are defined in each parametric direction with the following orders

$$f_j^k(\boldsymbol{r}_n) = P_{k_1}(u_1) P_{k_2}(u_2), \qquad (k_1, k_2 : 0, 1, .., N-1). \tag{3.30}$$

In general, there are two types of local correction methods. The first one is patch-based correction, and the second one is entire-domain correction [14]. In the patch-based correction, for each point, the new quadrature rule coefficients are calculated for each patch. The support of basis functions are restricted to the corresponding patch. So, the advantage of this method is, the linear system of equations required to solve the new quadrature weights are small and well-conditioned.

On the other hand, for the entire-domain correction, the basis functions distributed over the entire surface are supported. So, local correction coefficients are solved for a larger area, and linear systems to be solved are poorly-conditioned as expected.

In this thesis, local corrections are introduced on patches, for each observation point $\boldsymbol{r}_m$. For this purpose, the Legendre polynomials are distributed on the patch to be corrected, and the field radiated by these assumed currents is calculated at $\boldsymbol{r}_m$. For each observation point, the local correction on a patch can be expressed as

$$\begin{aligned}\sum_{n=1}^{N} L_{mn_{ij}} f_j^k(\boldsymbol{r}_n)\omega_n = {} & ik\eta \int_S d\boldsymbol{r}'(\boldsymbol{a}_{im} \cdot \boldsymbol{a}_j{}') g^R(\boldsymbol{r}_m, \boldsymbol{r}') f_j^k(\boldsymbol{r}')/\sqrt{g'} \\ & + i\frac{\eta}{k} \boldsymbol{a}_{im} \cdot \nabla \int_S d\boldsymbol{r}' \nabla g^R(\boldsymbol{r}_m, \boldsymbol{r}') \cdot \boldsymbol{a}_j{}' f_j^k(\boldsymbol{r}')/\sqrt{g'} \\ & - \sum_{n=1, n\neq m}^{N} G^R_{mn_{ij}} f_j^k(\boldsymbol{r}')\omega_n, \end{aligned} \tag{3.31}$$

where the first two terms on the right-hand side correspond to the exact evaluation of the integral on the patch, and the third term corresponds to the numerical approximation that is calculated using the underlying quadrature rule and by excluding the singular point. When the approximate result is subtracted from the exact value, a residual error is obtained. Then, this error is modeled as follows, to calculate the local correction coefficients

$$\begin{bmatrix} \omega_1 f_j^1(\boldsymbol{r}_1) & \omega_2 f_j^1(\boldsymbol{r}_2) & \dots & \omega_N f_j^1(\boldsymbol{r}_N) \\ \omega_1 f_j^2(\boldsymbol{r}_1) & \omega_2 f_j^2(\boldsymbol{r}_2) & \dots & \omega_N f_j^2(\boldsymbol{r}_N) \\ \vdots & & & \vdots \\ \omega_1 f_j^k(\boldsymbol{r}_1) & \omega_2 f_j^k(\boldsymbol{r}_2) & \dots & \omega_N f_j^k(\boldsymbol{r}_N) \end{bmatrix} \cdot \begin{bmatrix} L_{m1_{ij}} \\ L_{m2_{ij}} \\ \vdots \\ L_{mN_{ij}} \end{bmatrix} = \begin{bmatrix} E_m^1 \\ E_m^2 \\ \vdots \\ E_m^k \end{bmatrix}. \tag{3.32}$$

Finally, after obtaining the local correction coefficients for all of the observation points, the impedance matrix is updated as follows

$$\bar{G}_{mn_{ij}} = \begin{cases} G_{mn_{ij}}, & m \neq n \\ \omega_n L_{mn_{ij}}, & m = n. \end{cases} \tag{3.33}$$

3.2.1 Local Corrections for Self Patch

The integrand to be calculated during local corrections becomes hypersingular when the observation point and basis functions lie on the same patch. So, to calculate this integral efficiently with numerical quadrature rules, the hypersingular terms need to be modified. Because of this, the second term on the right-hand side of (3.31) is written as

$$\begin{aligned} \int_S d\boldsymbol{r}' \boldsymbol{a}_i \cdot \nabla \Big(\nabla g^R(\boldsymbol{r}_m, \boldsymbol{r}') \cdot \boldsymbol{J}(\boldsymbol{r}') \Big) &= - \int_S d\boldsymbol{r}' \boldsymbol{a}_i \cdot \nabla \Big(\nabla' g^R(\boldsymbol{r}_m, \boldsymbol{r}') \cdot \boldsymbol{J}(\boldsymbol{r}') \Big) \\ &= - \int_S d\boldsymbol{r}' \boldsymbol{J}(\boldsymbol{r}') \cdot \nabla_{||}{}' \Big(\boldsymbol{a}_i \cdot \nabla g^R(\boldsymbol{r}_m, \boldsymbol{r}') \Big), \end{aligned} \tag{3.34}$$

where $\nabla_{||}{}'$ is tangential to the surface. Next, using the following vector identity

$$\nabla \cdot (\phi \boldsymbol{A}) = \phi \nabla \cdot \boldsymbol{A} + \boldsymbol{A} \cdot \nabla \phi \tag{3.35}$$

(3.34) can be expressed as

$$\int_S d\boldsymbol{r}'\boldsymbol{a}_i \cdot \nabla\Big(\nabla g^R(\boldsymbol{r}_m,\boldsymbol{r}')\cdot\boldsymbol{J}(\boldsymbol{r}')\Big) = -\int_S d\boldsymbol{r}'{\nabla_{||}}'\cdot\Big[\boldsymbol{J}(\boldsymbol{r}')\big(\boldsymbol{a}_i\cdot\nabla g^R(\boldsymbol{r}_m,\boldsymbol{r}')\big)\Big] + \int_S d\boldsymbol{r}'{\nabla_{||}}'\cdot\boldsymbol{J}(\boldsymbol{r}')\big(\boldsymbol{a}_i\cdot\nabla g^R(\boldsymbol{r}_m,\boldsymbol{r}')\big). \quad (3.36)$$

Then, by using the open surface divergence theorem, the first term on the right-hand-side is written as

$$\int_S d\boldsymbol{r}'{\nabla_{||}}'\cdot\Big[\boldsymbol{J}(\boldsymbol{r}')\big(\boldsymbol{a}_i\cdot\nabla g^R(\boldsymbol{r}_m,\boldsymbol{r}')\big)\Big] = \oint_C dl'(\hat{\boldsymbol{e}}'\cdot\boldsymbol{J}(\boldsymbol{r}'))\big(\boldsymbol{a}_i\cdot\nabla g^R(\boldsymbol{r}_m,\boldsymbol{r}')\big), \quad (3.37)$$

where C is the closed contour of the surface S, and $\hat{\boldsymbol{e}}'$ is the outward normal to the contour which is also tangential to S.

The second term on the right-hand-side of (3.36) is modified as follows

$$\begin{aligned}\int_S d\boldsymbol{r}'{\nabla_{||}}'\cdot\boldsymbol{J}(\boldsymbol{r}')\big(\boldsymbol{a}_i\cdot\nabla g^R(\boldsymbol{r}_m,\boldsymbol{r}')\big) &= \int_S d\boldsymbol{r}'\nabla g^R(\boldsymbol{r}_m,\boldsymbol{r}')\cdot\Big[\boldsymbol{a}_i{\nabla_{||}}'\cdot\boldsymbol{J}(\boldsymbol{r}')\Big]\\ &= \int_S d\boldsymbol{r}'\nabla g^R(\boldsymbol{r}_m,\boldsymbol{r}')\cdot\Big[\boldsymbol{a}_i{\nabla_{||}}'\cdot\boldsymbol{J}(\boldsymbol{r}')-\boldsymbol{\kappa}'\Big]\\ &\quad+\int_S d\boldsymbol{r}'\nabla g^R(\boldsymbol{r}_m,\boldsymbol{r}')\cdot\boldsymbol{\kappa}', \end{aligned} \quad (3.38)$$

where

$$\boldsymbol{\kappa}' = {\boldsymbol{a}_i}'\Big[{\nabla_{||}}'\cdot\boldsymbol{J}(\boldsymbol{r}')|_{\boldsymbol{r}'=\boldsymbol{r}}\Big] = \frac{{\boldsymbol{a}_i}'}{\sqrt{g'}}\chi, \quad (3.39)$$

and

$$\chi = \sqrt{g}\Big[{\nabla_{||}}'\cdot\boldsymbol{J}(\boldsymbol{r}')|_{\boldsymbol{r}'=\boldsymbol{r}}\Big]. \quad (3.40)$$

The second term on the right-hand-side of (3.38) is further written as

$$\begin{aligned}\int_S d\boldsymbol{r}'\nabla g^R(\boldsymbol{r}_m,\boldsymbol{r}')\cdot\boldsymbol{\kappa}' &= -\int_S d\boldsymbol{r}'\nabla' g^R(\boldsymbol{r}_m,\boldsymbol{r}')\cdot\frac{{\boldsymbol{a}_i}'}{\sqrt{g'}}\chi\\ &= -\int_S d\boldsymbol{r}'\chi\Big(\frac{{\boldsymbol{a}_i}'}{\sqrt{g'}}\cdot\nabla' g^R(\boldsymbol{r}_m,\boldsymbol{r}')\Big)\\ &= -\int_S d\boldsymbol{r}'\chi\Big[{\nabla_{||}}'\cdot\Big(\frac{{\boldsymbol{a}_i}'}{\sqrt{g'}}g^R(\boldsymbol{r}_m,\boldsymbol{r}')\Big)-g^R(\boldsymbol{r}_m,\boldsymbol{r}')\nabla_{||}'\cdot\frac{{\boldsymbol{a}_i}'}{\sqrt{g'}}\Big]. \end{aligned} \quad (3.41)$$

Knowing that $\nabla_{||}{}' \cdot (\boldsymbol{a}_i{}'/\sqrt{g'}) = 0$ [7], we can apply the open surface divergence theorem to obtain

$$\int_S d\boldsymbol{r}' \nabla g^R(\boldsymbol{r}_m, \boldsymbol{r}') \cdot \boldsymbol{\kappa}' = -\chi \oint_C dl' \hat{\boldsymbol{e}}' \cdot \frac{\boldsymbol{a}_i{}'}{\sqrt{g'}} g^R(\boldsymbol{r}_m, \boldsymbol{r}'). \tag{3.42}$$

Finally, it is obtained that

$$\begin{aligned} \boldsymbol{a}_i \cdot \nabla \int_S d\boldsymbol{r}' \Big(\nabla g^R(\boldsymbol{r}_m, \boldsymbol{r}') \cdot \boldsymbol{J}(\boldsymbol{r}') \Big) &= \int_S d\boldsymbol{r}' \nabla g^R(\boldsymbol{r}_m, \boldsymbol{r}') \cdot \Big[\boldsymbol{a}_i \nabla_{||}{}' \cdot \boldsymbol{J}(\boldsymbol{r}') - \boldsymbol{\kappa}' \Big] \\ &\quad - \oint_C dl' (\hat{\boldsymbol{e}}' \cdot \boldsymbol{J}(\boldsymbol{r}'))(\boldsymbol{a}_i \cdot \nabla g^R(\boldsymbol{r}_m, \boldsymbol{r}')) \\ &\quad - \chi \oint_C dl' \hat{\boldsymbol{e}}' \cdot \frac{\boldsymbol{a}_i{}'}{\sqrt{g'}} g^R(\boldsymbol{r}_m, \boldsymbol{r}'). \end{aligned} \tag{3.43}$$

Then, the local correction coefficients on the self patch can be calculated by using

$$\begin{aligned} \sum_{n=1}^{N} L_{mn_{ij}} f_j^k(\boldsymbol{r}_n) \omega_n &= ik\eta \int_S d\boldsymbol{r}' (\boldsymbol{a}_{im} \cdot \boldsymbol{a}_j{}') g^R(\boldsymbol{r}_m, \boldsymbol{r}') f_j^k(\boldsymbol{r}') / \sqrt{g'} \\ &\quad + i\frac{\eta}{k} \int_S d\boldsymbol{r}' \nabla g^R(\boldsymbol{r}_m, \boldsymbol{r}') \cdot \Big[\boldsymbol{a}_{im} \nabla_{||}{}' \cdot \boldsymbol{J}(\boldsymbol{r}') - \boldsymbol{\kappa}' \Big] \\ &\quad - i\frac{\eta}{k} \oint_C dl' (\hat{\boldsymbol{e}}' \cdot \boldsymbol{J}(\boldsymbol{r}'))(\boldsymbol{a}_{im} \cdot \nabla g^R(\boldsymbol{r}_m, \boldsymbol{r}')) \\ &\quad - i\frac{\eta}{k} \chi \oint_C dl' \hat{\boldsymbol{e}}' \cdot \frac{\boldsymbol{a}_i{}'}{\sqrt{g'}} g^R(\boldsymbol{r}_m, \boldsymbol{r}') \\ &\quad - \sum_{n=1, n \neq m}^{N} G^R_{mn_{ij}} f_j^k(\boldsymbol{r}') \omega_n. \end{aligned} \tag{3.44}$$

These integrals are numerically tractable. Only the first term has a $1/R$ singularity when the region of integration contains the observation point. This singularity is handled by dividing the integration region into triangles with the observation point at one vertex. Then, this integration is performed by using the Duffy transformation. All other remaining integrals are bounded, and they are calculated by using adaptive quadrature rules.

We can look closer to these integrals. The first term on the right-hand-side of (3.44) is calculated with the Duffy transform and will be examined in details in Chapter 5. For the second integral, we should note that

$$\nabla_{||}{}' \cdot \boldsymbol{J}(\boldsymbol{r}_n) = \frac{1}{\sqrt{g_n}} \left(\boldsymbol{a}_1 \frac{\partial}{\partial u_1} + \boldsymbol{a}_2 \frac{\partial}{\partial u_2} \right) \cdot \left(\boldsymbol{a}_1 \frac{f_j^k(u_1, u_2)}{\sqrt{g_n}} + \boldsymbol{a}_2 \frac{f_j^k(u_1, u_2)}{\sqrt{g_n}} \right). \tag{3.45}$$

If $j = 1$, the current will be in the $\boldsymbol{a}_1$ direction,

$$\nabla_{||}{}' \cdot \boldsymbol{J}(\boldsymbol{r}_n) = \frac{1}{\sqrt{g_n}} \left[(\boldsymbol{a}_1 \cdot \boldsymbol{a}_1) \frac{\partial}{\partial u_1} \left(\frac{f_1^k(u_1, u_2)}{\sqrt{g_n}} \right) + (\boldsymbol{a}_2 \cdot \boldsymbol{a}_1) \frac{\partial}{\partial u_2} \left(\frac{f_1^k(u_1, u_2)}{\sqrt{g_n}} \right) \right]. \tag{3.46}$$

And, if $j = 2$, then the $\boldsymbol{a}_1$ directed component of the current will vanish,

$$\nabla_{||}{}' \cdot \boldsymbol{J}(\boldsymbol{r}_n) = \frac{1}{\sqrt{g_n}} \left[(\boldsymbol{a}_1 \cdot \boldsymbol{a}_2) \frac{\partial}{\partial u_1} \left(\frac{f_1^k(u_1, u_2)}{\sqrt{g_n}} \right) + (\boldsymbol{a}_2 \cdot \boldsymbol{a}_2) \frac{\partial}{\partial u_2} \left(\frac{f_1^k(u_1, u_2)}{\sqrt{g_n}} \right) \right], \tag{3.47}$$

where

$$\begin{aligned} \frac{\partial}{\partial u_j} \left(\frac{f_j^k(u_1, u_2)}{\sqrt{g_n(u_1, u_2)}} \right) &= \frac{1}{\sqrt{g_n(u_1, u_2)}} \frac{\partial}{\partial u_j} f_j^k(u_1, u_2) \\ &\quad - \frac{1}{2(\sqrt{g_n(u_1, u_2)})^3} f_j^k(u_1, u_2) \frac{\partial}{\partial u_j} g_n(u_1, u_2). \end{aligned} \tag{3.48}$$

Also, note that

$$\hat{\boldsymbol{e}}' dl' = d\bar{l}' \times \hat{\boldsymbol{n}}' \tag{3.49}$$

$$= \hat{\boldsymbol{x}}(dy' n_z{}' - dz' n_y{}') - \hat{\boldsymbol{y}}(dx' n_z{}' - dz' n_x{}') + \hat{\boldsymbol{z}}(dx' n_y{}' - dy' n_x{}'), \tag{3.50}$$

where $d\bar{l}' = \hat{\boldsymbol{x}} dx' + \hat{\boldsymbol{y}} dy' + \hat{\boldsymbol{z}} dz'$ and $\hat{\boldsymbol{n}}' = \hat{\boldsymbol{x}} n_x' + \hat{\boldsymbol{y}} n_y' + \hat{\boldsymbol{z}} n_z'$.

We can also split the current into its vectorial components as

$$\begin{aligned} \boldsymbol{J}(\boldsymbol{r}_n) &= \frac{a_{1n_x} f_1^k(\boldsymbol{r}_n) + \boldsymbol{a}_{2n_x} f_2^k(\boldsymbol{r}_n)}{\sqrt{g_n}} \hat{\boldsymbol{x}} \\ &\quad + \frac{a_{1n_y} f_1^k(\boldsymbol{r}_n) + \boldsymbol{a}_{2n_y} f_2^k(\boldsymbol{r}_n)}{\sqrt{g_n}} \hat{\boldsymbol{y}} \\ &\quad + \frac{a_{1n_z} f_1^k(\boldsymbol{r}_n) + \boldsymbol{a}_{2n_z} f_2^k(\boldsymbol{r}_n)}{\sqrt{g_n}} \hat{\boldsymbol{z}}. \end{aligned} \tag{3.51}$$

Then,

$$\begin{aligned} dl'(\hat{\boldsymbol{e}}' \cdot \boldsymbol{J}(\boldsymbol{r}')) &= \frac{a_{1n_x} f_1^k(\boldsymbol{r}_n) + \boldsymbol{a}_{2n_x} f_2^k(\boldsymbol{r}_n)}{\sqrt{g_n}} (dy' n_z{}' - dz' n_y{}') \\ &\quad + \frac{a_{1n_y} f_1^k(\boldsymbol{r}_n) + \boldsymbol{a}_{2n_y} f_2^k(\boldsymbol{r}_n)}{\sqrt{g_n}} (dx' n_z{}' - dz' n_x{}') \\ &\quad + \frac{a_{1n_z} f_1^k(\boldsymbol{r}_n) + \boldsymbol{a}_{2n_z} f_2^k(\boldsymbol{r}_n)}{\sqrt{g_n}} (dx' n_y{}' - dy' n_x{}') \end{aligned} \tag{3.52}$$

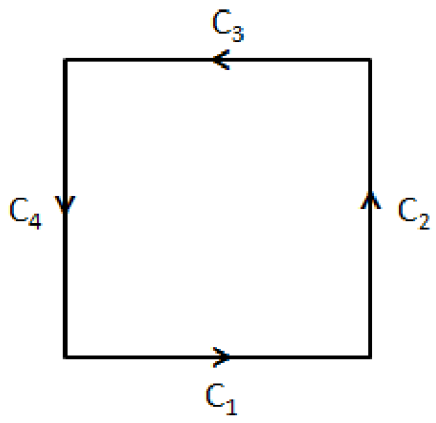

Figure 3.1: Contour integral on unitary space required for the local corrections.

More specifically, we can investigate the integrals explicitly on C_1, C_2, C_3, and C_4 as shown in Figure 3.1. We need the formulation of the surface, which is given in (3.8). For example, on $C_1 : u_2 = 0$, and $d\bar{l}' = \hat{\boldsymbol{u}}_{\mathbf{1}} du_1$. Then,

$$\boldsymbol{r}(u_1, 0) = \boldsymbol{a}_{00} + \boldsymbol{a}_{10} u_1 + \boldsymbol{a}_{20} u_1^2 \tag{3.53}$$

$$d\boldsymbol{r} = (\boldsymbol{a}_{10} + 2\boldsymbol{a}_{20} u_1) du_1 \tag{3.54}$$

Similarly, on $C_2 : u_1 = 1$, $d\bar{l}' = \hat{\boldsymbol{u}}_{\mathbf{2}} du_2$, on $C_3 : u_2 = 1$, $d\bar{l}' = -\hat{\boldsymbol{u}}_{\mathbf{1}} du_1$, and on $C_4 : u_1 = 0$, $d\bar{l}' = -\hat{\boldsymbol{u}}_{\mathbf{2}} du_2$.

3.2.2 Local Corrections for Near Patches

When the observation point lies on a different patch than the region of integration, there is no singularity. However, when we directly calculate the point-to-point interactions, the results will not be accurate enough. So, these integrals must be efficiently and accurately calculated by using adaptive quadrature rules. In this case, the local correction coefficients are obtained by solving the following

equation

$$\sum_{n=1}^{N} L_{mn_{ij}} f_j^k(\boldsymbol{r}_n)\omega_n = \int_S d\boldsymbol{r}' G^R_{mn_{ij}} f_j^k(\boldsymbol{r}') - \sum_{n=1, n\neq m}^{N} G^R_{mn_{ij}} f_j^k(\boldsymbol{r}')\omega_n, \tag{3.55}$$

where the first term corresponds to the most accurately calculated result of the integral. So, as before, from the residual error on the right-hand-side, the local correction coefficients will be calculated and these coefficients are combined with the far-interactions to form the final values of impedance matrix elements as shown in (3.33).

Chapter 4

Application of the Locally Corrected Nyström Method to the Magnetic-Field Integral Equation

This chapter is about the application of the LCN method to MFIE. Similar to EFIE, MFIE will be discretized using numerical quadrature rules. The MFIE will be tested with the unitary vectors defined on each point. For the singularity of integrals, local correction coefficients will be calculated. The Duffy transformation will be used if the region of integration contains the observation point. Else, the integrals will be calculated using adaptive quadrature rules. These concepts will be examined in details with formulations in this chapter.

4.1 Formulation

For a conducting closed surface, the boundary condition about the tangential component of the magnetic field can be written as

$$\hat{\boldsymbol{n}} \times \boldsymbol{H}^{inc}(\boldsymbol{r}) + \hat{\boldsymbol{n}} \times \boldsymbol{H}^{sca}(\boldsymbol{r}) = \boldsymbol{J}(\boldsymbol{r}), \tag{4.1}$$

where $\boldsymbol{r}$ is the observation point, $\boldsymbol{H}^{inc}$ is the incident magnetic field, and $\boldsymbol{H}^{sca}$ is the scattered magnetic field due to the induced current on the surface, which is also expressed as

$$\boldsymbol{H}^{sca}(\boldsymbol{r}) = \int_S d\boldsymbol{r}' \nabla \times g(\boldsymbol{r}, \boldsymbol{r}') \boldsymbol{J}(\boldsymbol{r}'). \tag{4.2}$$

In this equation, S represents the closed surface of a 3-D object with an arbitrary shape and $g(\boldsymbol{r}, \boldsymbol{r}')$ denotes the homogeneous-space Green's function defined as

$$g(\boldsymbol{r}, \boldsymbol{r}') = \frac{\exp(ikR)}{4\pi R}. \tag{4.3}$$

Note that, $R = |\boldsymbol{r} - \boldsymbol{r}'|$ and $k = \omega\sqrt{\mu\epsilon} = 2\pi/\lambda$ is the wavenumber.

Then, by using the boundary condition, the MFIE can be written as

$$\hat{\boldsymbol{n}} \times \boldsymbol{H}^{inc}(\boldsymbol{r}) = \boldsymbol{J}(\boldsymbol{r}) - \hat{\boldsymbol{n}} \times \int_S d\boldsymbol{r}' \nabla \times g(\boldsymbol{r}, \boldsymbol{r}') \boldsymbol{J}(\boldsymbol{r}'). \tag{4.4}$$

As for the EFIE, it is assumed that the surface of the geometry is discretized with curvilinear patches. The boundary condition of the MFIE is tested with the unitary vectors that are tangential to the surface. The unitary vectors are defined as the derivative of the surface equation with respect to the parametric coordinates as follows

$$\boldsymbol{a}_i = \frac{\partial \boldsymbol{r}(u_1, u_2)}{\partial u_i}, \qquad i = 1, 2 \tag{4.5}$$

where

$$\boldsymbol{r}(u_1, u_2) = \sum_{i=0}^{2} \sum_{j=0}^{2} \boldsymbol{a}_{ij} (u_1)^i (u_2)^j. \tag{4.6}$$

Then, the MFIE can be rewritten as

$$\boldsymbol{a}_i \cdot (\hat{\boldsymbol{n}} \times \boldsymbol{H}^{inc}(\boldsymbol{r})) = \boldsymbol{a}_i \cdot \boldsymbol{J}(\boldsymbol{r}) - \boldsymbol{a}_i \cdot \hat{\boldsymbol{n}} \times \int_S d\boldsymbol{r}' \nabla \times g(\boldsymbol{r}, \boldsymbol{r}') \boldsymbol{J}(\boldsymbol{r}'). \tag{4.7}$$

We can easily show that

$$\begin{aligned} \nabla \times g(\boldsymbol{r}, \boldsymbol{r}') \boldsymbol{J}(\boldsymbol{r}') &= g(\boldsymbol{r}, \boldsymbol{r}') \nabla \times \boldsymbol{J}(\boldsymbol{r}') - \boldsymbol{J}(\boldsymbol{r}') \times \nabla g(\boldsymbol{r}, \boldsymbol{r}') \\ &= -\boldsymbol{J}(\boldsymbol{r}') \times \nabla g(\boldsymbol{r}, \boldsymbol{r}') \\ &= \boldsymbol{J}(\boldsymbol{r}') \times \nabla' g(\boldsymbol{r}, \boldsymbol{r}'), \end{aligned} \tag{4.8}$$

and we can calculate

$$\begin{aligned} \nabla' g(\boldsymbol{r}, \boldsymbol{r}') &= \frac{1}{4\pi} \Big(\frac{\cos(kR) + kR \sin(kR)}{R^3} - i \frac{kR \cos(kR) - \sin(kR)}{R^3} \Big) \boldsymbol{R} \\ &= \frac{k^3}{4\pi} \Big(G^R(R) - i G^I(R) \Big) \boldsymbol{R}. \end{aligned} \tag{4.9}$$

As shown in this equation, the gradient of the Green's function is split into its real and imaginary components, which can also be written explicitly as

$$G^R(R) = \frac{\cos(kR) + kR \sin(kR)}{(kR)^3} \tag{4.10}$$

$$G^I(R) = \frac{\cos(kR) - (\sin(kR)/kR)}{(kR)^2} \tag{4.11}$$

Then, by substituting (4.10) and (4.11) into (4.7) we obtain the general expression for the LCN implementation of the MFIE as

$$\boldsymbol{a}_i \cdot (\hat{\boldsymbol{n}} \times \boldsymbol{H}^{inc}(\boldsymbol{r})) = \boldsymbol{a}_i \cdot \boldsymbol{J}(\boldsymbol{r}) - \boldsymbol{a}_i \cdot \hat{\boldsymbol{n}} \times \frac{k^3}{4\pi} \int_S d\boldsymbol{r}' (\boldsymbol{J}(\boldsymbol{r}') \times \boldsymbol{R}) (G^R(R) - i G^I(R)). \tag{4.12}$$

4.1.1 Principal and Limit Value Integrals

As the observation point approaches to the source point, the MFIE integral can be divided into its principal and limit value integrals as [15]

$$\begin{aligned} \boldsymbol{H}^{sca}(\boldsymbol{r}) &= \int_S d\boldsymbol{r}' \boldsymbol{J}(\boldsymbol{r}') \times \nabla' g(\boldsymbol{r}, \boldsymbol{r}') \\ &= \lim_{S_\epsilon \to 0} \int_{S - S_\epsilon} d\boldsymbol{r}' \boldsymbol{J}(\boldsymbol{r}') \times \nabla' g(\boldsymbol{r}, \boldsymbol{r}') \\ &+ \lim_{S_\epsilon \to 0} \int_{S_\epsilon} d\boldsymbol{r}' \boldsymbol{J}(\boldsymbol{r}') \times \nabla' g(\boldsymbol{r}, \boldsymbol{r}'), \end{aligned} \tag{4.13}$$

where S_ϵ is the infinitesimal surface with radius ϵ that shrinks to zero in the limit. The surface is locally planar and its normal is in the z direction as shown in Figure 4.1. Also, it is seen that the observation point is at $(0, 0, z)$ and as z goes to zero, it approaches to the surface.

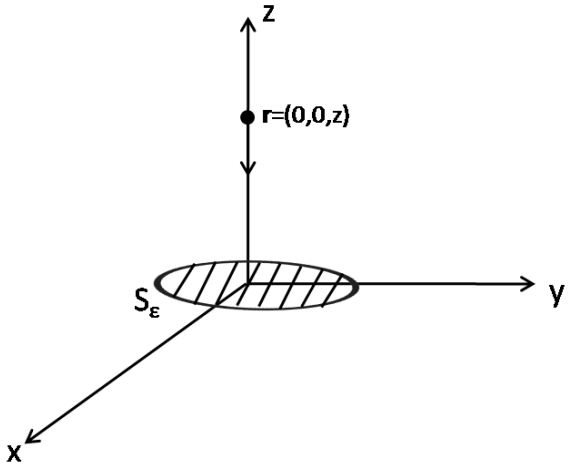

Figure 4.1: Observation point approaching to surface in the limit case.

So, the scattered magnetic field can be written as

$$\boldsymbol{H}^{sca}(\boldsymbol{r}) = \boldsymbol{H}^{sca}_{PV}(\boldsymbol{r}) + \boldsymbol{H}^{sca}_{lim}(\boldsymbol{r}). \tag{4.14}$$

Next, we approximate the Green's function in the case that the observation point gets close to the surface as

$$g(\boldsymbol{r}, \boldsymbol{r}') \approx \frac{1}{4\pi R}, \tag{4.15}$$

and we can calculate

$$\nabla'\Big(\frac{1}{R}\Big) = \frac{\boldsymbol{R}}{R^3}. \tag{4.16}$$

Substituting the approximated Green's function and its gradient in the limit value of scattered magnetic field, we obtain

$$\boldsymbol{H}^{sca}_{lim}(\boldsymbol{r}) = \lim_{S_\epsilon \to 0} \int_{S_\epsilon} d\boldsymbol{r}' \boldsymbol{J}(\boldsymbol{r}') \times \frac{\boldsymbol{R}}{4\pi R^3}, \tag{4.17}$$

where

$$\boldsymbol{R} = \boldsymbol{r} - \boldsymbol{r}' = \hat{\boldsymbol{z}}z - \hat{\boldsymbol{x}}x' - \hat{\boldsymbol{y}}y'. \tag{4.18}$$

Since the area of the surface is infinitesimal, we can assume that the current density is constant on this surface, i.e.,

$$\boldsymbol{J}_0 = \boldsymbol{J}(0,0,0) \tag{4.19}$$

Then, the current density in (4.17) can be taken out of the integral and the equation can be rewritten as

$$\begin{aligned}
\boldsymbol{H}_{lim}^{sca}(\boldsymbol{r}) &\approx \boldsymbol{J}_0 \times \lim_{S_\epsilon \to 0} \int_{S_\epsilon} d\boldsymbol{r}' \frac{\boldsymbol{R}}{4\pi R^3} \\
&= \frac{\boldsymbol{J}_0}{4\pi} \times \int_{S_\epsilon} d\boldsymbol{r}' \frac{\boldsymbol{R}}{R^3} \\
&= \frac{\boldsymbol{J}_0}{4\pi} \times \hat{\boldsymbol{z}} \int_0^{2\pi} d\phi' \int_0^{\epsilon} d\rho' \frac{\rho' z}{\left((\rho')^2 + z^2\right)^{3/2}} \\
&- \frac{\boldsymbol{J}_0}{4\pi} \times \hat{\boldsymbol{x}} \int_0^{2\pi} d\phi' \int_0^{\epsilon} d\rho' \frac{(\rho')^2 \cos(\phi')}{\left((\rho')^2 + z^2\right)^{3/2}} \\
&- \frac{\boldsymbol{J}_0}{4\pi} \times \hat{\boldsymbol{y}} \int_0^{2\pi} d\phi' \int_0^{\epsilon} d\rho' \frac{(\rho')^2 \sin(\phi')}{\left((\rho')^2 + z^2\right)^{3/2}} \\
&= -\frac{\boldsymbol{J}_0}{2} \times \hat{\boldsymbol{z}} \left[\frac{z}{[\epsilon^2 + z^2]^{1/2}} - \frac{z}{|z|} \right].
\end{aligned} \tag{4.20}$$

When we calculate the limit value while ϵ goes to zero, we obtain

$$\lim_{z \to 0} \boldsymbol{H}_{lim}^{sca}(\boldsymbol{r}_0) \approx \frac{\boldsymbol{J}_0}{2} \times \hat{\boldsymbol{z}}. \tag{4.21}$$

More generally, if the surface normal is in the direction of $\hat{\boldsymbol{n}}$

$$\lim_{\epsilon \to 0} \boldsymbol{H}_{lim}^{sca}(\boldsymbol{r}_0) \approx \frac{\boldsymbol{J}_0}{2} \times \hat{\boldsymbol{n}}. \tag{4.22}$$

So, the limit value of the scattered magnetic field is calculated to have a magnitude that is equal to half of the current density, and its direction is perpendicular to the plane of current flow, i.e.,

$$\boldsymbol{H}_{lim}^{sca}(\boldsymbol{r}_0) = \frac{\boldsymbol{J}_0}{2} \times \hat{\boldsymbol{n}}. \tag{4.23}$$

Then, by rewriting the MFIE with these observed results, we obtain

$$\hat{\boldsymbol{n}} \times \boldsymbol{H}^{inc}(\boldsymbol{r}) = \frac{\boldsymbol{J}(\boldsymbol{r})}{2} - \hat{\boldsymbol{n}} \times \frac{k^3}{4\pi} \int_{S_{PV}} d\boldsymbol{r}'(\boldsymbol{J}(\boldsymbol{r}') \times \boldsymbol{R})(G^R(R) - iG^I(R)). \quad (4.24)$$

By using (4.24) and the vector identity that

$$\boldsymbol{A} \cdot (\boldsymbol{B} \times \boldsymbol{C}) = \boldsymbol{C} \cdot (\boldsymbol{A} \times \boldsymbol{B}) = -\boldsymbol{C} \cdot (\boldsymbol{B} \times \boldsymbol{A}),$$

(4.12) can be rewritten as

$$\boldsymbol{a}_i \cdot (\hat{\boldsymbol{n}} \times \boldsymbol{H}^{inc}(\boldsymbol{r})) = \frac{\boldsymbol{a}_i \cdot \boldsymbol{J}(\boldsymbol{r})}{2} - (\hat{\boldsymbol{n}} \times \boldsymbol{a}_i) \cdot \frac{k^3}{4\pi} \int_{S_{PV}} d\boldsymbol{r}'(\boldsymbol{J}(\boldsymbol{r}') \times \boldsymbol{R})(G^R(R) - iG^I(R)). \quad (4.25)$$

4.1.2 Discretization

As for the EFIE, by assuming that the surface of the geometry is discretized into P curvilinear patches, and the integrations are approximated by introducing an N-point quadrature rule on each patch, (4.24) can be formulated by Nyström method as

$$\boldsymbol{a}_{im} \cdot (\hat{\boldsymbol{n}} \times \boldsymbol{H}^{inc}(\boldsymbol{r}_m)) = \frac{\boldsymbol{a}_{im} \cdot \boldsymbol{J}(\boldsymbol{r}_m)}{2} \delta_{mn} - \boldsymbol{a}_{im} \cdot \hat{\boldsymbol{n}} \times \frac{k^3}{4\pi} \sum_{p=1}^{P} \sum_{n=1}^{N} (\boldsymbol{J}(\boldsymbol{r}_n) \times \boldsymbol{R}_{mn})(G^R(R_{mn}) - iG^I(R_{mn}))\omega_n \sqrt{g_n}, \quad (4.26)$$

where $\boldsymbol{r}_m$ is source point, $\boldsymbol{r}_n$ is observation point, $\boldsymbol{a}_{im}$ are the unitary vectors at each source point, and $\sqrt{g_n}$ is the Jacobian defined as

$$\sqrt{g_n} = |\boldsymbol{a}_{1n} \times \boldsymbol{a}_{2n}| = \sqrt{g_{11}g_{22} - g_{12}^2}, \quad (4.27)$$

where

$$g_{ij} = \boldsymbol{a}_i \cdot \boldsymbol{a}_j. \quad (4.28)$$

Next, the surface current density is expanded in terms of two unitary vectors as follows

$$\boldsymbol{J}(\boldsymbol{r}_n) = \frac{\boldsymbol{a}_{1n} J_{1n} + \boldsymbol{a}_{2n} J_{2n}}{\sqrt{g_n}}. \quad (4.29)$$

Then, a linear system of equations can be formed by substituting (4.29) into (4.26) as

$$\begin{bmatrix} \boldsymbol{a}_{1m} \cdot (\hat{\boldsymbol{n}} \times \boldsymbol{H}^{inc}(\boldsymbol{r}_m)) \\ \boldsymbol{a}_{2m} \cdot (\hat{\boldsymbol{n}} \times \boldsymbol{H}^{inc}(\boldsymbol{r}_m)) \end{bmatrix} =$$

$$\begin{bmatrix} (\boldsymbol{a}_{1m} \cdot \boldsymbol{a}_{1m})/(2\sqrt{g_n}) & (\boldsymbol{a}_{1m} \cdot \boldsymbol{a}_{2m})/(2\sqrt{g_n}) \\ (\boldsymbol{a}_{2m} \cdot \boldsymbol{a}_{1m})/(2\sqrt{g_n}) & (\boldsymbol{a}_{2m} \cdot \boldsymbol{a}_{2m})/(2\sqrt{g_n}) \end{bmatrix} \cdot \begin{bmatrix} J_{1n} \\ J_{2n} \end{bmatrix} - \frac{k^3}{4\pi}$$

$$\begin{bmatrix} \boldsymbol{a}_{1m} \cdot \hat{\boldsymbol{n}} \times (\boldsymbol{a}_{1n} \times \boldsymbol{R}_{mn})(G^R - iG^I)\omega_n & \boldsymbol{a}_{1m} \cdot \hat{\boldsymbol{n}} \times (\boldsymbol{a}_{2n} \times \boldsymbol{R}_{mn})(G^R - iG^I)\omega_n \\ \boldsymbol{a}_{2m} \cdot \hat{\boldsymbol{n}} \times (\boldsymbol{a}_{1n} \times \boldsymbol{R}_{mn})(G^R - iG^I)\omega_n & \boldsymbol{a}_{2m} \cdot \hat{\boldsymbol{n}} \times (\boldsymbol{a}_{2n} \times \boldsymbol{R}_{mn})(G^R - iG^I)\omega_n \end{bmatrix}$$

$$\cdot \begin{bmatrix} J_{1n} \\ J_{2n} \end{bmatrix}, \qquad (4.30)$$

which is solved for the unknown current coefficients J_{1n} and J_{2n}. As shown in this equation, the kernel is composed of real and imaginary components. Hence, (4.30) can be rewritten as

$$\begin{bmatrix} \boldsymbol{a}_{1m} \cdot (\hat{\boldsymbol{n}} \times \boldsymbol{H}^{inc}(\boldsymbol{r}_m)) \\ \boldsymbol{a}_{2m} \cdot (\hat{\boldsymbol{n}} \times \boldsymbol{H}^{inc}(\boldsymbol{r}_m)) \end{bmatrix} = \begin{bmatrix} \frac{\boldsymbol{a}_{1m} \cdot \boldsymbol{a}_{1m}}{2\sqrt{g_n}} & \frac{\boldsymbol{a}_{1m} \cdot \boldsymbol{a}_{2m}}{2\sqrt{g_n}} \\ \frac{\boldsymbol{a}_{2m} \cdot \boldsymbol{a}_{1m}}{2\sqrt{g_n}} & \frac{\boldsymbol{a}_{2m} \cdot \boldsymbol{a}_{2m}}{2\sqrt{g_n}} \end{bmatrix} \cdot \begin{bmatrix} J_{1n} \\ J_{2n} \end{bmatrix}$$

$$- \begin{bmatrix} G_{mn_{11}} & G_{mn_{12}} \\ G_{mn_{21}} & G_{mn_{22}} \end{bmatrix} \cdot \begin{bmatrix} J_{1n} \\ J_{2n} \end{bmatrix}, \qquad (4.31)$$

where

$$G_{mn_{ij}} = G^R_{mn_{ij}} + G^I_{mn_{ij}}. \qquad (4.32)$$

4.2 Local Corrections

It is obvious from (4.30) that

$$G^R_{mn_{ij}} = -\frac{k^3}{4\pi} \boldsymbol{a}_{im} \cdot \hat{\boldsymbol{n}} \times (\boldsymbol{a}_{jn} \times \boldsymbol{R}_{mn}) G^R(R_{mn})\omega_n, \qquad (4.33)$$

and

$$G^I_{mn_{ij}} = i\frac{k^3}{4\pi} \boldsymbol{a}_{im} \cdot \hat{\boldsymbol{n}} \times (\boldsymbol{a}_{jn} \times \boldsymbol{R}_{mn}) G^I(R_{mn})\omega_n. \qquad (4.34)$$

We can immediately say that the contribution from $G^I_{mn_{ij}}$ is regular, while the contribution from $G^R_{mn_{ij}}$ is singular.

In the limit that the source and observation point gets very close to each other, components of the distance vector R_{mm} approaches to zero. Since G^I is bounded in this limit, the integral of this term will tend to 0. So, there is no need to locally correct the imaginary part of the kernel. On the other hand, the real part of the kernel goes to infinity since G^R is unbounded. Thus, $G^R_{mn_{ij}}$ must be locally corrected.

As for the EFIE, patch-based local corrections will be implemented for the MFIE. When the region of integration contains the observation point, the integrand will have a $1/R$ singularity. Thus, special techniques such as the Duffy transformation must be applied to accurately calculate the value of the integrals on self patches. However, as mentioned earlier in the EFIE section, for the patches that do not contain singularity but are in the near vicinity of the observation point, some numerical quadrature techniques must be applied adaptively to accurately calculate the integrals.

4.2.1 Local Corrections for Self Patch

Local correction coefficients for the MFIE are calculated using the following equation

$$\sum_{n=1}^{N} L_{mn_{ij}} f_j^k(\boldsymbol{r}_n)\omega_n = -\frac{k^3}{4\pi}\int_S d\boldsymbol{r}' \boldsymbol{a}_{im}\cdot\hat{\boldsymbol{n}}\times(\boldsymbol{J}(\boldsymbol{r}')\times\boldsymbol{R})G^R(R) + \frac{k^3}{4\pi}\sum_{n=1,n\neq m}^{N} \boldsymbol{a}_{im}\cdot\hat{\boldsymbol{n}}\times(\boldsymbol{J}(\boldsymbol{r}_n)\times\boldsymbol{R}_{mn})G^R(R_{mn})\omega_n\sqrt{g_n}, \quad (4.35)$$

where the first integral on the right-hand-side corresponds to the exact value of the integral, and the second one is the approximate result. The first term, which has a $1/R$ singularity, will be examined in details in Chapter 5. In the second term, the singular point is excluded from the calculation, so an error is

introduced intentionally. This residual error forms the right-hand-side of the following linear system

$$\begin{bmatrix} \omega_1 f_j^1(\boldsymbol{r}_1) & \omega_2 f_j^1(\boldsymbol{r}_2) & \dots & \omega_N f_j^1(\boldsymbol{r}_N) \\ \omega_1 f_j^2(\boldsymbol{r}_1) & \omega_2 f_j^2(\boldsymbol{r}_2) & \dots & \omega_N f_j^2(\boldsymbol{r}_N) \\ \vdots & & & \vdots \\ \omega_1 f_j^k(\boldsymbol{r}_1) & \omega_2 f_j^k(\boldsymbol{r}_2) & \dots & \omega_N f_j^k(\boldsymbol{r}_N) \end{bmatrix} \cdot \begin{bmatrix} L_{m1_{ij}} \\ L_{m2_{ij}} \\ \vdots \\ L_{mN_{ij}} \end{bmatrix} = \begin{bmatrix} E_m^1 \\ E_m^2 \\ \vdots \\ E_m^k \end{bmatrix}, \tag{4.36}$$

where the right-hand-side can also be written explicitly as

$$\begin{aligned} E_m^k = &- \frac{k^3}{4\pi} \boldsymbol{a}_{im} \cdot \hat{\boldsymbol{n}} \times \int_S d\boldsymbol{r}' (\boldsymbol{J}(\boldsymbol{r}') \times \boldsymbol{R}) G^R(R) \\ &+ \frac{k^3}{4\pi} \boldsymbol{a}_{im} \cdot \hat{\boldsymbol{n}} \times \sum_{n=1, n\neq m}^{N} (\boldsymbol{J}(\boldsymbol{r}_n) \times \boldsymbol{R}_{mn}) G^R(R_{mn}) \omega_n \sqrt{g_n}. \end{aligned} \tag{4.37}$$

By introducing a two-dimensional basis set over each patch, the current is expressed in terms of these known basis functions as follows

$$\boldsymbol{J}(\boldsymbol{r}_n) = \frac{\boldsymbol{a}_{1n} f_1^k(\boldsymbol{r}_n) + \boldsymbol{a}_{2n} f_2^k(\boldsymbol{r}_n)}{\sqrt{g_n}}, \tag{4.38}$$

where $f_j^k(\boldsymbol{r}_n)$ are chosen as the product of two Legendre polynomials that are defined in each parametric direction with the following orders

$$f_j^k(\boldsymbol{r}_n) = P_{k_1}(u_1) P_{k_2}(u_2), \qquad (k_1, k_2 : 0, 1, .., N-1) \tag{4.39}$$

Then, by substituting (4.38) into (4.37), we obtain

$$\begin{aligned} E_m^k = &- \frac{k^3}{4\pi} \boldsymbol{a}_{im} \cdot \hat{\boldsymbol{n}} \times \int_S d\boldsymbol{r}' (\boldsymbol{a}_j' \times \boldsymbol{R}) f_j^k(\boldsymbol{r}') G^R(R) \\ &+ \frac{k^3}{4\pi} \boldsymbol{a}_{im} \cdot \hat{\boldsymbol{n}} \times \sum_{n=1, n\neq m}^{N} (\boldsymbol{a}_j' \times \boldsymbol{R}) f_j^k(\boldsymbol{r}') G^R(R) \omega_n. \end{aligned} \tag{4.40}$$

4.2.2 Local Corrections for Near Patches

As for the EFIE, when the observation point is on a different patch than the integration region, the singularity vanishes. But, the problem still occurs when the source point is on a patch that is in the near vicinity of the observation point. In this case, the integral is calculated using adaptive quadrature rules (see Chapter 5).

4.3 Excitation

For the scattering problems in this thesis, plane-wave excitation is used. In the plane-wave excitation, the external source is a plane wave that have a certain propagation direction. The plane-wave incident electric field can be written as

$$\boldsymbol{E}^{inc}(\boldsymbol{r}) = \boldsymbol{E}_o \exp\left(i\boldsymbol{k}\cdot\boldsymbol{r}\right) \tag{4.41}$$

where $\boldsymbol{E}_o$ is a complex vector that satisfies

$$\boldsymbol{E}_o \cdot \boldsymbol{k} = 0. \tag{4.42}$$

For $\hat{\theta}$ polarization

$$\boldsymbol{E}_o = \hat{\boldsymbol{x}}\cos\theta\cos\phi + \hat{\boldsymbol{y}}\cos\theta\sin\phi - \hat{\boldsymbol{z}}\sin\theta, \tag{4.43}$$

and for $\hat{\phi}$ polarization

$$\boldsymbol{E}_o = -\hat{\boldsymbol{x}}\sin\phi + \hat{\boldsymbol{y}}\cos\phi. \tag{4.44}$$

Also,

$$\boldsymbol{k} = \hat{\boldsymbol{x}}k_x + \hat{\boldsymbol{y}}k_y + \hat{\boldsymbol{z}}k_z \tag{4.45}$$

where

$$\begin{aligned} k_x &= -k_o\sin\theta\cos\phi \\ k_y &= -k_o\sin\theta\sin\phi \\ k_z &= -k_o\cos\theta. \end{aligned} \tag{4.46}$$

Then, the incident magnetic field can be written as

$$\boldsymbol{H}^{inc}(\boldsymbol{r}) = \frac{1}{\eta}\hat{\boldsymbol{k}} \times \boldsymbol{E}_o \exp\left(i\boldsymbol{k}\cdot\boldsymbol{r}\right). \tag{4.47}$$

4.4 RCS Calculations

In this section, the calculation of the radar cross section (RCS) with the LCN method is introduced briefly. The electric field in the far-zone ($r \gg \lambda$) can be expressed as

$$\boldsymbol{E}(\boldsymbol{r}) = ik\eta\Big[\hat{\boldsymbol{\theta}}\boldsymbol{F}_\theta(\theta,\phi) + \hat{\boldsymbol{\phi}}\boldsymbol{F}_\phi(\theta,\phi)\Big]g(r), \tag{4.48}$$

where $\boldsymbol{F}(\theta,\phi)$ is the vector current moment defined as

$$\boldsymbol{F}(\theta,\phi) = \int_{S'} d\boldsymbol{r}'\boldsymbol{J}(\boldsymbol{r}')\exp(-ik\hat{r}\cdot r'), \tag{4.49}$$

and

$$g(r) = \frac{\exp(ikr)}{r}. \tag{4.50}$$

Since the current is defined on points in the LCN method, vector current moments are calculated directly without integrating on the surface S. Then, they are summed to find the vector current moment of the overall current distribution.

The RCS is calculated using vector current moments as follows

$$\begin{aligned} RCS(\theta,\phi) &= 4\pi r^2|\boldsymbol{E}(\boldsymbol{r})|^2 \\ &= \frac{k^2\eta^2}{4\pi}\Big|\hat{\boldsymbol{\theta}}\boldsymbol{F}_\theta(\theta,\phi) + \hat{\boldsymbol{\phi}}\boldsymbol{F}_\phi(\theta,\phi)\Big|^2. \end{aligned} \tag{4.51}$$

Chapter 5

Numerical Evaluation of the Integrals

When patch-based local correction is implemented, the region over which local correction coefficients are computed always includes the patch that contains the observation point. And it extends out to include other patches until the integral is calculated with the desired accuracy by using the underlying quadrature rule. So the problem of local corrections is composed of local corrections on several patches. In principle, the regular part of the kernel does not need to be locally corrected. But, if the integrand cannot be calculated efficiently with the quadrature rule, then it is better to treat them as if they were singular and compute the local corrections. Since such a local correction does not contain a direct singularity, it will be sufficient to calculate them using an adaptive quadrature rule. In this section, the methods for adaptive calculation of this kind of integrals will be introduced. On the other hand, if the observation point coincides with one of the quadrature points on the locally corrected patch, some special techniques should be used to handle this problem. One way to solve the singularity problem is to divide the integration region into triangular domains and use Duffy transform on these regions [16].

5.1 The Duffy Transform

Assume that K is a kernel with $1/R$ singularity. Then, consider the following integration over a quadrilateral patch:

$$\begin{aligned}\phi(\boldsymbol{r}_m) &= \int_S d\boldsymbol{r}' K(\boldsymbol{r}_m, \boldsymbol{r}') J(\boldsymbol{r}') \\ &= \int_{u_2=0}^{1} \int_{u_1=0}^{1} du_1 du_2 \sqrt{g} K(\boldsymbol{r}_m, \boldsymbol{r}') J(\boldsymbol{r}') \end{aligned} \tag{5.1}$$

where $\boldsymbol{r}_m$ is observation point on the surface, and when source and observation points coincide, the singularity occurs.

As shown in Figure 5.1, first, the quadrilateral patch is divided into four triangles that share a common vertex at the singular point. Note that, (u_1, u_2) are coordinates of the parametric space, where $u_1, u_2 \in (0, 1)$. The integration over the quadratic patch can be written as the summation of the integrations over each triangle. To calculate the integrations over the triangles, each of the triangles is considered to be degenerate quads, which means one vertex of the triangle is elapsed to one side of the quadratic patch. The degenerate quad is then mapped into the unitary space with parameters (α, β). As indicated in Figure 5.1(c), the vertices $\boldsymbol{r}_1$ and $\boldsymbol{r}_2$ are mapped to $(0, 1)$ and $(1, 0)$, respectively, whereas the singular vertex, $\boldsymbol{r}_s$, is mapped to edge $\alpha = 0$. Thus, the integral can be written as

$$\phi(\boldsymbol{r}_m) = \sum_{n=1}^{N_{tri}} 2A_n \int_{\beta=0}^{1} \int_{\alpha=0}^{1} d\alpha d\beta \alpha \sqrt{g(u_1, u_2)} K(\boldsymbol{r}_m, \boldsymbol{r}'(u_1, u_2)) J(\boldsymbol{r}'(u_1, u_2)), \tag{5.2}$$

where N_{tri} is the number of triangles, and A_n is the area of the n-th triangle.

Also, note that

$$\begin{aligned} 2A_n &= |(\boldsymbol{r}_1 - \boldsymbol{r}_s) \times (\boldsymbol{r}_2 - \boldsymbol{r}_s)| \\ &= \sqrt{||(\boldsymbol{r}_1 - \boldsymbol{r}_s)||^2 ||(\boldsymbol{r}_2 - \boldsymbol{r}_s)||^2 - ((\boldsymbol{r}_1 - \boldsymbol{r}_s) \cdot (\boldsymbol{r}_2 - \boldsymbol{r}_s))^2}. \end{aligned} \tag{5.3}$$

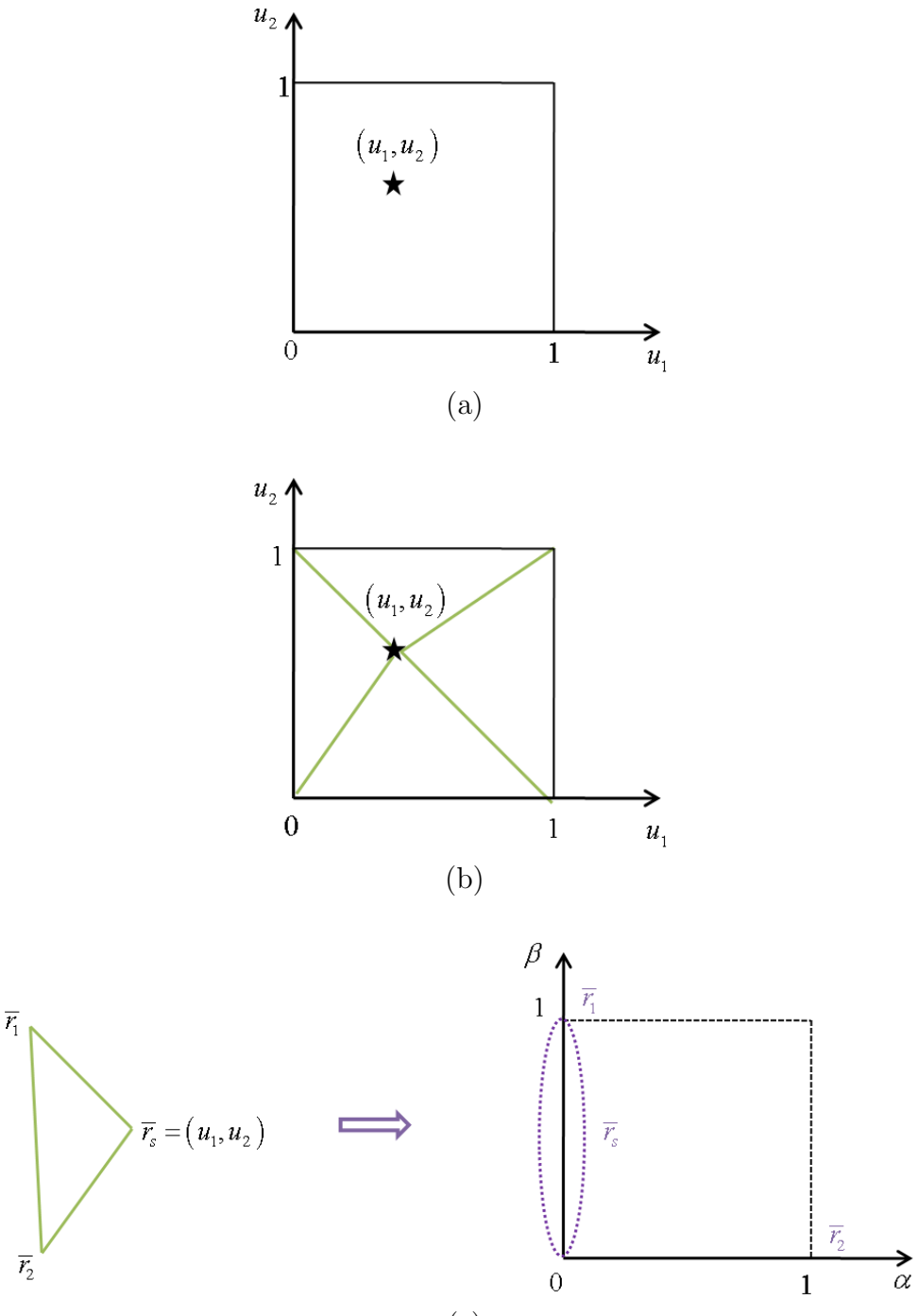

Figure 5.1: (a) Singular point on the patch in the parametric space, (b) triangulated patch with common vertex at the singular point, and (c) mapping the Duffy-triangle into the unitary space.

The unitary coordinates are related to the parametric coordinates as follows

$$\boldsymbol{r} = (u_1, u_2) = (1-\alpha)\boldsymbol{r}_s + \alpha(1-\beta)\boldsymbol{r}_1 + \alpha\beta\boldsymbol{r}_2. \tag{5.4}$$

So, to evaluate the integral, first, (u_1, u_2) are calculated from parametric coordinates. Then, $\boldsymbol{r}_s(u_1, u_2)$, the unitary vectors, and the Jacobian are computed using the surface formulation. This process effectively removes the $1/R$ simgularity. The integrands that contain higher order singularities need to be modified before Duffy transform can be used. If it cannot be reduced to $1/R$, then other techniques must be preferred.

5.1.1 The Duffy Transform for EFIE

The integrand that makes the EFIE singular with an order of $1/R$ is as follows

$$ik\eta \int_S d\boldsymbol{r}'(\boldsymbol{a}_{im} \cdot \boldsymbol{a}_j{}')g^R(\boldsymbol{r}_m, \boldsymbol{r}')\frac{f_j^k(\boldsymbol{r}')}{\sqrt{g'}} = ik^2\eta \int_S d\boldsymbol{r}'(\boldsymbol{a}_{im} \cdot \boldsymbol{a}_j{}')\frac{\cos kR}{4\pi(kR)}\frac{f_j^k(\boldsymbol{r}')}{\sqrt{g'}}. \tag{5.5}$$

By using (5.2), the integrand is evaluated on the triangles and the results are superposed to form the overall integral as follows

$$\begin{aligned} &ik^2\eta \int_S d\boldsymbol{r}'(\boldsymbol{a}_{im} \cdot \boldsymbol{a}_j{}')\frac{\cos kR}{4\pi(kR)}\frac{f_j^k(\boldsymbol{r}')}{\sqrt{g'}} \\ &\quad = \frac{ik^2\eta}{4\pi}\sum_{n=1}^{4} 2A_n \int_{\beta=0}^{1}\int_{\alpha=0}^{1} d\alpha d\beta\alpha(\boldsymbol{a}_{im} \cdot \boldsymbol{a}_j{}')\frac{\cos kR}{(kR)}\frac{f_j^k(\boldsymbol{r}')}{\sqrt{g'}}. \end{aligned} \tag{5.6}$$

The integrand in (5.6) then can be evaluated effectively by using a high-order adaptive quadrature rule on the unitary space.

5.1.2 The Duffy Transform for MFIE

The singular term in the MFIE can be written as

$$\begin{aligned} &-\frac{k^3}{4\pi}\int_S d\boldsymbol{r}'\boldsymbol{a}_{im} \cdot \hat{\boldsymbol{n}} \times (\boldsymbol{J}(\boldsymbol{r}_n) \times \boldsymbol{R})G^R(R) \\ &\quad = -\frac{k^3}{4\pi}\boldsymbol{a}_{im} \cdot \hat{\boldsymbol{n}} \times \int_S d\boldsymbol{r}'(\boldsymbol{a}_j \times \boldsymbol{R})f_j^k(\boldsymbol{r}')/\sqrt{g'}G^R(R). \end{aligned} \tag{5.7}$$

Similar to the EFIE, we can evaluate this integral using the Duffy transform after dividing the surface into four triangles that have a common vertex at the singular point. By using (5.2), (5.7) can be rewritten as

$$-\frac{k^3}{4\pi}\boldsymbol{a}_{im}\cdot\hat{\boldsymbol{n}}\times\int_S d\boldsymbol{r}'(\boldsymbol{a}_j\times\boldsymbol{R})f_j^k(\boldsymbol{r}')/\sqrt{g'}G^R(R)$$
$$=\frac{-k^3}{4\pi}\sum_{n=1}^{4}2A_n\boldsymbol{a}_{im}\cdot\hat{\boldsymbol{n}}\times\int_{\beta=0}^{1}\int_{\alpha=0}^{1}d\alpha d\beta\alpha(\boldsymbol{a}_j\times\boldsymbol{R})f_j^k(\boldsymbol{r}')/\sqrt{g'}G^R(R), \tag{5.8}$$

where

$$G^R(R)=\frac{\cos(kR)+kR\sin(kR)}{R^3}. \tag{5.9}$$

To this end, since the order of singularity is $1/R$, we can evaluate (5.8) efficiently, by using an adaptive Gauss-Legendre quadrature rule if the surface is smooth, or we can calculate it by using an adaptive Gauss-Jacobi quadrature rule if the surface has geometric singularities, such as sharp edges.

5.1.3 Contribution to the Duffy Transform

The Duffy transform is a widely used and efficient method to handle $1/R$ singularity. As we mentioned earlier in this chapter, for the singular integrals, first the quadrilateral region is divided into triangular domains, then the Duffy transform is employed to calculate the integrals on each of these regions. When the observation point is far from the edges and the corners, the Duffy transform works perfectly. On the other hand, if the observation point is close to a corner or an edge, the triangles that share this point at the common vertex do not have similar shapes any more. Indeed, some of them have very bad aspect ratios that the result of the integrand converges to the desired tolerance by passing through several levels of the adaptive integration routine, i.e. by using too many points in adaptive calculations. Hence, the computational resources increase in this case. For example, consider the MFIE integrand. All the integration points at each level and their values are plotted as a cloud of points on the unitary space as

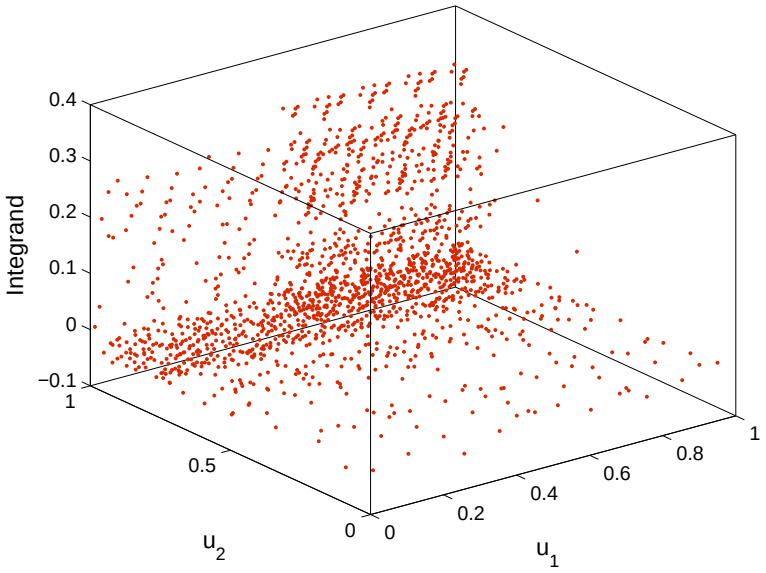

(a)

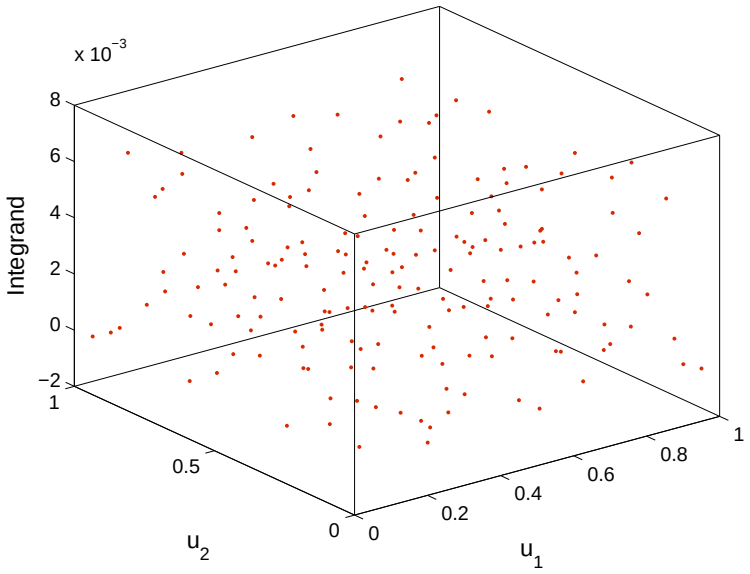

(b)

Figure 5.2: The integrand plotted on the first triangle by using: (a) classical Duffy and (b) modified Duffy.

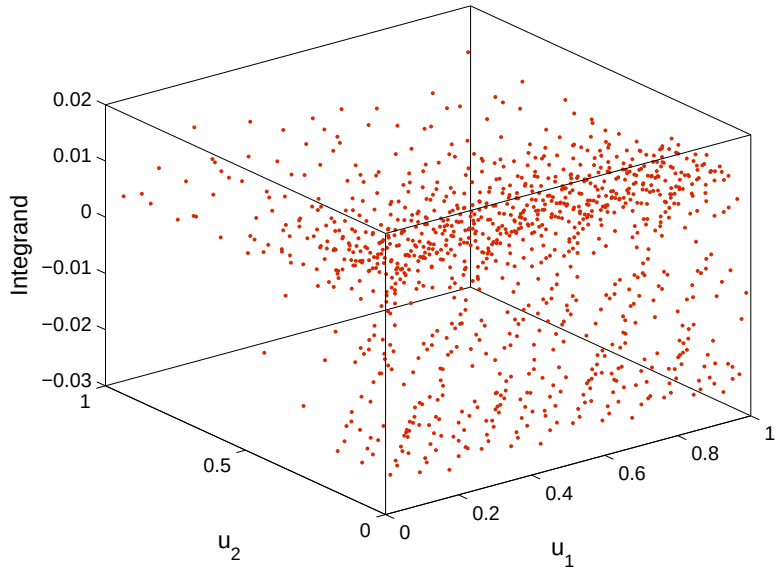

(a)

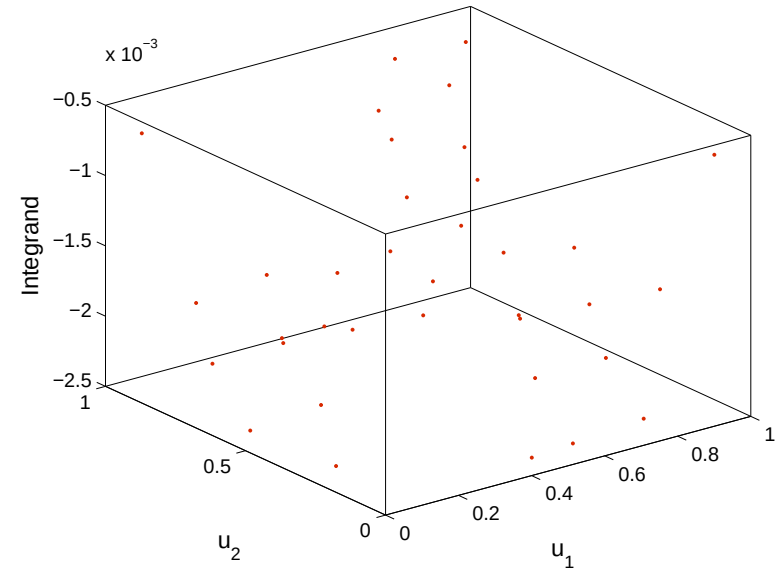

(b)

Figure 5.3: The integrand plotted on the second triangle by using: (a) classical Duffy and (b) modified Duffy.

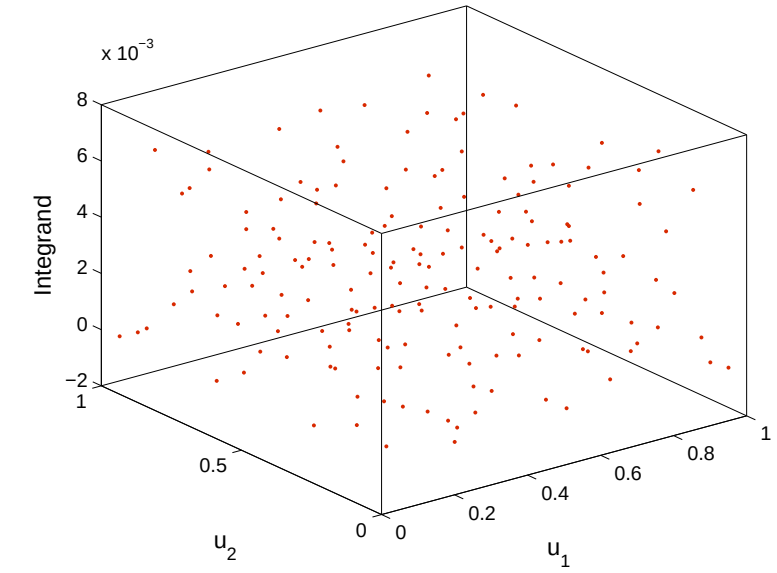

(a)

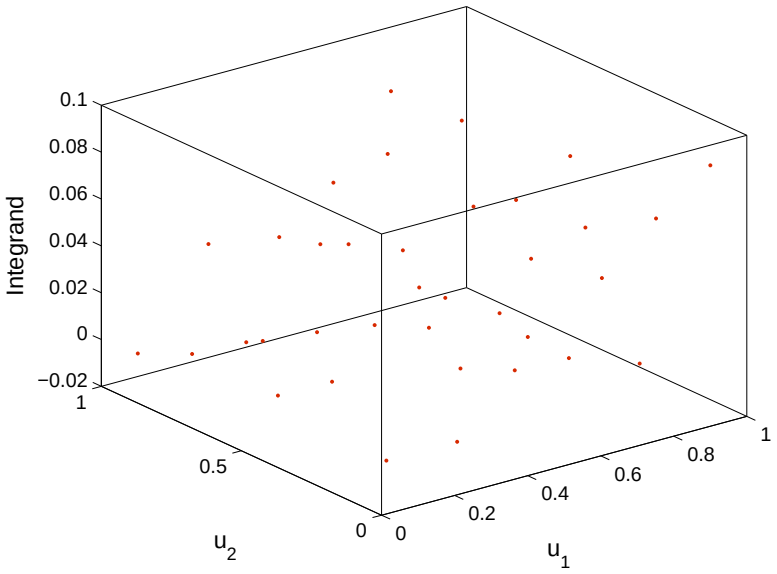

(b)

Figure 5.4: The integrand plotted on the third triangle by using: (a) classical Duffy and (b) modified Duffy.

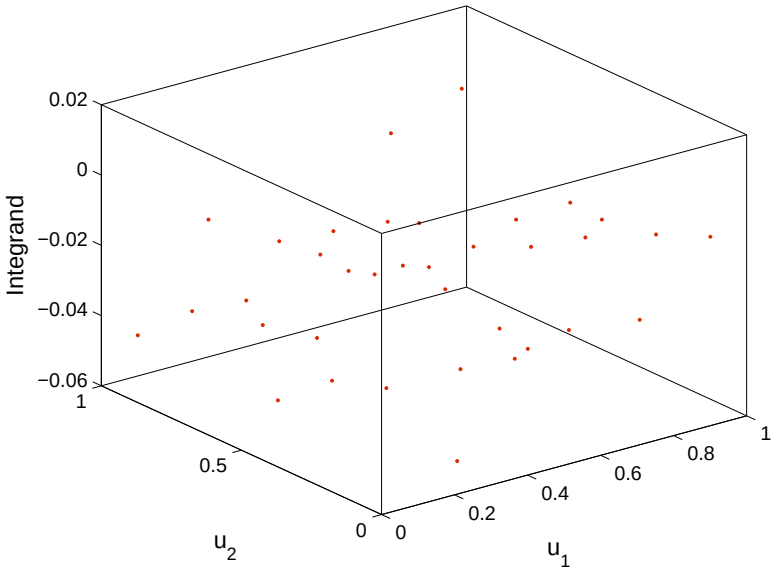

(a)

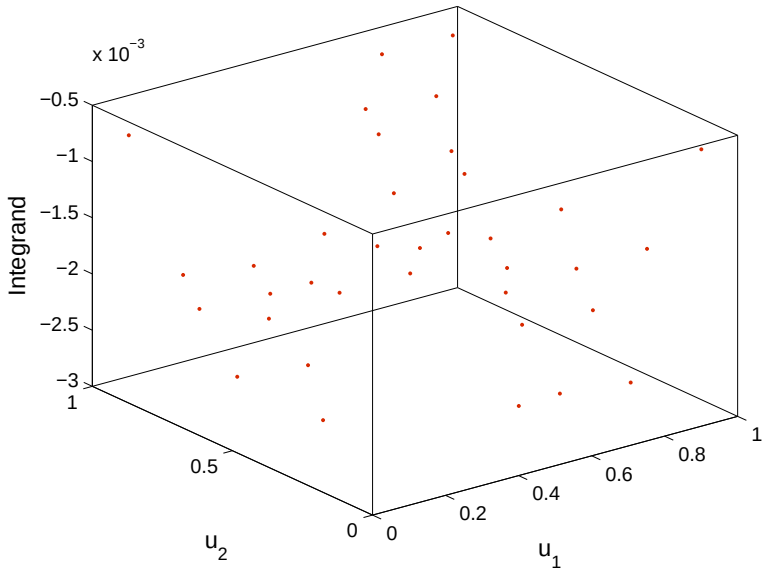

(b)

Figure 5.5: The integrand plotted on the fourth triangle by using: (a) classical Duffy and (b) modified Duffy.

Table 5.1: Total CPU-time (sec) required to calculate Duffy integrals for a sphere at all observation points by using the MFIE formulation.

Tolerance	Classical Duffy	Modified Duffy
10^{-2}	45.7	24.5
10^{-3}	89.9	44.6
10^{-4}	164.8	80.5
10^{-5}	333.3	150.1

shown in Figures 5.2(a)–5.5(a). These results belong to a sphere that is composed of 24 curvilinear patches. In the figures, the observation point is very close to one corner in the parametric space. The kernel of the plotted integrand is exactly as given in (5.8). We have presented the simplest case by choosing the order of the Legendre polynomials as first order. Despite this, on the first and second triangles, too many integration points are used to reach the correct result.

For the classical Duffy transform, the division of the integration region into triangular domains is shown in Figure 5.6(a). Our contribution to the Duffy transform is dividing the region into triangular subdomains in a different way which is shown in Figure 5.6(b). The aim of such division is to correct the aspect ratio of the triangles. Then, the integrand converges to the desired accuracy faster by using less number of integration points. The shape of the integrand and number of integration points for both methods are presented in Figures 5.2–5.5. From these results modified method seems more efficient. But as we know, the integration regions are not the same anymore. In the modified method, the triangles are smaller, and in addition to that, there are now extra two or three regions that we have to calculate the integrals on. So, we cannot restrict the efficiency only with the number of integration points seen in the figures. Also, the required total time for the calculation of Duffy integrations on all of the triangular and rectangular regions must be analyzed. When we look at the total required times shown at Table 5.1 for both of the methods, we can explicitly say that the new method is much more faster than the classical method.

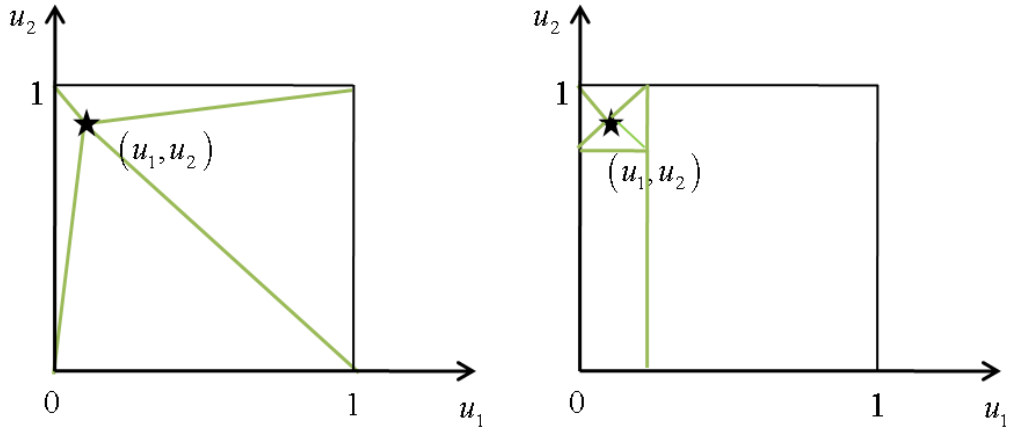

Figure 5.6: Division of the quadrilateral region into triangular domains for the (a) classical Duffy and (b) modified Duffy.

Table 5.2: Total CPU-time (sec) required to calculate Duffy integrals for a $1\lambda \times 1\lambda$ patch at all observation points by using the EFIE formulation.

Quadrature Rule	Classical Duffy	Modified Duffy
8×9	22	8.6
9×10	45	15
11×11	101	35
12×12	153	60

We can also check the accuracy of the results obtained from these methods. When the RCS values are calculated using both of these methods, 3 or 4 digits of matching is obtained between them. So, the advantage of the new method is the solution time is substantially decreased while the accuracy remains approximately the same.

We observed similar results for the EFIE. This time, an open patch geometry is investigated. Since we do not have an analytical solution for this geometry, the MLFMA solution with a mesh size of $\lambda/100$ is accepted as the reference value. Then, both the accuracy and the required time for all of the Duffy integrations are obtained for both of the methods. The beauty of the modified Duffy method

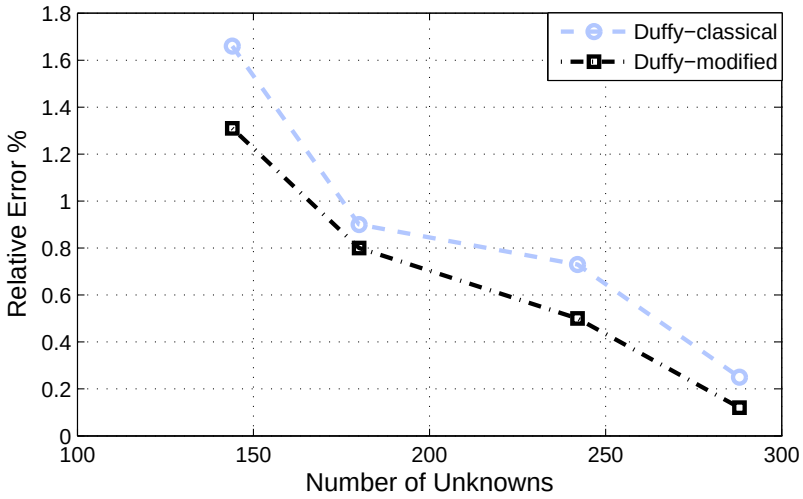

Figure 5.7: Relative error of classical and modified Duffy transforms for a $1\lambda \times 1\lambda$ patch using the EFIE formulation.

is, as for the MFIE, the required CPU-time is decreased substantially. The CPU-time results for the EFIE solution are presented in Table 5.2. Also, the relative errors with respect to the reference value are plotted in Figure 5.7.

5.2 Adaptive Integration

The numerical integrations for both of the EFIE and the MFIE are calculated using Gauss-Legendre quadrature rules. Using a static quadrature rule in the implementation may result inaccurate integrations or inefficient calculations. For example, if the number of points are less than required, the final value of the integral probably does not converge to the exact value within a desired tolerance. On the other hand, many integration points can be used even if a few of them could already satisfy the convergence criteria. In addition, in some cases it would be better to take more samples where the function oscillates rapidly, while taking less points for smooth regions. Hence, in order to control the integration error efficiently, an adaptive algorithm can be used.

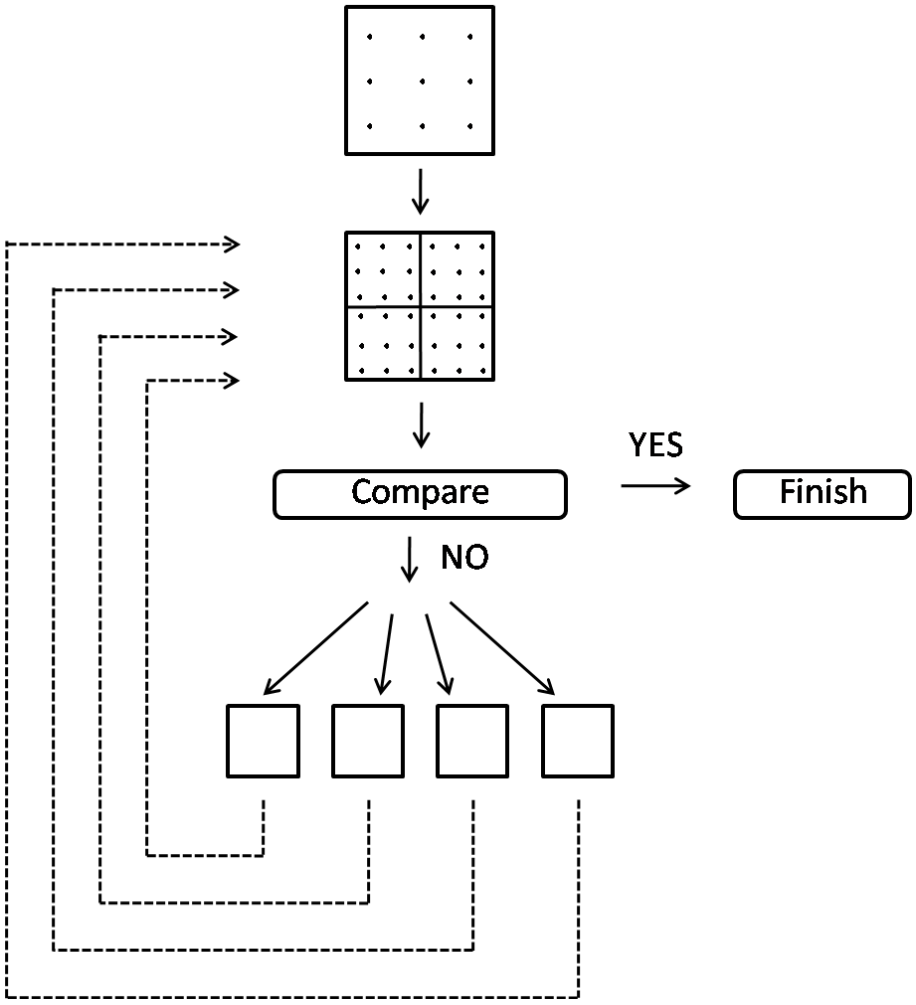

Figure 5.8: Adaptive integration method 1.

5.2.1 Method 1

One of the adaptive integration methods used to calculate the integrals on the parametric space is as shown in Figure 5.8.

- Two one-dimensional Gauss-Legendre quadrature rules are combined to form a 3×3 two-dimensional quadrature rule on the parametric space.
- The quadrilateral is divided into four pieces and on each of them 3×3 Gauss-Legendre quadrature rule is defined.

- A comparison is performed on the integration value of one-piece quad versus summation of integration values on four-pieces. The error is defined as

$$E = \frac{|I_4 - I_1|}{|I_4|}. \tag{5.10}$$

  If the error is less then the desired error threshold, then the integration is assumed to converge. Hence, I_4 becomes the result of the integration. If the error is larger than threshold, next step comes.

- If convergence of the integration is not satidfied, each of the four sub-quads are considered as separate regions, on which the integrations are expected to converge individually. Then, going back to the first step, we already have the value of I_1, the process continues by dividing each of the quads into sub-quads as in the second step.

- This process continues until each of the subdomains converge to the desired accuracy. Whenever convergence is reached in a subdomain, the corresponding branch of the algorithm stops, but the algorithm continues until all of the subdomains reach convergence.

This algorithm works efficiently when the integration region is a square or close to a square. However, when the integration region is a rectangle with a large aspect ratio, subdivision into four domains at each step becomes inefficient. The second adaptive integration method can be applied to such regions.

5.2.2 Method 2

The second algorithm is more suitable for rectangular domains. In this method, domains are divided into two pieces instead of four at each level. Before the division starts, the algorithm finds the longer edge and places subdomains on this edge to avoid destroying the aspect ratio of the rectangular domains. The algorithm is as shown in Figure 5.9.

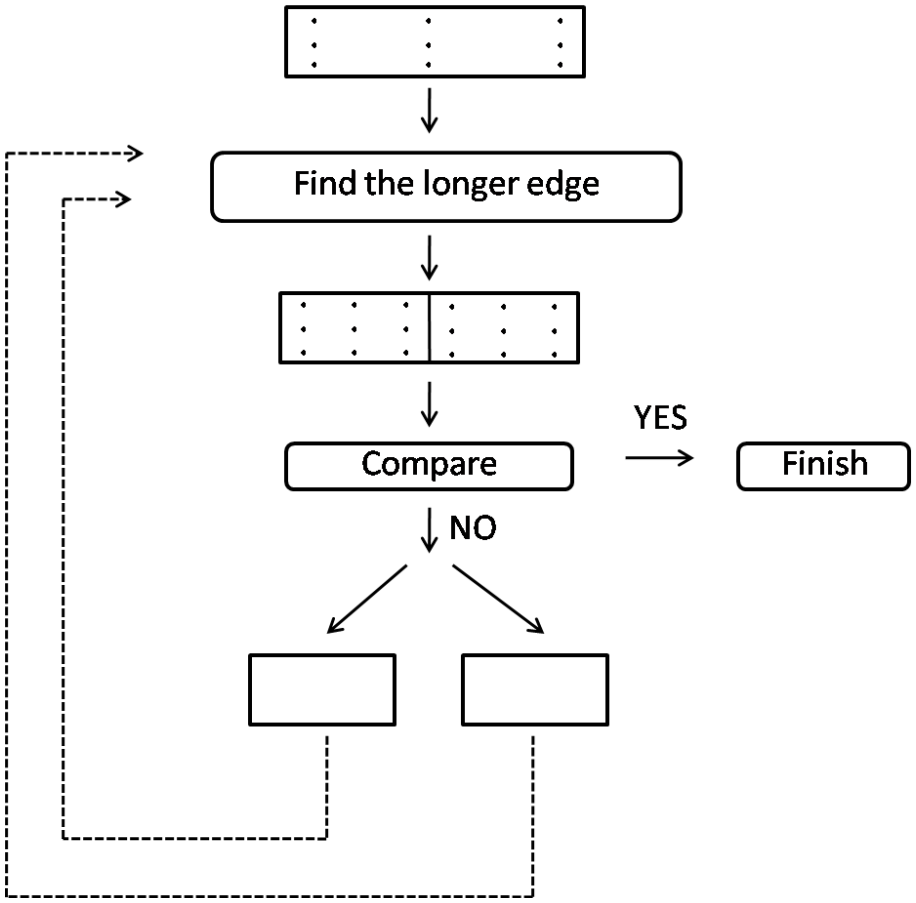

Figure 5.9: Adaptive integration method 2.

- The algorithm starts with defining a 3×3 quadrature rule on the rectangular domain.
- Before dividing into two pieces, the algorithm determines the longer edge. Then, the rectangle is divided into two pieces and on each of them 3×3 Gauss-Legendre quadrature rule is defined.
- A comparison is performed on the integration value of one-piece quad versus summation of integration values on two-pieces. The error is as defined in (5.10). And the remaining steps are same as the first algorithm.

In both steps, the process continues until convergence in every region is satisfied. This may lead to unnecessary usage of time. Convergence on some regions may

not be so important since the result of this region may be negligible compared to other regions. For this reason, in both of the algorithms, the error criteria in subdomains is redetermined according to its contribution to the overall integral. For example, at one level of any of the algorithms, integral results on each of the four regions are calculated separately. Then, maximum of these values are found. It is assumed that, this value dominates the overall result. So the error criteria remains same for the calculation of this term in the next step. On the other hand, the negligibility of the remaining parts are determined according to their values, which means if the contribution of one quad to the overall integral is small, then the error criteria will be more flexible for the convergence of this term in the next steps.

Chapter 6

Mixed-Order Basis Functions

In the LCN method, Legendre polynomials are used in conjunction with the Gauss-Legendre quadrature rule for local corrections. These basis functions represent the current completely to a specified order. It was shown by Çalışkan and Peterson [17] that current results, especially for cross-polarization components, can be incorrect if the polynomial complete basis functions are employed by the EFIE. The reason for this is that the polynomial complete basis functions do not correctly represent the continuity of charge relation, since the charge distribution is implicitly modeled by the divergence of the basis functions used to model the current distribution [18]. That is, the static term in the EFIE operator requires the divergence of the current density, hence both the current density and the charge density must be represented by the basis functions. Thus, when using a polynomial complete basis set, the charge continuity can be violated.

Interestingly, when the Jacobi polynomial basis functions are used, this problem does not occur for a simple patch problem. Because, this basis is inherently a mixed-order basis that can accurately represent both the current and charge densities [19]. On the other hand, this set can only be applied to a limited class of problems.

6.1 Discretization with the Mixed-Order Basis Functions

For the local correction of a patch, the current density is expanded in terms of the basis functions over the corresponding patch. When the polynomial complete basis functions are used as the basis set, the current is expressed as [20]

$$\boldsymbol{J}_i^{pc}(u_1,u_2) = \frac{\boldsymbol{a}_i P_j(u_1) P_k(u_2)}{\sqrt{g}} \qquad (i=1,2; j,k=0...p). \tag{6.1}$$

where (u_1, u_2) are the local curvilinear coordinates, $\boldsymbol{a}_i$ are the local unitary vectors, $\sqrt{g}$ is the Jacobian, and $P_j(u_i)$ are j-th order Legendre polynomials in the u_i direction. On the other hand, when mixed order basis functions are used, the current density is expressed as

$$\boldsymbol{J}_1^{mo}(u_1,u_2) = \frac{\boldsymbol{a}_1 P_j(u_1) P_k(u_2)}{\sqrt{g}} \qquad (j=0...p; k=0...p-1) \tag{6.2}$$

$$\boldsymbol{J}_2^{mo}(u_1,u_2) = \frac{\boldsymbol{a}_2 P_j(u_1) P_k(u_2)}{\sqrt{g}} \qquad (j=0...p-1; k=0...p) \tag{6.3}$$

where $\boldsymbol{J}_1^{mo}$ is polynomial complete to order $p+1$ along u_1 and p along u_2, while $\boldsymbol{J}_2^{mo}$ is polynomial complete to order p along u_1 and $p+1$ along u_2. Also, we can express the charge density using mixed-order basis function set as follows

$$\begin{aligned}\rho &= \frac{1}{i\omega}\nabla\cdot\boldsymbol{J} \\ &= \frac{1}{i\omega\sqrt{g}}\left[\frac{\partial P_j(u_1)}{\partial u_1}P_k(u_2) + P_j(u_1)\frac{\partial P_k(u_2)}{\partial u_2}\right].\end{aligned} \tag{6.4}$$

To sum up, if the polynomial complete basis functions are used to expand the current density, then this set does not represent the charge density with a complete polynomial expansion. In this case, the surface charge densities will be mixed-order, while the mixed-order representation of the current density leads to a surface charge density that is polynomial complete [19].

6.2 Validation

As an example to the usage of mixed-order basis functions, consider a $1\lambda \times 1\lambda$ plate in free space, illuminated by a normally-incident plane wave.

Figure 6.1 presents a solution of the EFIE using polynomial complete basis functions and a Gauss-Legendre quadrature rule with an order of 10×10. The y-component of the current density exhibits irregular fluctuations especially at the corners. By implementing the EFIE with mixed-order basis function set of order 10×11, it is observed that the cross-polarization current density results are more accurate as shown in Figure 6.2.

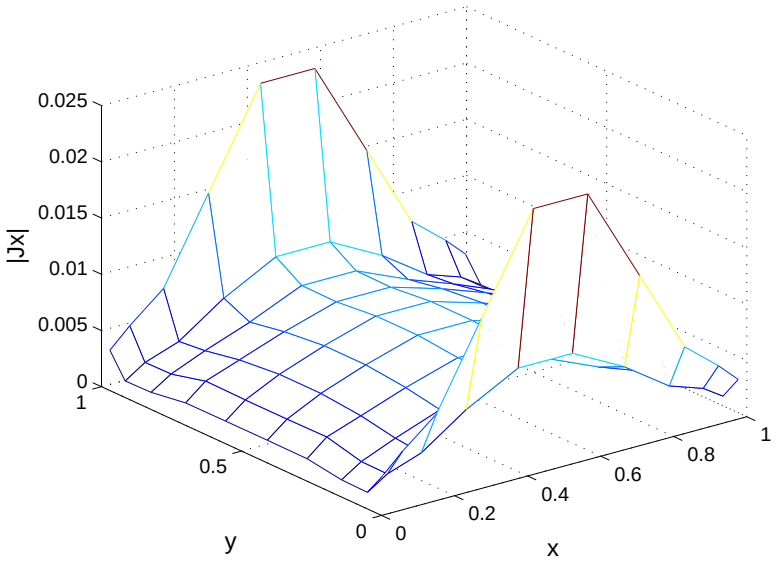

(a)

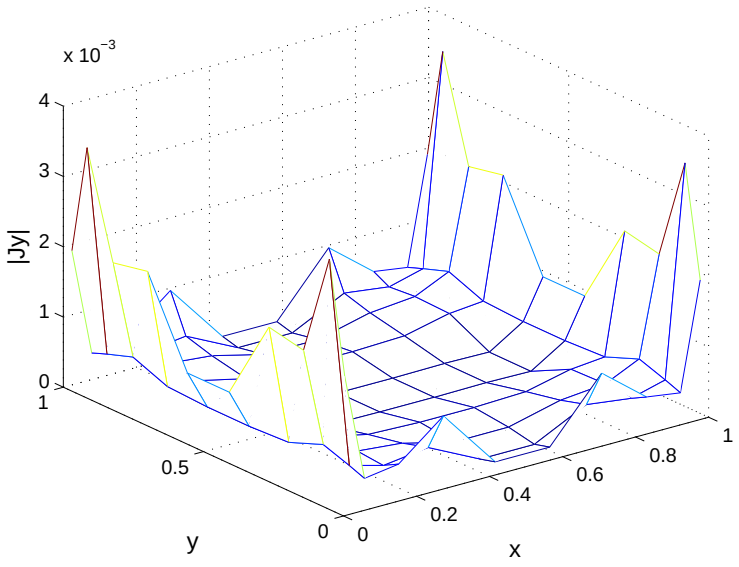

(b)

Figure 6.1: (a) x component and (b) y component of the surface current density on a $1\lambda \times 1\lambda$ plate by using a 10×10 quadrature rule.

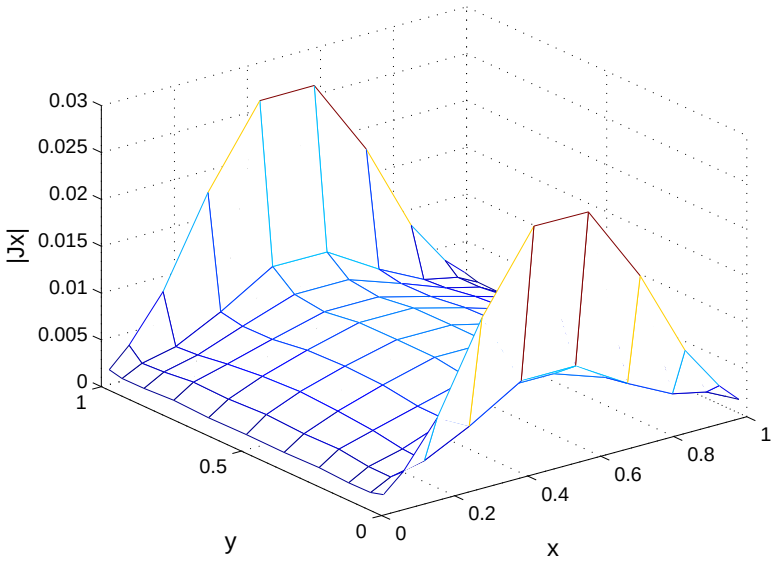

(a)

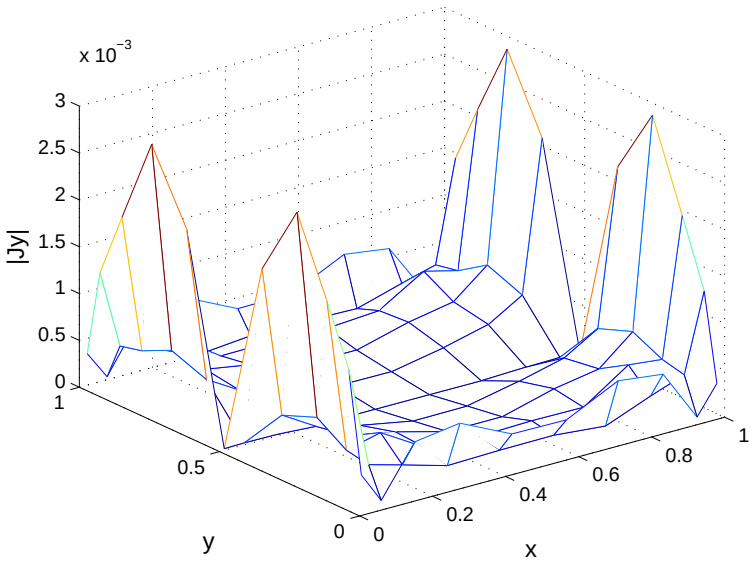

(b)

Figure 6.2: (a) x component and (b) y component of the surface current density on a $1\lambda \times 1\lambda$ plate by using a 10×11 quadrature rule.

Chapter 7

The Locally Corrected Nyström Method Implementations

In this chapter, we present various examples for the scattering problems that are solved with the LCN method. More specifically, we present current density results for some patch geometries that are solved using the EFIE. Also, the current density on all of the six faces of a cube are presented. The cube solutions are obtained both with MoM and the LCN method, and the MFIE formulation is implemented. Next, we present RCS results for several geometries, such as patch, cube, sphere, ellipsoid, NASA almond, and ogive. We compare the results of the LCN method with MLFMA solver of Bilkent University Computational Electromagnetics Research Center (BiLCEM), whose accuracy and efficiency is presented with several applications in several resources. Finally, we investigate the efficiency and accuracy of the LCN method with results of some geometries.

7.1 Current Results for Some Geometries

In the preceding chapter, we have shown current density results for a $1\lambda \times 1\lambda$ patch. Here, we will present the solutions for the same patch, but the patch is composed of four pieces this time. The surfaces are illuminated by a normally-incident plane wave. The x and y components of the surface current density are shown in Figure 7.1. As shown in the figure, the continuity of the current density is satisfied for both of the components. We also present the current density of some geometries that are composed of two patches while the distance between these patches changes. When the patches are far from each other, the interactions between them are negligibly small. On the other hand, when they get close to each other, to satisfy the continuity of current relation, the interactions become stronger. These results are shown in Figures 7.2–7.6.

Next, current densities on each face of a PEC cube with edge length of 1λ are presented for the LCN method in Figures 7.7 and 7.8. This simple geometry is of interest since it has geometric singularities at the edges and corners. Each face of the cube is finely discretized with four cells. Fifth-order quadrature rule and basis functions are employed on each cell. Results are obtained with the MFIE solution. The cube is illuminated from the front face, i.e., the direction of the plane wave is in the $-\hat{x}$ direction. For comparison, the MoM solutions are also given in Figures 7.9 and 7.10. It can be seen from these figures that the LCN and MoM results are in a strong agreement with each other.

7.2 RCS Results for Several Geometries

In this section, we present RCS results of several geometries. Some of these open geometries, which are solved using the EFIE formulation, are shown in Figure 7.11. RCS values of these geometries are presented in Figures 7.12–7.17

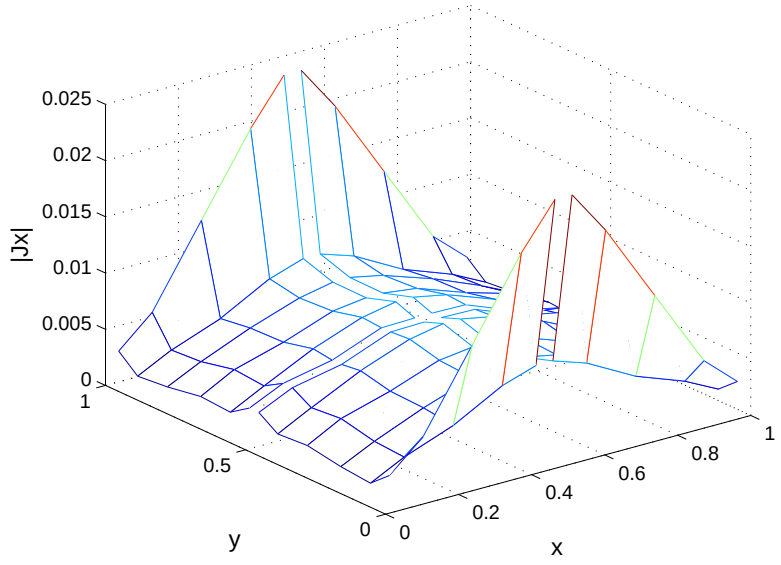

(a)

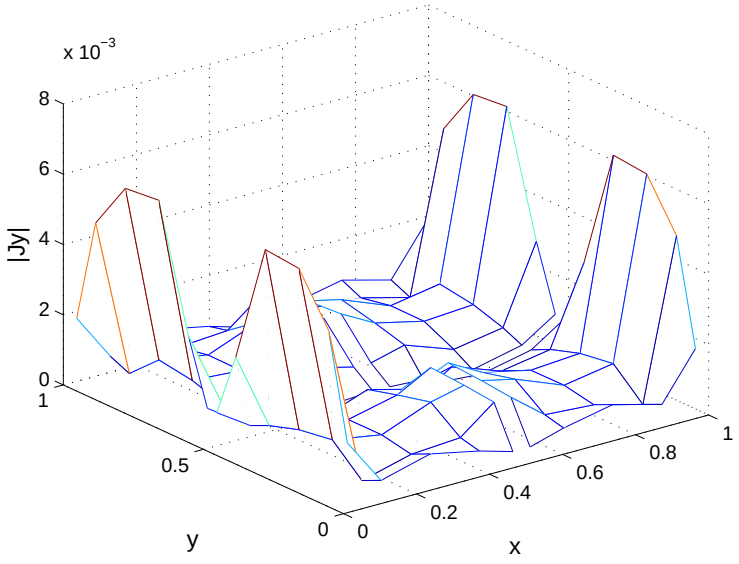

(b)

Figure 7.1: (a) x component and (b) y component of the surface current density on a $1\lambda \times 1\lambda$ plate, which is divided into four pieces, by using a 5×6 quadrature rule on each of the patches.

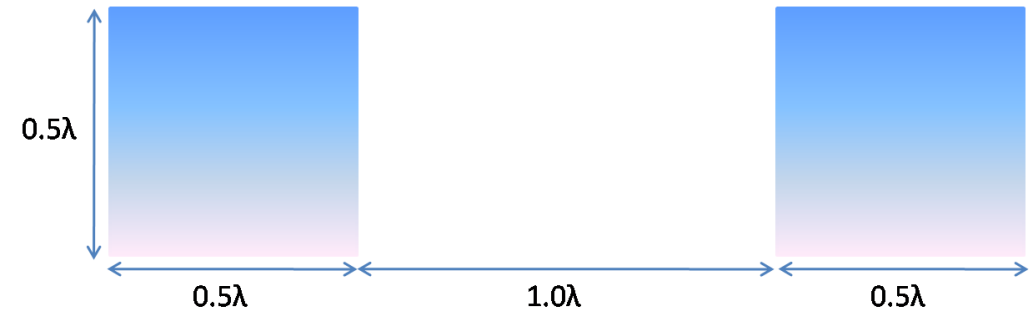

(a)

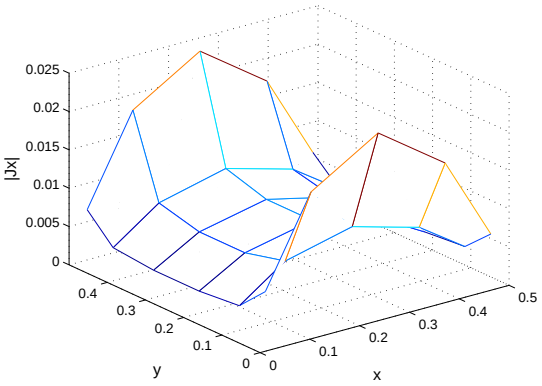

(b)

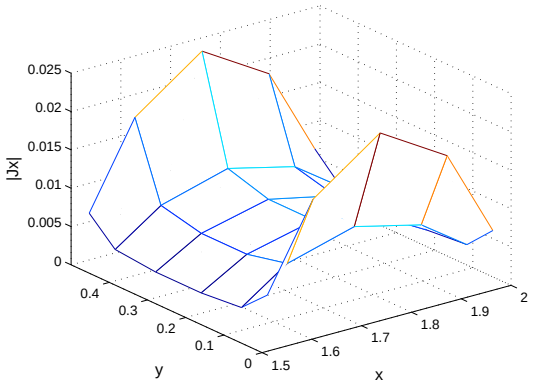

(c)

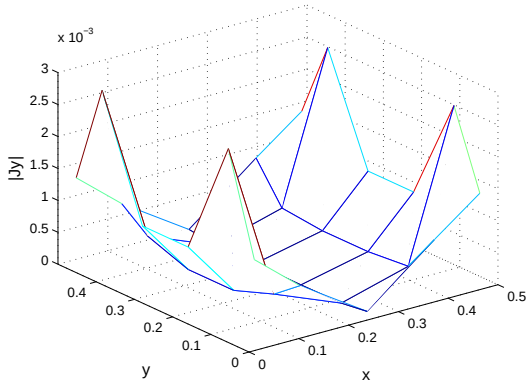

(d)

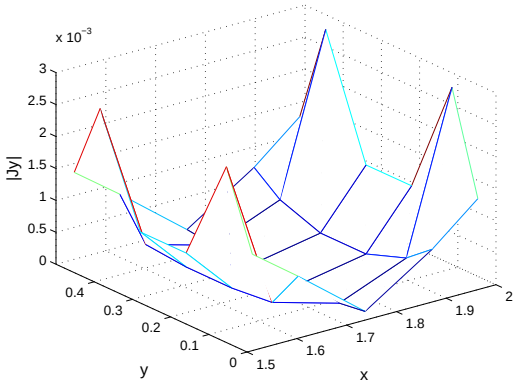

(e)

Figure 7.2: Current density results obtained with the LCN-EFIE formulation, (a) the geometry to be solved, (b) x component on the first patch, (c) x component on the second patch, (d) y component on the first patch, and (e) y component on the second patch.

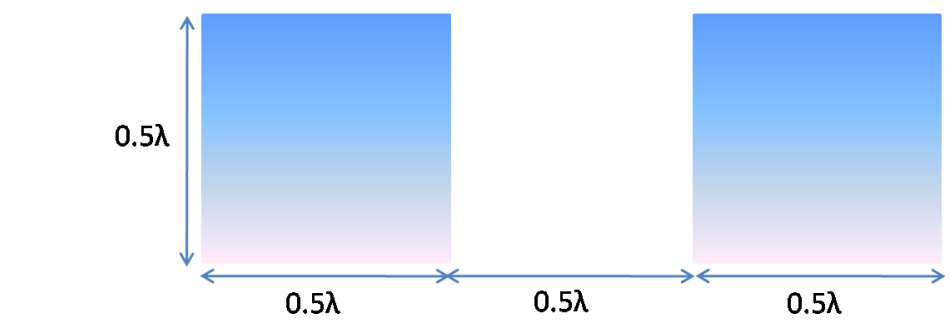

(a)

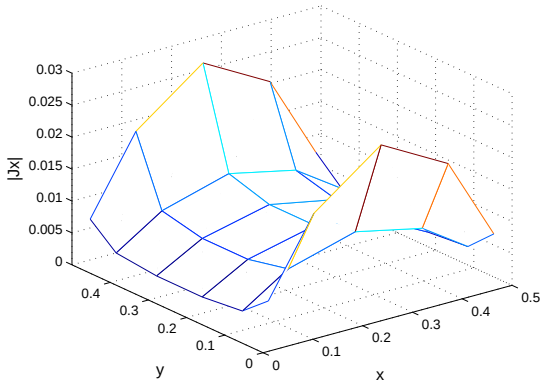

(b)

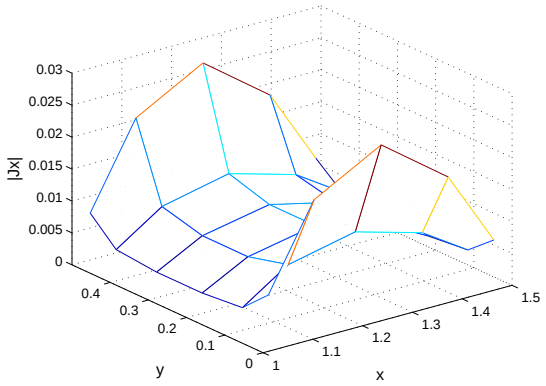

(c)

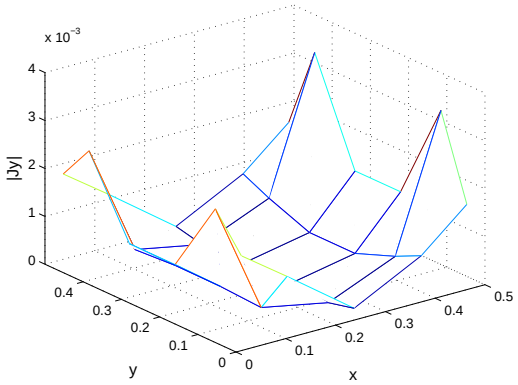

(d)

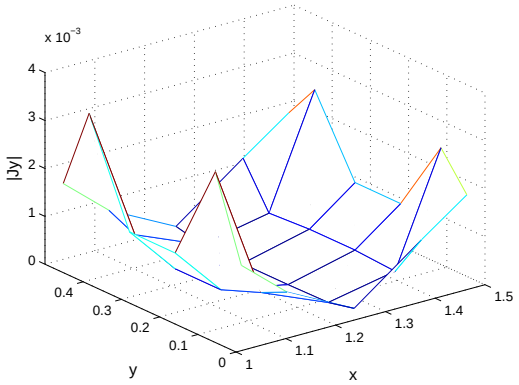

(e)

Figure 7.3: Current density results obtained with the LCN-EFIE formulation, (a) the geometry to be solved, (b) x component on the first patch, (c) x component on the second patch, (d) y component on the first patch, and (e) y component on the second patch.

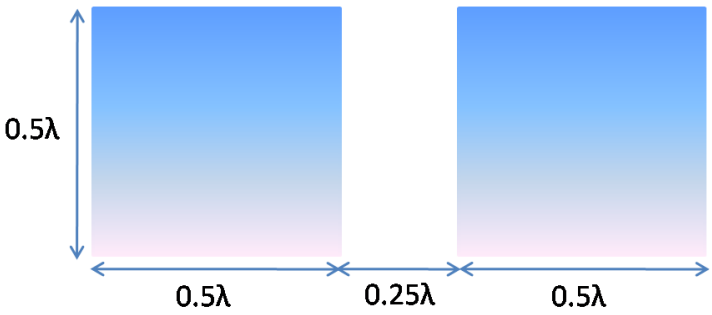

(a)

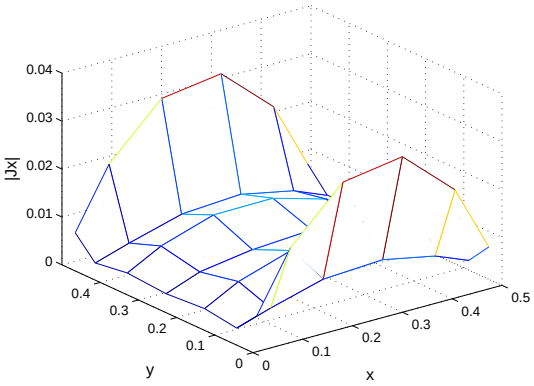

(b)

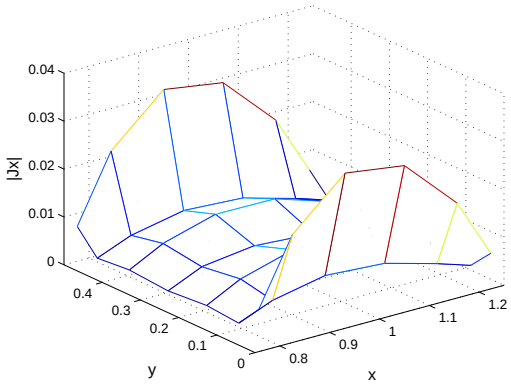

(c)

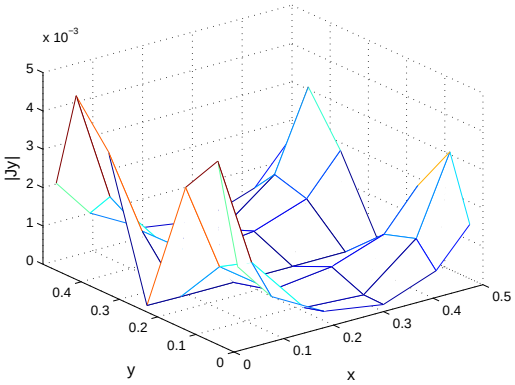

(d)

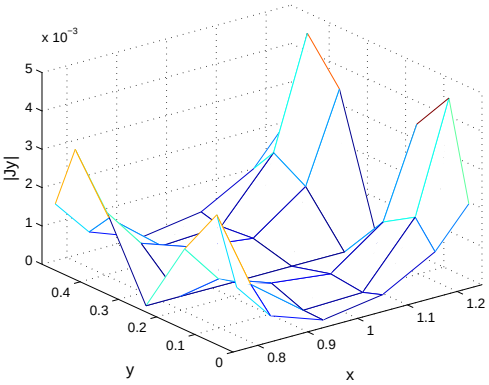

(e)

Figure 7.4: Current density results obtained with the LCN-EFIE formulation, (a) the geometry to be solved, (b) x component on the first patch, (c) x component on the second patch, (d) y component on the first patch, and (e) y component on the second patch.

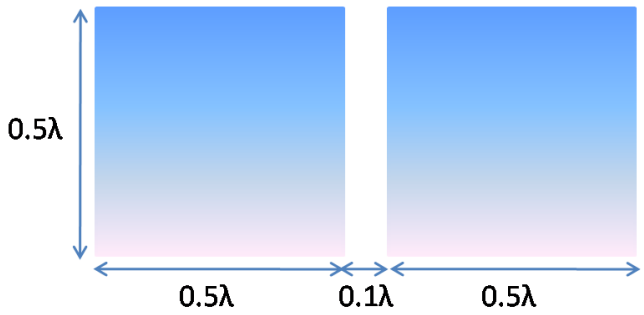

(a)

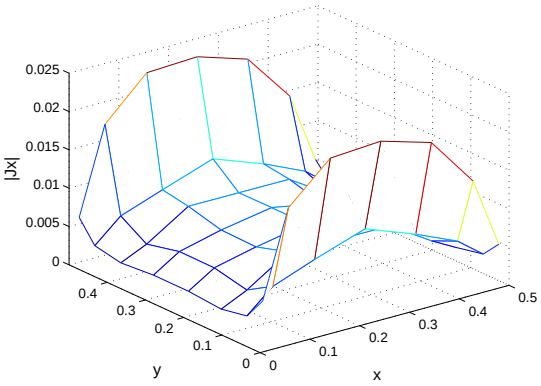

(b)

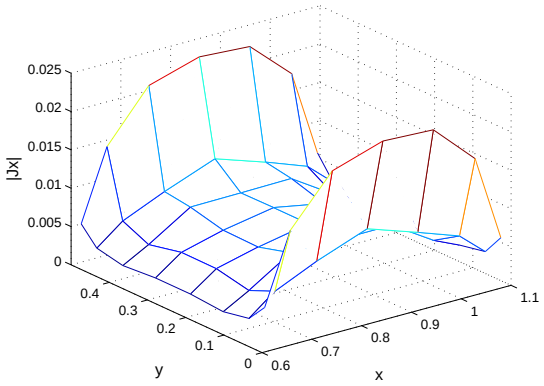

(c)

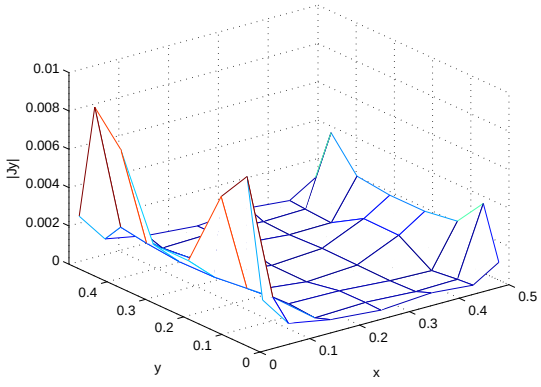

(d)

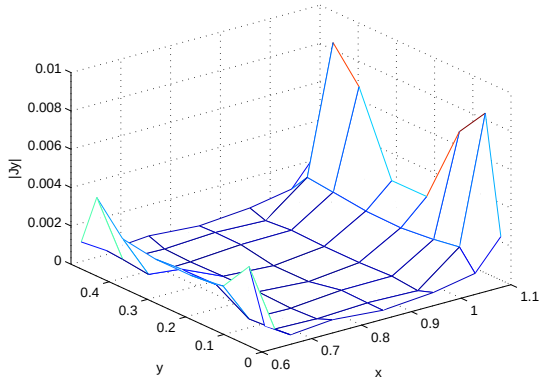

(e)

Figure 7.5: Current density results obtained with the LCN-EFIE formulation, (a) the geometry to be solved, (b) x component on the first patch, (c) x component on the second patch, (d) y component on the first patch, and (e) y component on the second patch.

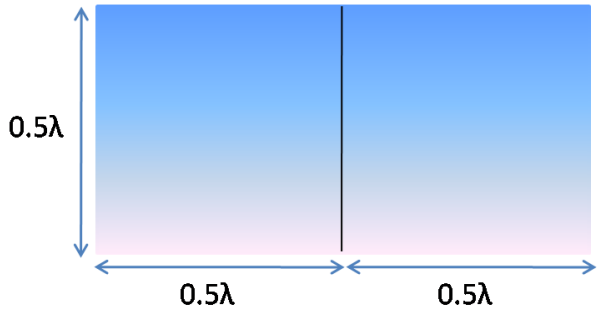

(a)

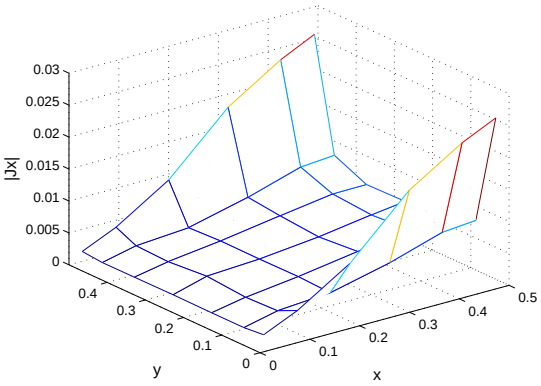

(b)

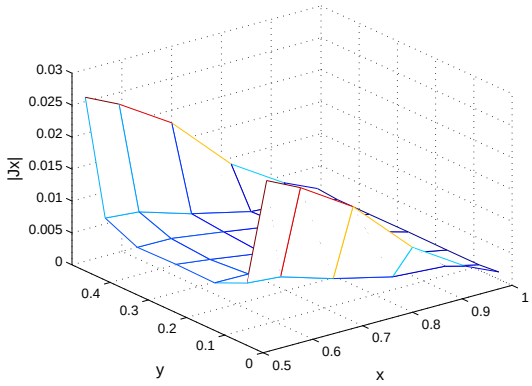

(c)

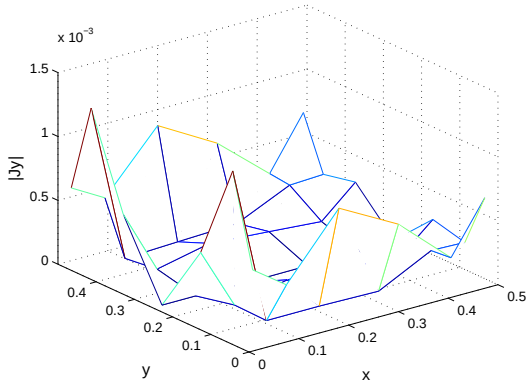

(d)

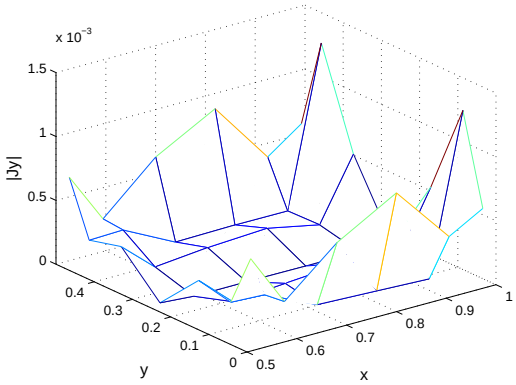

(e)

Figure 7.6: Current density results obtained with the LCN-EFIE formulation, (a) the geometry to be solved, (b) x component on the first patch, (c) x component on the second patch, (d) y component on the first patch, and (e) y component on the second patch.

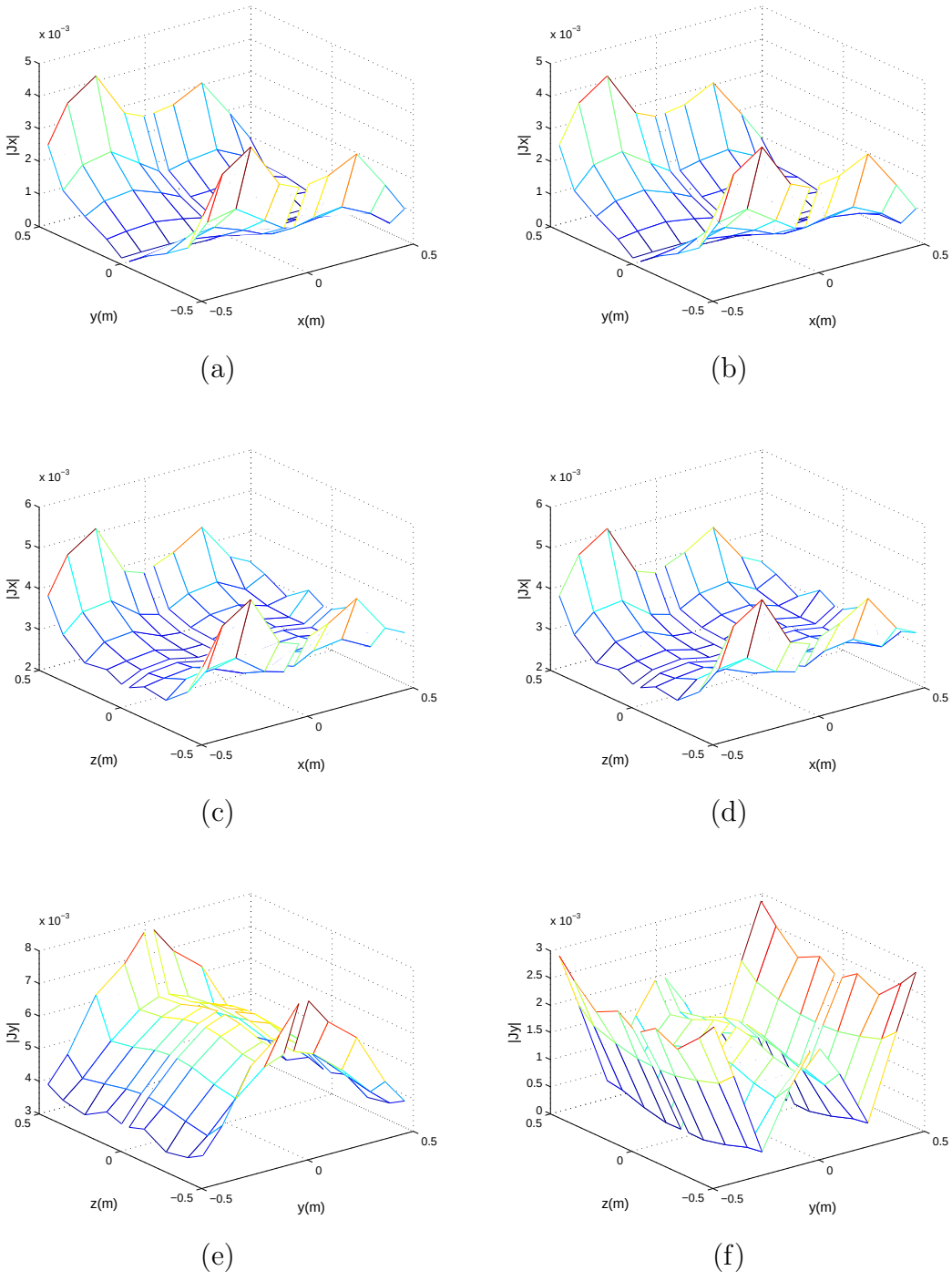

Figure 7.7: The current density results for a 1λ cube, obtained with the LCN-MFIE, x component on the: (a) top face, (b) bottom face, (c) right face, (d) left face, y component on the: (e) front face, and (f) back face.

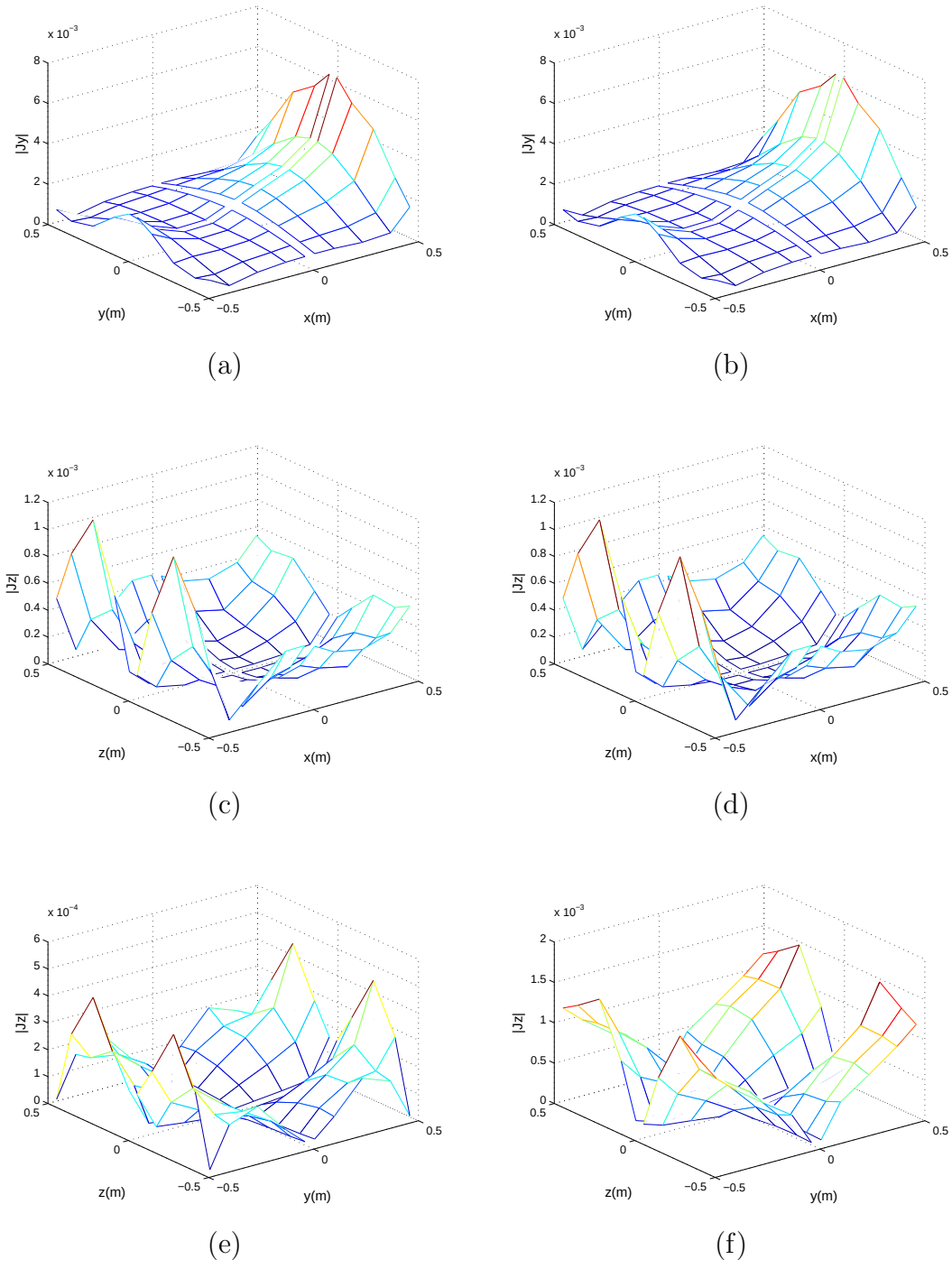

Figure 7.8: The current density results for a 1λ cube, obtained with the LCN-MFIE, y component on the: (a) top face, (b) bottom face, z component on the: (c) right face, (d) left face, (e) front face, and (f) back face.

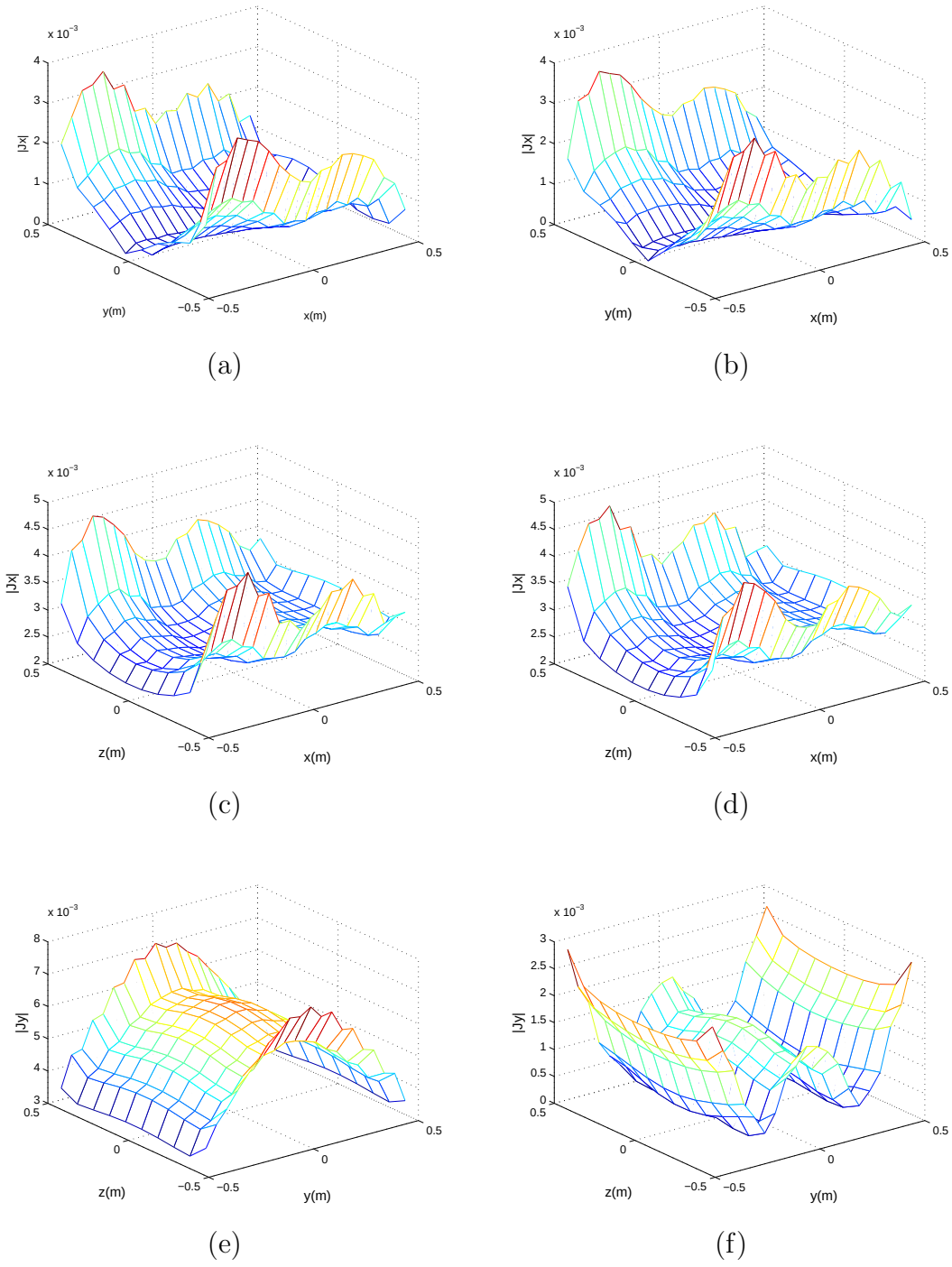

Figure 7.9: The current density results for a 1λ cube, obtained with the MoM-MFIE, x component on the: (a) top face, (b) bottom face, (c) right face, (d) left face, y component on the: (e) front face, and (f) back face.

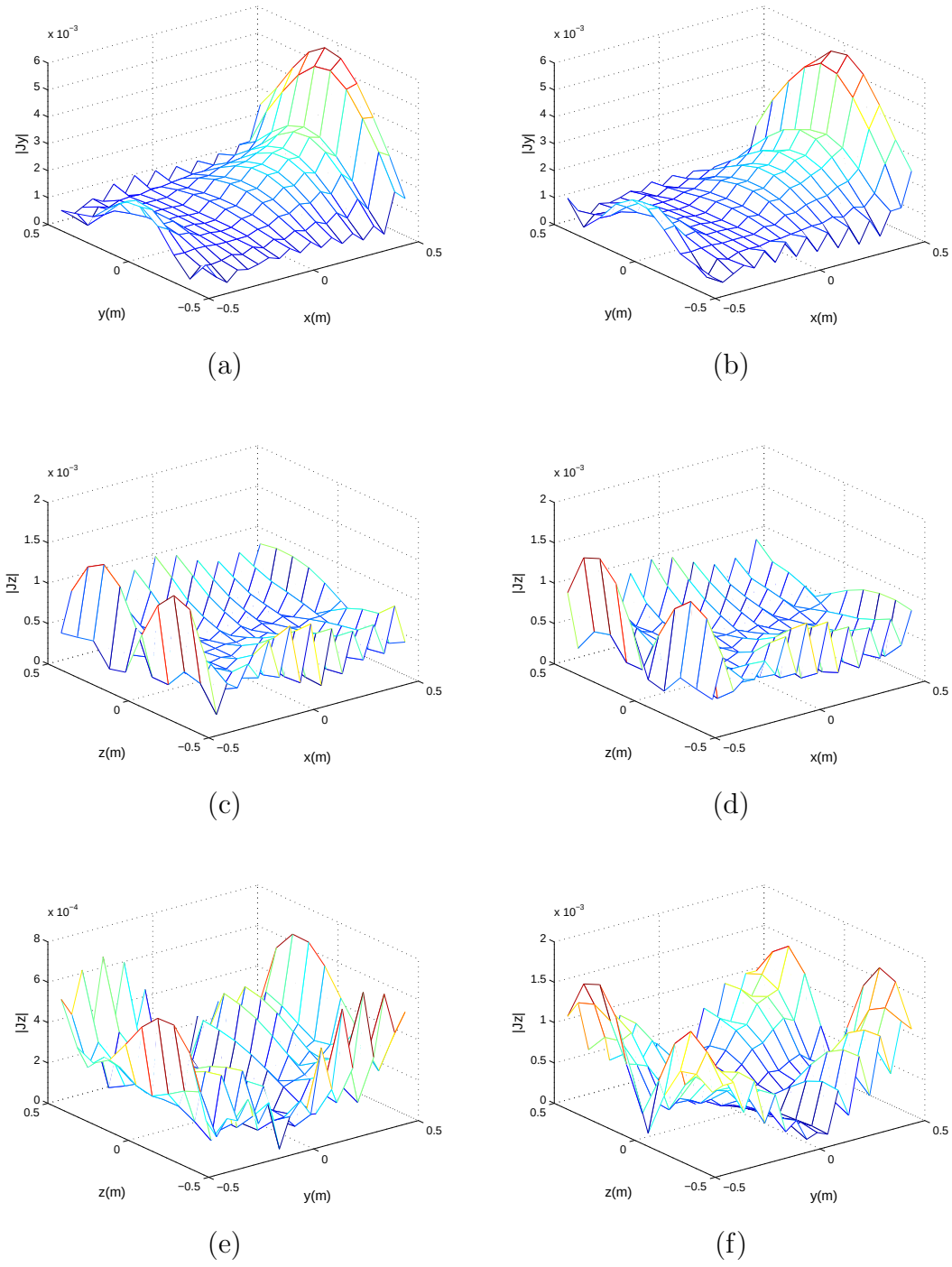

Figure 7.10: The current density results for a 1λ cube, obtained with the MoM-MFIE, y component on the: (a) top face, (b) bottom face, z component on the: (c) right face, (d) left face, (e) front face, and (f) back face.

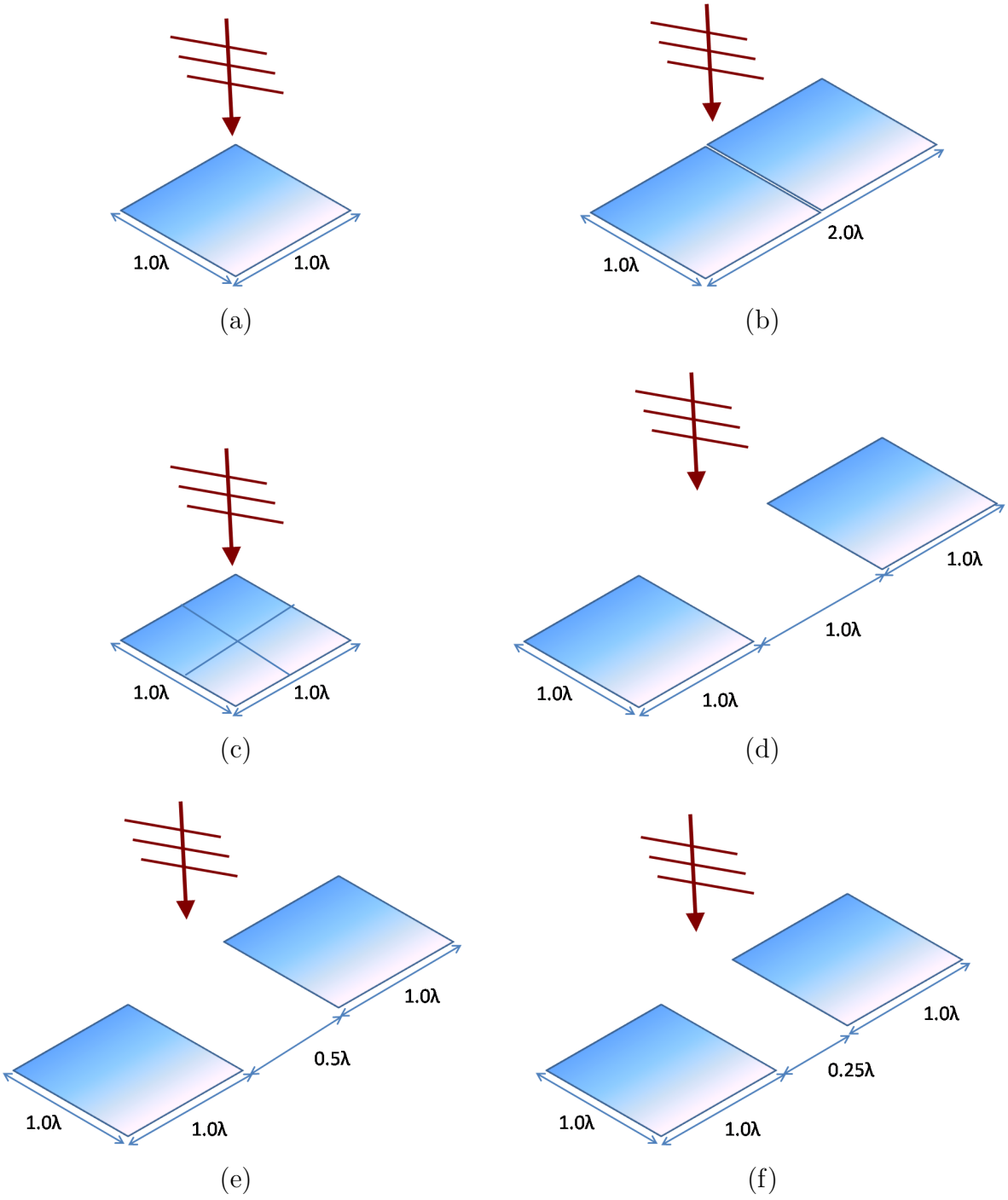

Figure 7.11: The geometries solved with the LCN-EFIE formulation.

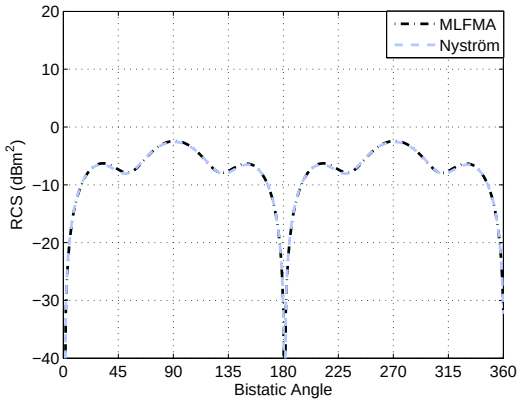

(a)

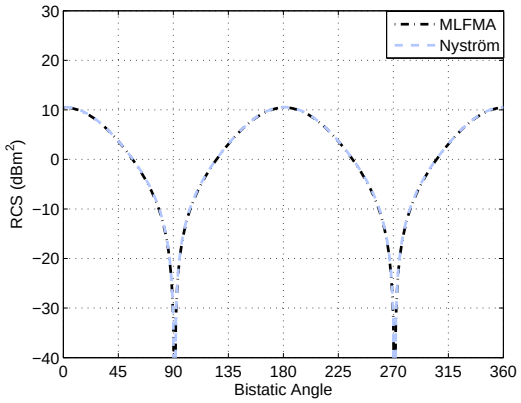

(b)

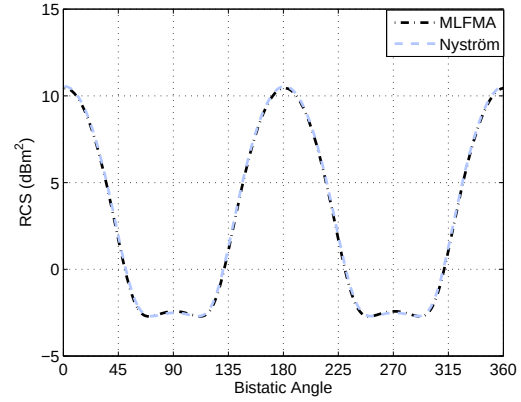

(c)

Figure 7.12: RCS values obtained by the LCN-EFIE formulation for the patch geometry in Figure 7.16-(a) on the (a) x-y cut, (b) x-z cut, and (c) y-z cut.

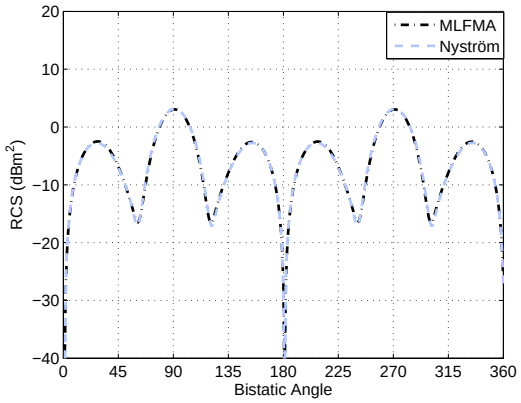

(a)

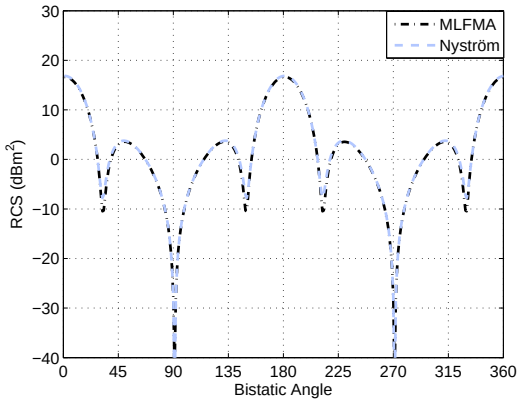

(b)

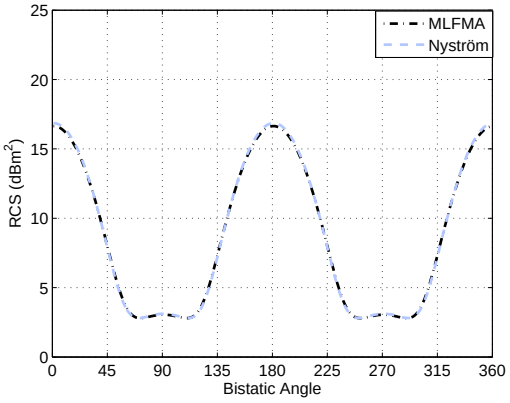

(c)

Figure 7.13: RCS values obtained by the LCN-EFIE formulation for the patch geometry in Figure 7.16-(b) on the (a) x-y cut, (b) x-z cut, and (c) y-z cut.

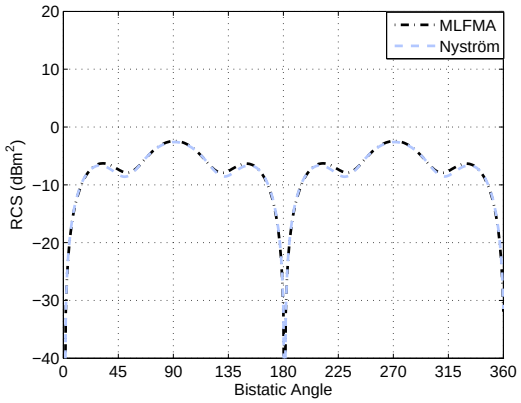

(a)

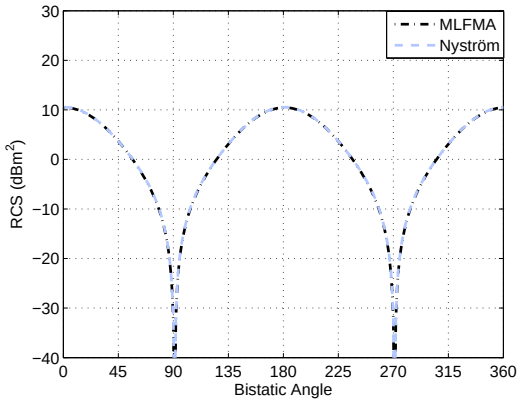

(b)

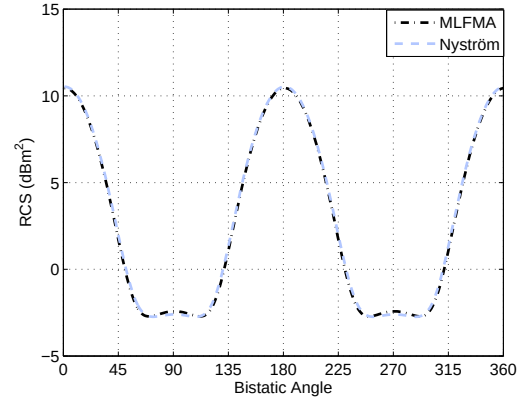

(c)

Figure 7.14: RCS values obtained by the LCN-EFIE formulation for the patch geometry in Figure 7.16-(c) on the (a) x-y cut, (b) x-z cut, and (c) y-z cut.

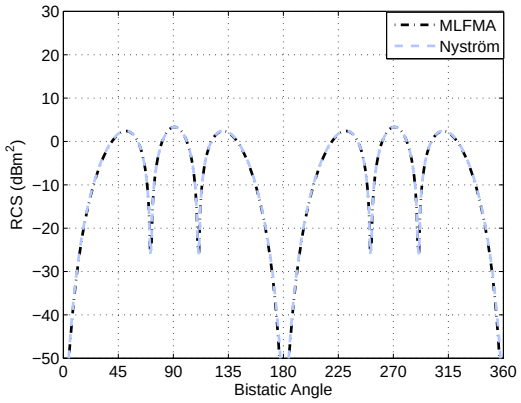

(a)

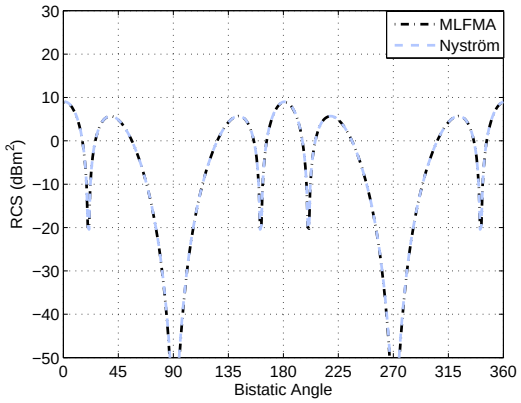

(b)

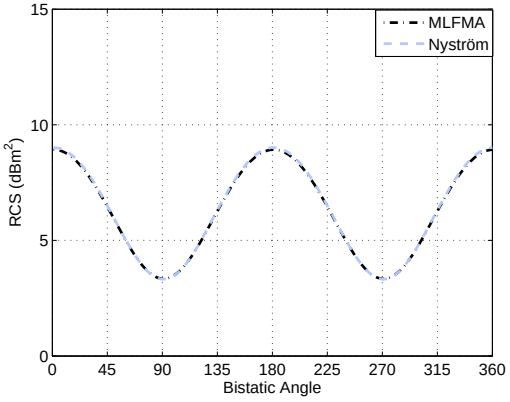

(c)

Figure 7.15: RCS values obtained by the LCN-EFIE formulation for the patch geometry in Figure 7.16-(d) on the (a) x-y cut, (b) x-z cut, and (c) y-z cut.

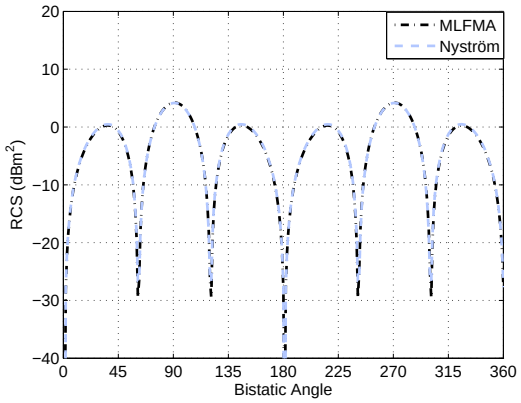

(a)

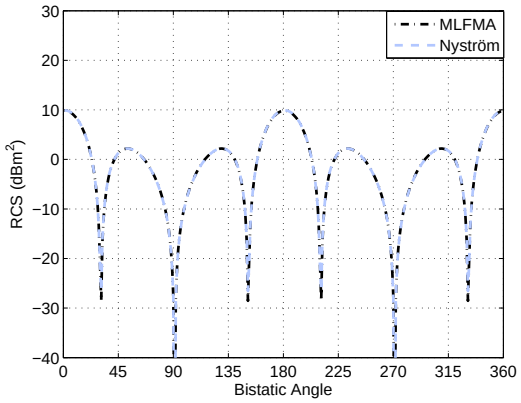

(b)

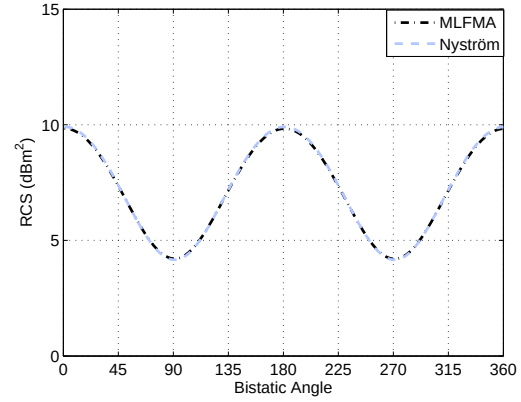

(c)

Figure 7.16: RCS values obtained by the LCN-EFIE formulation for the patch geometry in Figure 7.16-(e) on the (a) x-y cut, (b) x-z cut, and (c) y-z cut.

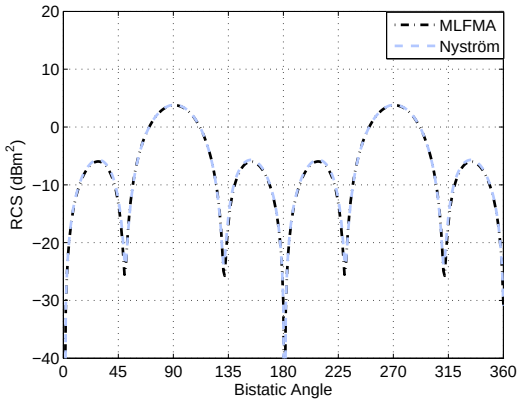

(a)

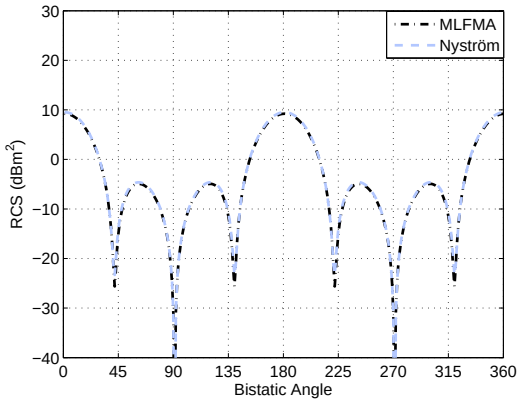

(b)

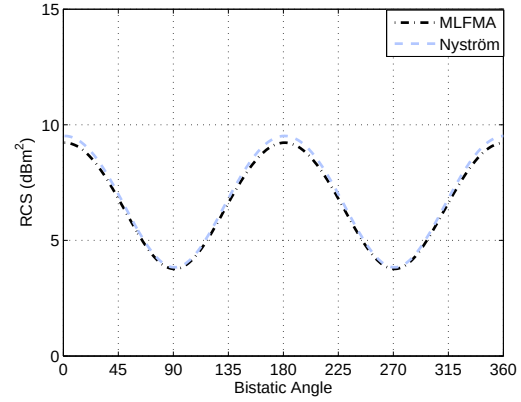

(c)

Figure 7.17: RCS values obtained by the LCN-EFIE formulation for the patch geometry in Figure 7.16-(f) on the (a) x-y cut, (b) x-z cut, and (c) y-z cut.

in three cuts. Note that, on the x-y cut, $\theta = \pi/2$ and ϕ changes from 0 to 2π as the bistatic angle. Similarly, on the x-z cut, $\phi = 0$ while θ changes, and on the y-z cut, $\phi = \pi/2$ while θ changes from 0 to π. The results are compared with MLFMA solutions.

Results shown in Figure 7.18 belong to a cube solved with the LCN-MFIE formulation at frequencies 300 MHz, 600 MHz, 900 MHz, and 1500 MHz with the number of unknowns 1200, 2700, 6912, and 12288, respectively. As we go to the higher frequencies, the curvilinear patches get larger with respect to the wavelength. Hence, to obtain solutions with high accuracy, we simply increase the order of the quadrature rule, or we can increase the number of curvilinear patches that are used to define the surface. At 300 MHz, we modeled the geometry with 150 curvilinear patches, and defined a quadrature rule with order two in both dimensions. Similarly, at 600 MHz, the surface of the geometry is divided into 150 patches. To solve the geometry at this frequency with high accuracy, the quadrature rule order is increased to four in two dimensions. Next, instead of increasing the order of quadrature rule, the surface is divided into 384 pieces for 900 MHz, and a 3×3 quadrature rule is employed on each of them. Finally, for the last frequency, we increase the quadrature rule order to four. So, as it can be predicted, the number of unknowns are calculated using the formula $2PN$, where P is the number of patches and N is the total number of integration points obtained by the underlying quadrature rule. We multiply by two, since we solve two coefficients to find the current density at a point.

Next, the scattering by a sphere is studied. The sphere problem is of interest because of its smooth geometry and the fact that the RCS can be calculated analytically using a Mie-series solution [21]. The sphere is discretized using curvilinear quadrilateral patches that exactly model the curvature. The radius of the sphere is 0.5 m, and we have presented the RCS results at several frequencies. Hence, the size of the sphere changes with respect to wavelength. The sphere is

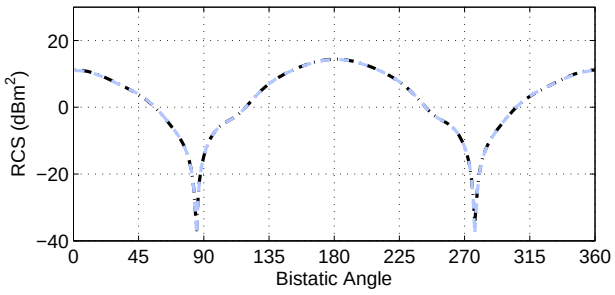

(a)

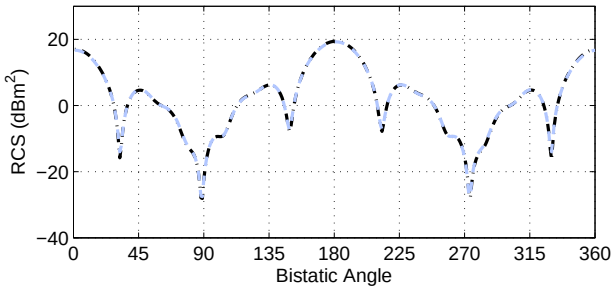

(b)

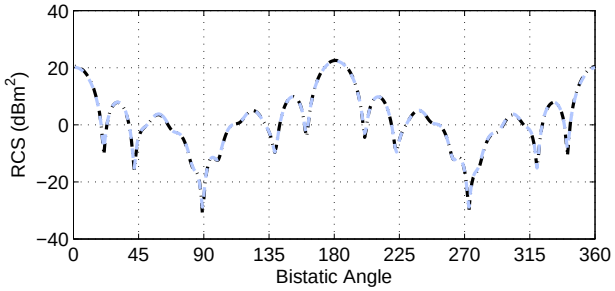

(c)

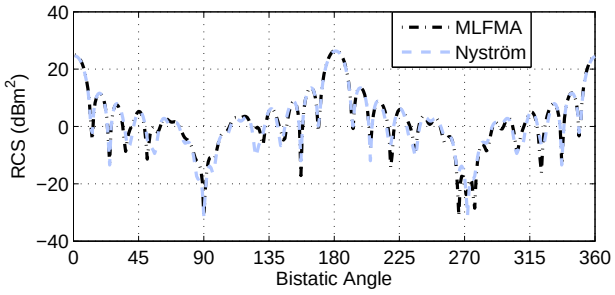

(d)

Figure 7.18: RCS values obtained by the LCN-MFIE formulation for a cube having a side length of (a) 1.0λ, (b) 2.0λ, (c) 3.0λ, and (d) 5.0λ.

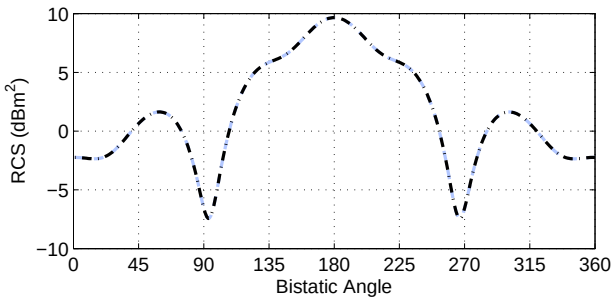

(a)

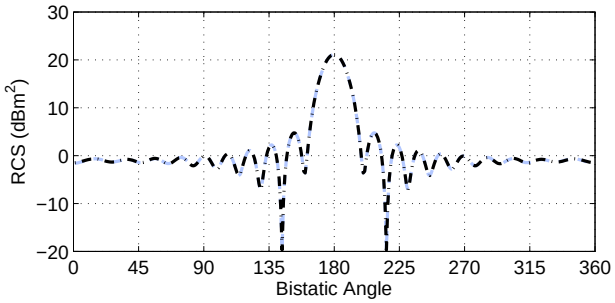

(b)

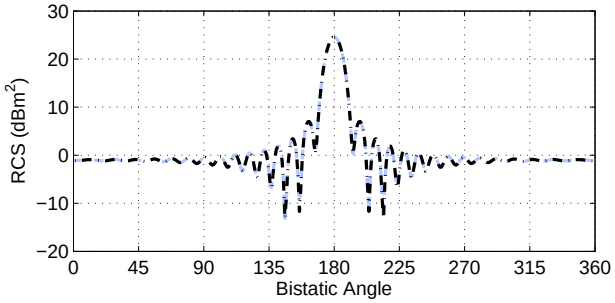

(c)

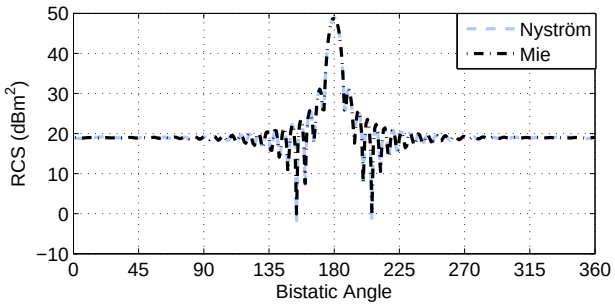

(d)

Figure 7.19: RCS values obtained by the LCN-MFIE formulation for a sphere having a radius of (a) 0.5λ, (b) 2.0λ, (c) 3.0λ, and (d) 5.0λ.

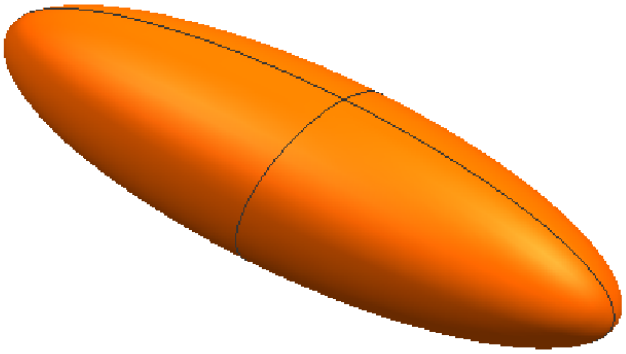

(a)

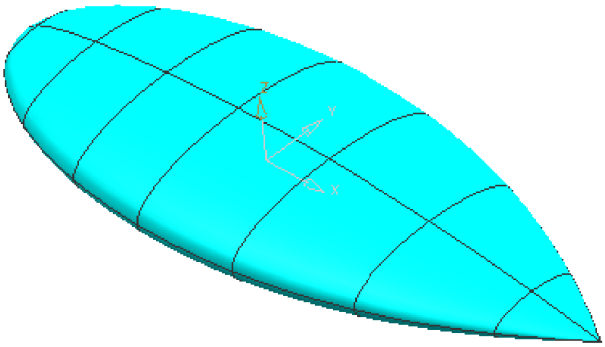

(b)

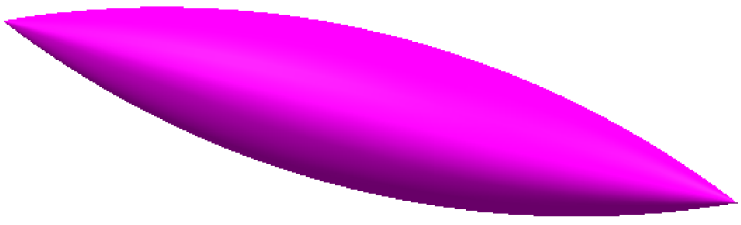

(c)

Figure 7.20: Geometries solved with the LCN method: (a) ellipsoid, (b) NASA almond, and (c) ogive.

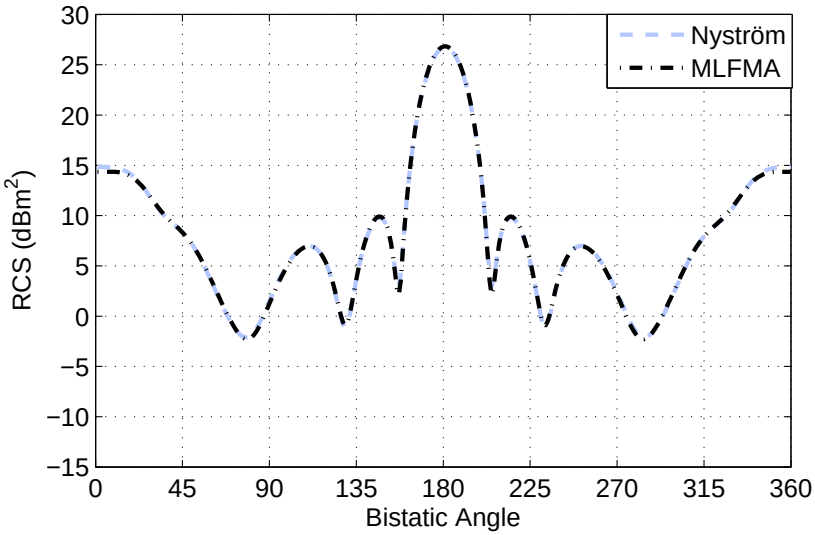

(a)

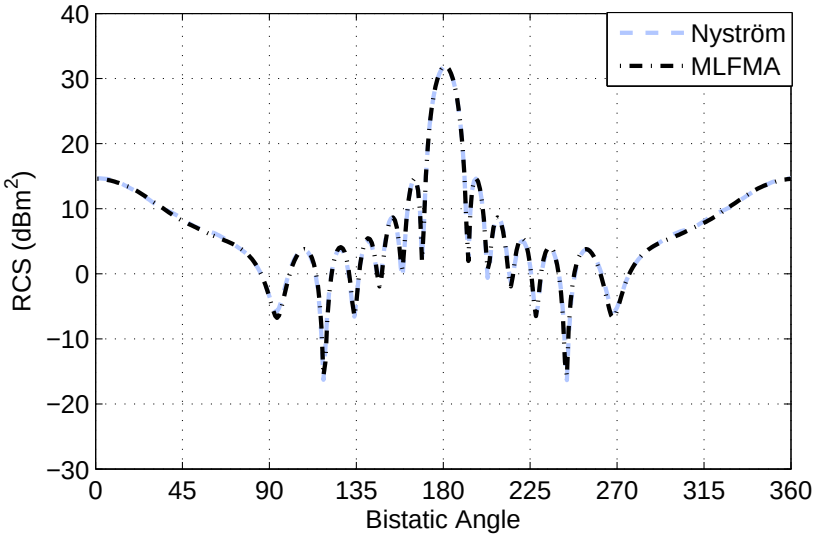

(b)

Figure 7.21: RCS values obtained by the LCN-MFIE implementation for an ellipsoid having principal axis diameters (a) $0.5\lambda \times 1.5\lambda$ and (b) $1.0\lambda \times 3.0\lambda$.

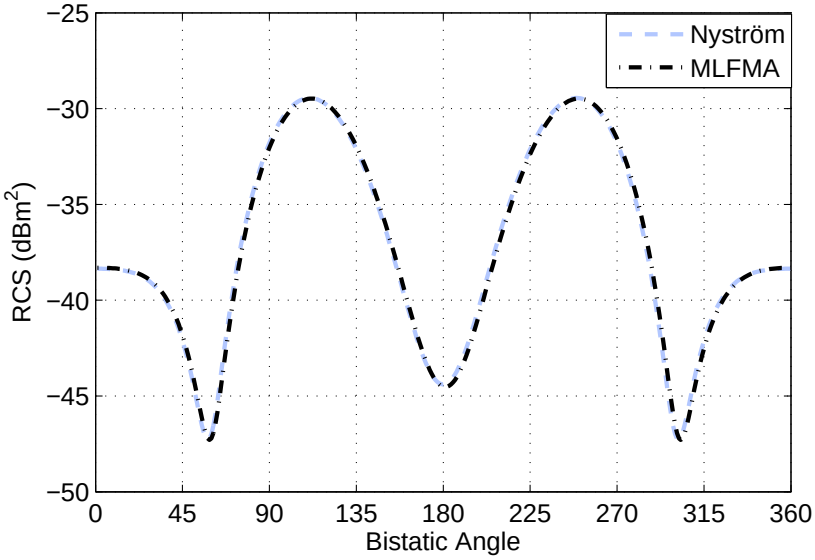

(a)

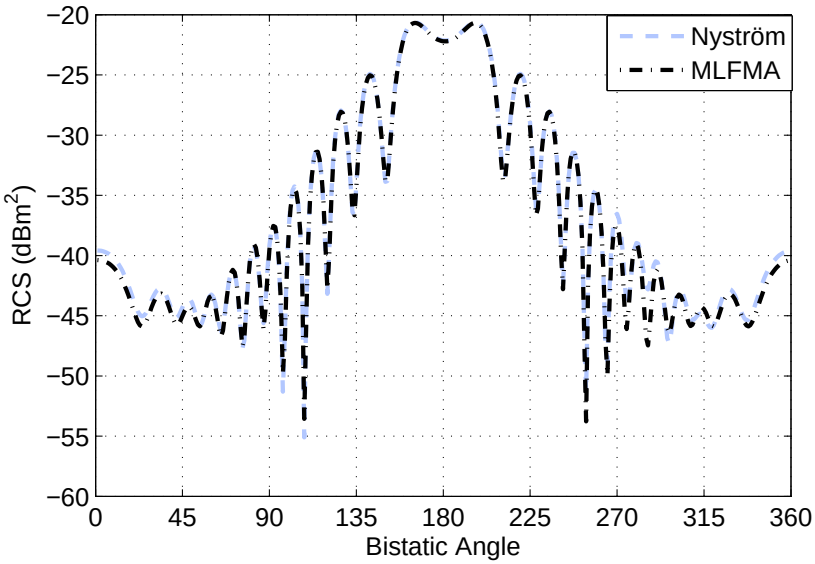

(b)

Figure 7.22: RCS values obtained by the LCN-MFIE implementation for the NASA almond at (a) 1.19 GHz and (b) 7 GHz.

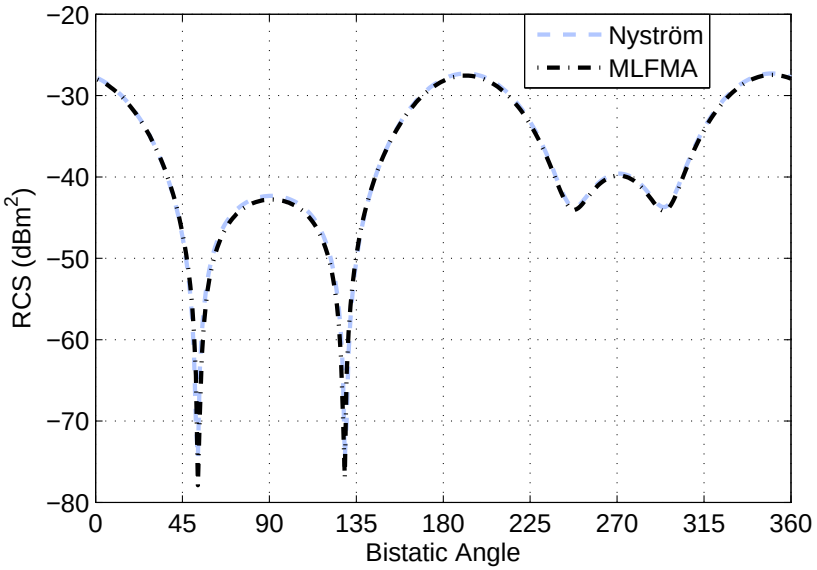

(a)

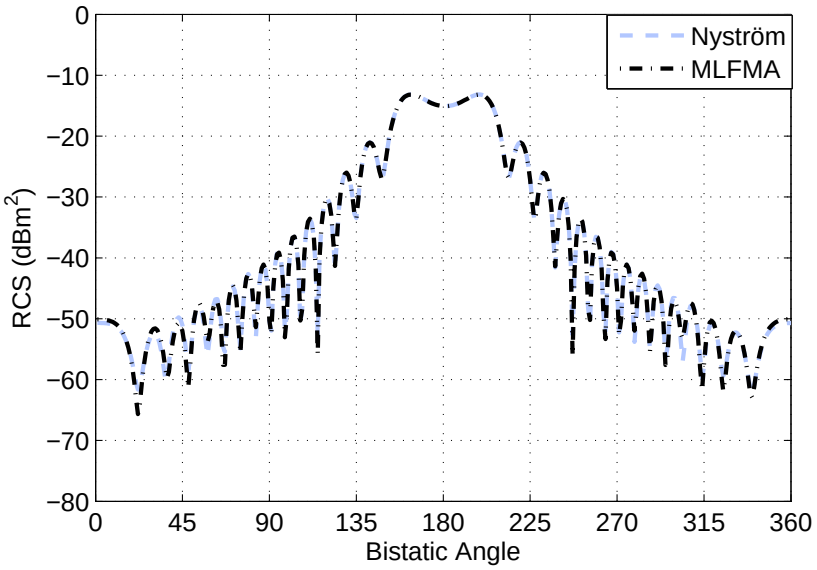

(b)

Figure 7.23: RCS values obtained by the LCN-MFIE implementation for the ogive at (a) 1.18 GHz and (b) 9 GHz.

illuminated by a plane wave propagating in the $-\hat{z}$ direction. We modeled the geometry with 150 curvilinear patches and used 2×2 quadrature rule on each patch at 300 MHz, hence the number of unknowns is 1200. The number of patches becomes 216 at 1200 MHz, 486 at 1800 MHz, and 726 at 3000 MHz, while the order of quadrature rule remains as three in both dimensions. In Figure 7.19, we presented that the LCN method results perfectly match Mie-series solutions. In the following section, the accuracy and efficiency of the LCN method will be shown in details.

Another example is the electromagnetic scattering by an ellipsoid, which is also a smooth but less symmetric geometry than the sphere. The RCS values are plotted in Figure 7.21 together with MLFMA results. The number of unknowns is 2156 for the first problem and 2816 for the second one. The plane-wave propagates in the $-\hat{z}$ direction in this problem.

Next, the scattering by the NASA almond, whose dimensions are published in [22], is studied. The NASA almond is a challenging structure in that the geometry is singular at the two tips and there is a high-rate of curvature in the geometry. While meshing this geometry with curvilinear patches, first the singular tips are modeled in the shape of a diamond, then the remaining parts are meshed with quadrilateral elements. The almond is excited from the singular tips, and the bistatic RCS is obtained. First, the RCS is computed at 1.19 GHz with 46 curvilinear cells and third-order Gauss-Legendre quadrature rule. Note that, at 1.19 GHz the almond is approximately one wavelength long. The RCS was also computed with the MLFMA solver, and these results are illustrated in Figure 7.22(a). It is found in the LCN method that with 828 unknowns the RCS is predicted accurately. The RCS results are also illustrated at 7 GHz as shown in Figure 7.22(b). For the LCN simulation, the geometry is modeled with 110 curvilinear patches and fifth-order quadrature rule is employed on each of these patches.

The last example is scattering by an ogive, whose dimensions are also published in [22]. The ogive is a rotationally symmetric geometry. By illuminating from the singular tips, the RCS values are obtained at 1.18 GHz and 9 GHz. And these results are presented in Figure 7.23. Results at 1.18 GHz are obtained with a discretization by 60 curvilinear cells and second-order quadrature rule is used on each of the cells, while at 9 GHz the number of cells is 226 and quadrature rule is again second-order.

7.3 Efficiency and Accuracy Comparisons with the MLFMA

In the preceding sections, we have presented the current density and RCS results for several geometries. We compared the results with the analytical solutions or the MLFMA solver results. Here, we will illustrate the accuracy of the LCN method by the relative error plots. Also, we will present the efficiency of the method with the CPU-time measurements. The mean error in the RCS is calculated as

$$\text{Mean Error} = \frac{1}{N_a} \sum_{i=1}^{N_a} \frac{|RCS_{LCN}(\theta_i, \phi_i) - RCS_{ref}(\theta_i, \phi_i)|}{|RCS_{ref}(\theta_i, \phi_i)|}, \tag{7.1}$$

where N_a is the number of bistatic angles. Using this formulation, we calculated the mean error of the RCS values of the sphere geometry obtained with the LCN-MFIE formulation. The reference values are obtained from the exact Mie series solutions. Comparisons with the MLFMA solver in Figures 7.24(a) and 7.25(a) show that the LCN method reaches to a better accuracy by using less number of unknowns for both the EFIE and the MFIE. With approximately same number of unknowns, the LCN method is more accurate then the MLFMA. Also, the convergence of the MLFMA results are quite slow when compared to the convergence of the LCN results. Next, we compared the CPU-times of both

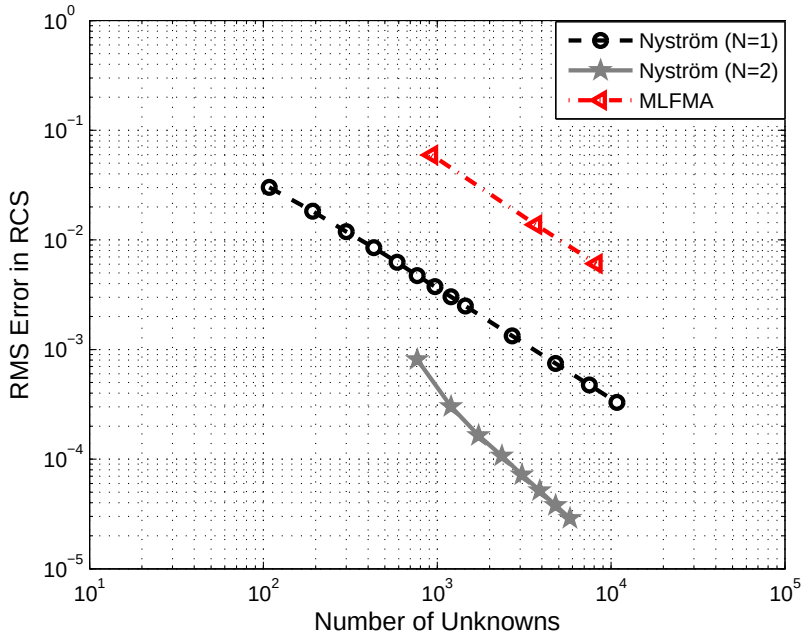

(a)

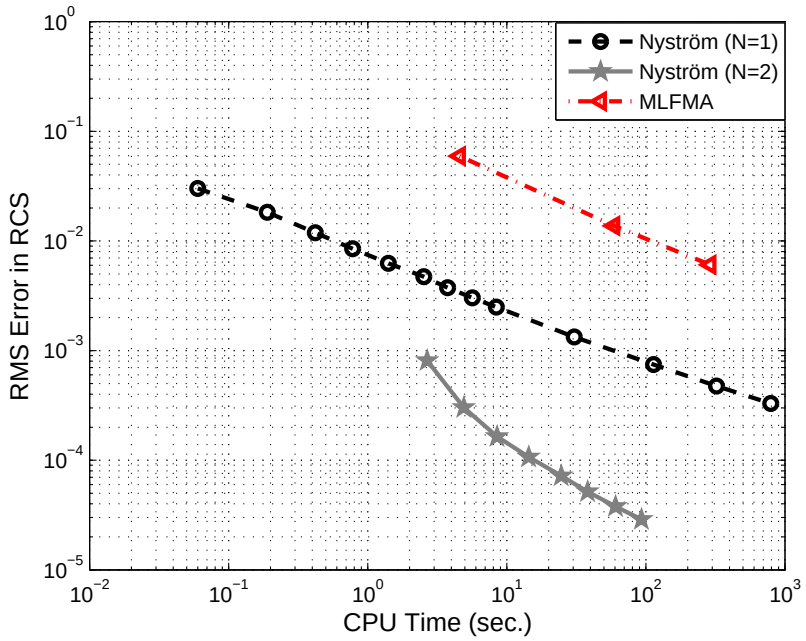

(b)

Figure 7.24: Comparison of the MLFMA and the LCN methods for the MFIE solution of sphere : (a) RMS error versus number of unknowns and (b) RMS error versus CPU-time.

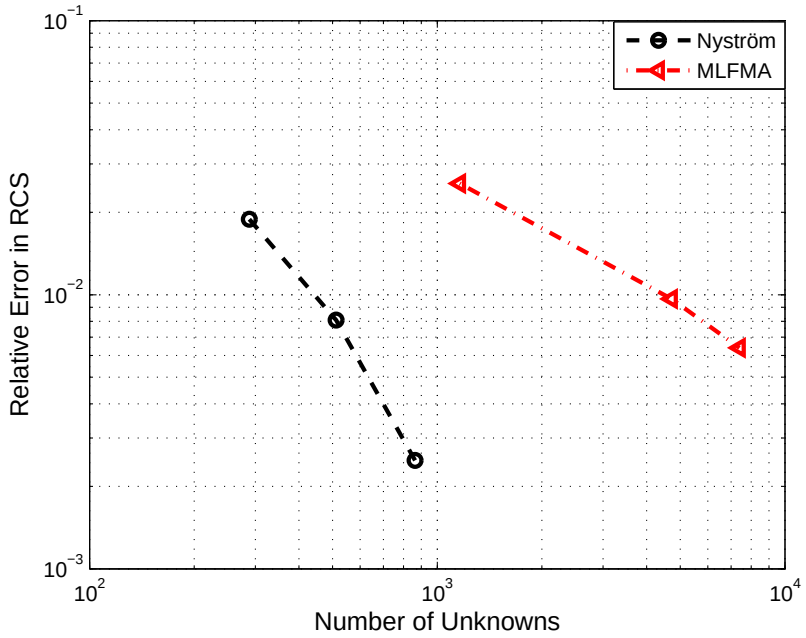

(a)

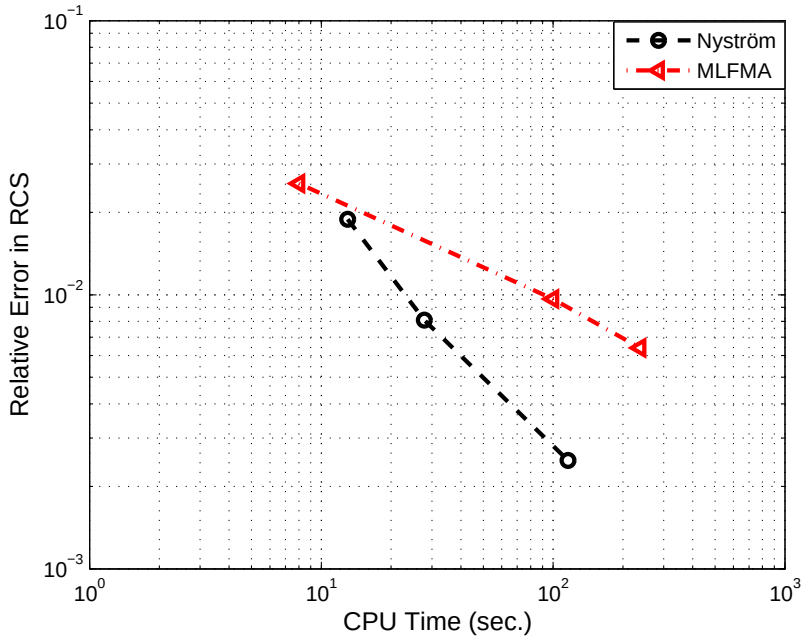

(b)

Figure 7.25: Comparison of the MLFMA and the LCN methods for EFIE solution of patch geometry: (a) Relative error versus number of unknowns and (b) Relative error versus CPU-time.

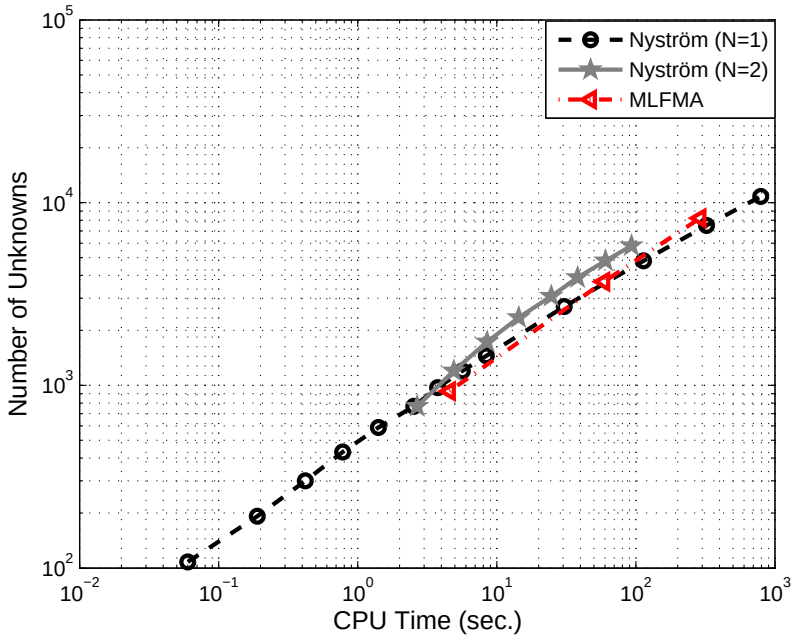

(a)

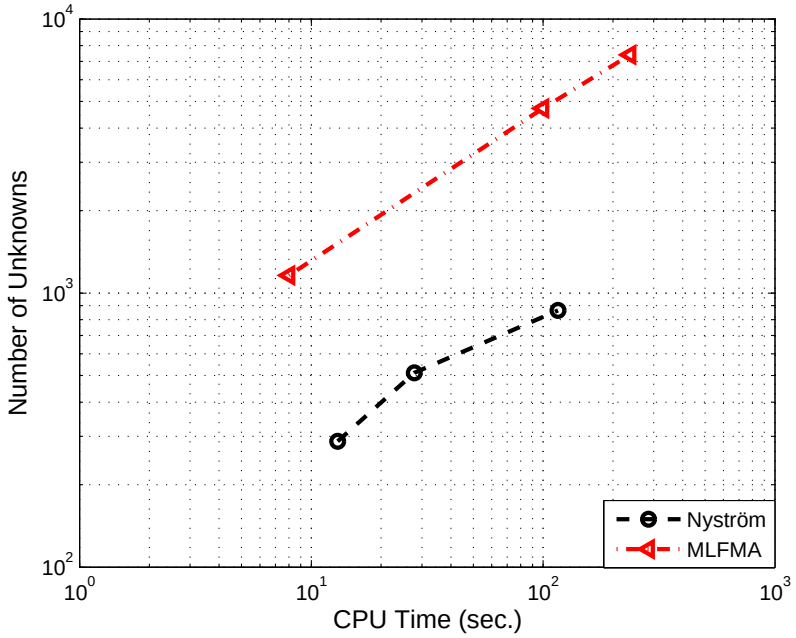

(b)

Figure 7.26: Number of unknowns versus CPU-time results for the MLFMA and the LCN methods for (a) the MFIE (b) the EFIE.

of the methods in Figures 7.24(b) and 7.25(b). The LCN impedance matrix is solved using the direct solver of the LAPACK library, while the MLFMA matrix is solved iteratively with biconjugate gradient stabilized method. Furthermore, the block diagonal preconditioner is applied to MLFMA, to accelerate the convergence of the iterative solver. Nevertheless, it is obvious from results that the LCN method is more efficient than the MLFMA for a desired accuracy, in terms of CPU-time. When we compare EFIE and MFIE solution of the LCN method, the time required for the EFIE solution is more than the MFIE solution. The reason for this is, for the EFIE formulation, number of integrations required for local corrections are more than the MFIE formulation. This is important because the majority of the CPU-time is spent for local corrections.

Next, we have showed results for the required time to solve a number of unknowns both with the LCN method and the MLFMA. As seen from Figure 7.26, for MFIE, both of the methods solve the problem with the same number of unknowns at approximately the same time. On the other hand, for EFIE, MLFMA is faster than the LCN method. This result is not surprising because of the computation time for the local corrections of the LCN method. Also, remember that the impedance matrix of the LCN method is solved directly, while MLFMA is solved iteratively and it is accelerated with preconditioners.

Chapter 8

Conclusion and Future Work

In this thesis, the LCN method is investigated in details for the solution of electromagnetic scattering problems involving arbitrary shaped, 3-D, conducting geometries. The LCN method is applied to EFIE and MFIE.

The classical Nyström method is a simple and efficient mechanism for discretizing the integral equations, but it can only be applied to the regular kernels. Hence, we introduced the local correction procedure for singular kernels. To obtain high-order solutions, we modeled the geometry with curvilinear patches, and we approximated numerical integrations with Gauss-Legendre quadrature rules. During the local corrections, we expanded the current in terms of known basis functions, which are chosen as Legendre polynomials.

Chapter 3 and Chapter 4 present an overview of the LCN method implementation using EFIE and MFIE formulations, respectively. Both EFIE and MFIE kernels have a $1/R$ singularity and these singularities are handled using the Duffy transform and adaptive integrations. The classical Duffy transform uses too many integration points to reach the desired accuracy when the observation point is close to an edge or a corner. So we modified the Duffy transform to handle this problem. We followed a procedure to improve the aspect ratio of Duffy triangles.

Instead of applying the Duffy transform to the triangles with bad-aspect ratios, we applied to ones with better aspect ratio and smaller size. As a result of this, the overall time required for the Duffy calculations are substantially decreased. At the same time, we showed that the accuracy remains approximately the same for both of the methods.

In Chapter 6, we have shown that, for EFIE, the charge density cannot be represented to complete order if the polynomial-complete basis functions are employed in local corrections. This causes inaccurate results for the current density solution. Hence, we presented the enhancement of the results with the mixed-order basis functions on some patch examples.

Finally, we have presented current density and RCS results for several geometries. We have compared our results with the analytical solutions or MLFMA results. We have shown that the LCN method is more accurate and more efficient than the MLFMA. The LCN method can reach to a better accuracy with less number of unknowns and in a shorter time. The convergence of the MLFMA results are quite slow when compared to the convergence of the LCN results.

The future work includes the parallelization of the LCN method to solve larger electromagnetic scattering problems. Also, the computational requirements to solve the impedance matrix can be minimized by using iterative methods and preconditioning techniques.

Bibliography

[1] R. F. Harrington, *Field Computation by Moment Methods*. New York: Macmillan, 1968.

[2] N. Engheta, W. D. Murphy, V. Rokhlin, and M. S. Vassiliou, "The fast multipole method (FMM) for electromagnetic scattering problems," *IEEE Trans. Antennas Propagat.*, vol. 40, no. 6, pp. 634-641, June 1992.

[3] R. Coifman, V. Rokhlin, and S. Wandzura, "The fast multipole method for the wave equation: a pedestrian prescription," *IEEE Ant. Propag. Mag.*, vol. 35, no. 3, pp. 7-12, June 1993.

[4] C.-C. Lu and W. C. Chew, "Multilevel fast multipole algorithm for electromagnetic scattering by large complex objects," *IEEE Trans. Antennas Propagat.*, vol. 45, no. 10, pp. 1488-1493, Oct. 1997.

[5] W. C. Chew, J.-M. Jin, E. Michielssen, and J. M. Song, eds., *Fast and Efficient Algorithms in Computational Electromagnetics*. Boston-London: Artech House Publishers, 2001.

[6] S. M. Rao, D. R. Wilton, and A. W. Glisson, "Electromagnetic scattering by surfaces of arbitrary shape," *IEEE Trans. Antennas Propag.*, vol. 30, no. 3, pp. 409–418, May 1982.

[7] L. F. Canino, J. J. Ottusch, M. A. Stalzer, J. L. Visher, and S. M. Wandzura, "Numerical solution of the Helmholtz equation in 2D

and 3D using a high-order Nyström discretization," *J. Comput. Phys.*, vol. 146, pp. 627–663, Aug. 1998.

[8] S. D. Gedney, "On deriving a locally corrected Nyström scheme from a quadrature sampled moment method," *IEEE Trans. Antennas Propagat.*, vol. 51, no. 9, pp. 2402–2412, Sep. 2003.

[9] S. D. Gedney, "Application of the high-order Nyström scheme to the integral equation solution of electromagnetic interaction problems," in *IEEE International Symposium on Electromagnetic Compatibility*, pp. 289–294, Aug. 2000.

[10] Ö. S. Ergül, *Accurate and efficient solutions of electromagnetic problems with the multilevel fast multipole algorithm*, PhD Thesis, Bilkent University, Ankara, Turkey, Aug. 2009.

[11] Ö. Ergül and L. Gürel, "Comparison of integral-equation formulations for the fast and accurate solution of scattering problems involving dielectric objects with the multilevel fast multipole algorithm," *IEEE Trans. Antennas Propagat.*, vol. 57, no. 1, pp. 176–187, Jan. 2009.

[12] Ö. Ergül and L. Gürel, "Fast and accurate solutions of large-scale scattering problems with parallel multilevel fast multipole algorithm," in *Proc. IEEE Antennas and Propagation Soc. Int. Symp.*, pp. 3436–3439, 2007.

[13] J. Strain, "Locally-corrected multidimensional quadrature rules for singular functions," *SIAM J. Sci. Comput.*, vol. 16, pp. 992, 1995.

[14] S. D. Gedney, "High-order sparse matrix Nyström algorithm for the analysis of planar microwave circuits," Technical Report, *The University of Kentucky*, Nov. 2000, Accession Number: 100.2/ADA385792.

[15] Ö. S. Ergül, *Fast multipole method for the solution of electromagnetic scattering problems*, M.S. Thesis, Bilkent University, Ankara, Turkey, June 2003.

[16] M. G. Duffy, "Quadrature over a pyramid or cube of integrands with a singularity at the vertex," *SIAM Journal of Numerical Analysis*, vol. 19, pp. 1260–1262, Dec. 1982.

[17] F. Çalışkan and A. F. Peterson, "The need for mixed-order representations with the locally corrected Nyström method," *IEEE Antennas Wireless Propag. Lett.*, vol. 2, pp. 72–73, 2003.

[18] L. Gürel, K. Sertel, and İ. K. Şendur, "On the choice of basis functions to model surface electric current densities in computational electromagnetics," *Radio Sci.*, vol. 34, no. 6, pp. 1373–1387, Nov.-Dec. 1999.

[19] S. D. Gedney, A. Zhu, and C.-C. Lu, "Mixed-order basis functions for the locally corrected Nyström method," *IEEE Antennas and Propagation Society International Symposium*, vol. 4, pp. 4044–4047, June 2004.

[20] S. D. Gedney, A. Zhu, and C.-C. Lu, "Study of mixed-order basis functions for the locally corrected Nyström method," *IEEE Trans. Antennas Propagat.*, vol. 52, no. 11, pp. 2996–3004, Nov. 2004.

[21] G. Mie, "Contributions to the optics of turbid media, particularly of colloidal metal solutions," in German, *Ann. Phys.*, vol. 25, no. 3, pp. 377-445, 1908.

[22] A. C. Woo, H. T. G. Wang, M. J. Schuh, and M. L. Sanders, "Benchmark radar targets for the validation of computational electromagnetics programs," *IEEE Antennas Propagat. Mag.*, vol. 35, pp. 84–89, 1993.

[23] S. D. Gedney, "Implementing the locally corrected Nyström method," *Applied Computational Electromagnetics Society Newsletter*, vol. 18, no. 3, pp. 15–27, Nov. 2003.

[24] S. D. Gedney, J. Ottusch, P. Petre, J. Visher, S. Wandzura, "Efficient high-order discretization schemes for integral equation methods ,"

IEEE Antennas and Propagation Society International Symposium, vol. 3, pp. 1814–1817, 1997.

Chapter 9

Appendix A: Legendre Polynomials

Legendre polynomials are used as high-order basis functions to calculate the local correction coefficients of the locally corrected Nyström method. The Legendre polynomials are solutions to the following differential equation

$$\frac{d}{dx}\Big[(1-x^2)\frac{d}{dx}P_n(x)\Big] + n(n+1)P_n(x) = 0. \tag{9.1}$$

Then, $n-th$ order Legendre polynomial can be expressed using Rodrigues' formula

$$P_n(x) = \frac{1}{2^n n!}\frac{\partial^n}{\partial x^n}(x^2-1)^n. \tag{9.2}$$

The Legendre polynomials are also recursively written using Bonnet's recursion formula

$$(n+1)P_{n+1}(x) = (2n+1)xP_n(x) - nP_{n-1}(x). \tag{9.3}$$

First few Legendre polynomials can be expressed as

$$
\begin{aligned}
P_0(x) &= 1 \\
P_1(x) &= x \\
P_2(x) &= \frac{1}{2}(3x^2 - 1) \\
P_3(x) &= \frac{1}{2}(5x^3 - 3x) \\
P_4(x) &= \frac{1}{8}(35x^4 - 30x^2 + 3) \\
P_5(x) &= \frac{1}{8}(63x^5 - 70x^3 + 15x) \\
P_6(x) &= \frac{1}{16}(231x^6 - 315x^4 + 105x^2 - 5)
\end{aligned} \tag{9.4}
$$

Derivatives of the Legendre polynomials are calculated as

$$P'_{n+1}(x) = (n+1)P_n(x) + xP'_n(x). \tag{9.5}$$

9.1 Shifted Legendre Polynomials

The shifted Legendre polynomials are defined as $\hat{P}_n(x) = P_n(2x-1)$. With this transformation the interval [0,1] is mapped to the interval [-1,1]. First few shifted Legendre polynomials can be written as

$$
\begin{aligned}
P_0(x) &= 1 \\
P_1(x) &= 2x - 1 \\
P_2(x) &= (6x^2 - 6x + 1) \\
P_6(x) &= (20x^3 - 30x^2 + 12x - 1)
\end{aligned} \tag{9.6}
$$

Chapter 10

Appendix B: Biquadratic Surfaces

A given surface is parameterized by dividing it into generalized quadrilaterals and introducing a curvilinear (u, v) coordinate system on each quadrilateral. It is assumed that a parametric representation of a surface is given by

$$\boldsymbol{r}(u,v) = \hat{\boldsymbol{x}} f_x(u,v) + \hat{\boldsymbol{y}} f_y(u,v) + \hat{\boldsymbol{z}} f_z(u,v), \qquad (u,v) \in [-1,1], \tag{10.1}$$

where f_x,f_y, and f_v are continuous functions with continuous derivatives. The so-called covariant unitary vectors are defined as

$$\boldsymbol{a}_u = \frac{\partial \boldsymbol{r}}{\partial u}, \qquad \boldsymbol{a}_v = \frac{\partial \boldsymbol{r}}{\partial v} \tag{10.2}$$

are tangential to the u and v coordinate curves.

When the continuous functions are of first order, the representation becomes bilinear, biquadratic when it is 2, and bicubic when the order is 3. Also, high order representations are possible, i.e., splines or NURBS. A biquadratic surface representation is formulated as

$$\boldsymbol{r}(u,v) = \sum_{i=0}^{2} \sum_{j=0}^{2} \boldsymbol{a}_{ij} u^i v^j, \tag{10.3}$$

where $\boldsymbol{a}_{ij}$'s are vector coefficients. Then, the sampling points can be obtained on each patch by uniformly sampling $n \times n$ points in the $u - v$ domain. The unitary vectors can be written by calculating the derivatives of (10.3) as

$$\frac{\partial \boldsymbol{r}}{\partial u} = \sum_{i=0}^{2} \sum_{j=0}^{2} \boldsymbol{a}_{ij} i u^{i-1} v^{j} \tag{10.4}$$

$$\frac{\partial \boldsymbol{r}}{\partial v} = \sum_{i=0}^{2} \sum_{j=0}^{2} \boldsymbol{a}_{ij} u^{i} j v^{j-1}. \tag{10.5}$$